2015

NONCONTACT DIFFUSE CORRELATION TOMOGRAPHY OF BREAST TUMOR

Lian He
University of Kentucky, lian.he@uky.edu

STUDENT AGREEMENT:

I represent that my thesis or dissertation and abstract are my original work. Proper attribution has been given to all outside sources. I understand that I am solely responsible for obtaining any needed copyright permissions. I have obtained needed written permission statement(s) from the owner(s) of each third-party copyrighted matter to be included in my work, allowing electronic distribution (if such use is not permitted by the fair use doctrine) which will be submitted to UKnowledge as Additional File.

I hereby grant to The University of Kentucky and its agents the irrevocable, non-exclusive, and royalty-free license to archive and make accessible my work in whole or in part in all forms of media, now or hereafter known. I agree that the document mentioned above may be made available immediately for worldwide access unless an embargo applies.

I retain all other ownership rights to the copyright of my work. I also retain the right to use in future works (such as articles or books) all or part of my work. I understand that I am free to register the copyright to my work.

REVIEW, APPROVAL AND ACCEPTANCE

The document mentioned above has been reviewed and accepted by the student's advisor, on behalf of the advisory committee, and by the Director of Graduate Studies (DGS), on behalf of the program; we verify that this is the final, approved version of the student's thesis including all changes required by the advisory committee. The undersigned agree to abide by the statements above.

Lian He, Student

Dr. Guoqiang Yu, Major Professor

Dr. Abhijit R. Patwardhan, Director of Graduate Studies

NONCONTACT DIFFUSE CORRELATION TOMOGRAPHY OF BREAST TUMOR

DISSERTATION

A dissertation submitted in partial fulfillment of the requirements for the degree of Doctor of Philosophy in the College of Engineering at the University of Kentucky

By

Lian He

Lexington, Kentucky

Director: Dr. Guoqiang Yu, Associate Professor of Biomedical Engineering

Co-Director: Dr. Abhijit R. Patwardhan, Professor of Biomedical Engineering

Lexington, Kentucky

2015

ABSTRACT OF DISSERTATION

NONCONTACT DIFFUSE CORRELATION TOMOGRAPHY
OF BREAST TUMOR

Since aggressive cancers are frequently hypermetabolic with angiogenic vessels, quantification of blood flow (BF) can be vital for cancer diagnosis. Our laboratory has developed a noncontact diffuse correlation tomography (ncDCT) system for 3-D imaging of BF distribution in deep tissues (up to centimeters). The ncDCT system employs two sets of optical lenses to project source and detector fibers respectively onto the tissue surface, and applies finite element framework to model light transportation in complex tissue geometries. This thesis reports our first step to adapt the ncDCT system for 3-D imaging of BF contrasts in human breast tumors. A commercial 3-D camera was used to obtain breast surface geometry which was then converted to a solid volume mesh. An ncDCT probe scanned over a region of interest on the breast mesh surface and the measured boundary data were used for 3-D image reconstruction of BF distribution. This technique was tested with computer simulations and in 28 patients with breast tumors. Results from computer simulations suggest that relatively high accuracy can be achieved when the entire tumor was within the sensitive region of diffuse light. Image reconstruction with a priori knowledge of the tumor volume and location can significantly improve the accuracy in recovery of tumor BF contrasts. In vivo ncDCT imaging results from the majority of breast tumors showed higher BF contrasts in the tumor regions compared to the surrounding tissues. Reconstructed tumor depths and dimensions matched ultrasound imaging results when the tumors were within the sensitive region of light propagation. The results demonstrate that ncDCT system has the potential to image BF distributions in soft and vulnerable tissues without distorting tissue hemodynamics. In addition to this primary study, detector fibers with different modes (i.e., single-mode, few-mode, multimode) for photon collection were experimentally explored to improve the signal-to-noise ratio of diffuse correlation spectroscopy flow-oximeter measurements.

KEYWORDS

Diffuse Correlation Spectroscopy/Tomography (DCS/DCT); Breast tumor; Blood flow contrast; Noncontact; Optical fiber mode

Lian He
Student's Signature

August 5th, 2015
Date

NONCONTACT DIFFUSE CORRELATION TOMOGRAPHY OF BREAST TUMOR

By

Lian He

Dr. Guoqiang Yu
Director of Dissertation

Dr. Abhijit R. Patwardhan
Co-Director of Dissertation

Dr. Abhijit R. Patwardhan
Director of Graduate Studies

August 5th, 2015

DEDICATION

This work is dedicated to

Dad, Mom and Li

ACKNOWLEDGEMENTS

I would like to first thank my adviser, Dr. Guoqiang Yu, without whom this work would never have been possible. Most of my successful research ideas originated from discussions with Dr. Yu. Dr. Yu also spent a lot of time carefully editing my manuscripts and reviewing my oral presentations. My critical thinking and professional writing have been improved a lot during my graduate school years, in large part due to Dr. Yu's efforts.

I would also like to sincerely thank Dr. Yu Lin, who worked closely with me on this project, providing research guidance and assisting me in a lot of experiments. I would like to thank Dr. Chong Huang, for his assistance in all things technological and instrument-related, as well as his positive attitude. I cannot thank Dr. Yu Shang enough for his incredible patience while explaining concepts to me when I started graduate school. I acknowledge all my lab-mates, Daniel Irwin, Mingjun Zhao, Lixin Dong, Ahmed Abahrani, Katelyn Gurley, Weikai Kong and Drs. Ting Li and Ran Cheng. They have been invaluable to my thesis and improved the quality of my research life.

My appreciation further extends to my committee members, Drs. Abhijit Patwardhan, David Puleo, Ellis Johnson and Margaret Szabunio, who were all very responsive to my questions and requests and gave me great advising that illuminated my research field. I want to particularly thank Dr. Szabunio and her clinical team, including Vera Kadamyan, Toni Mucci, Vivian John and all other people from Comprehensive Breast Care Center and Markey Cancer Center who have helped me recruit patients and perform measurements. Without their help this clinical study would not be possible.

I also acknowledge the funding support from the National Institutes of Health (NIH) R01-CA149274 (G.Y.), R21-AR062356 (G.Y.), UL-1RR033173 Pilot Grant (G.Y.),

R25-CA153954 Predoctoral Traineeship (D.I.) and the dissertation year fellowship from University of Kentucky.

Finally I would like to thank my parents and husband. Without their constant support and encouragement, I could not have accomplished this dissertation.

TABLE OF CONTENTS

LIST OF TABLES

LIST OF FIGURES

LIST OF CHARTS

CHAPTER 1 INTRODUCTION

1.1 Classification of Breast Disease

The main function of the breasts is to make milk for breastfeeding. Glandular tissues and supporting (stromal) tissues are two main types of tissues in breasts (1). The glandular part of the breast includes the lobules and ducts (**Figure 1.1**). In women who are breastfeeding, the cells of the lobules make milk. The milk then moves through the ducts, which are tiny tubes that carry milk, to the nipple. Each breast has several ducts that lead out to the nipple. The support tissue of the breast includes fatty tissue and fibrous connective tissue that give the breast its size and shape.

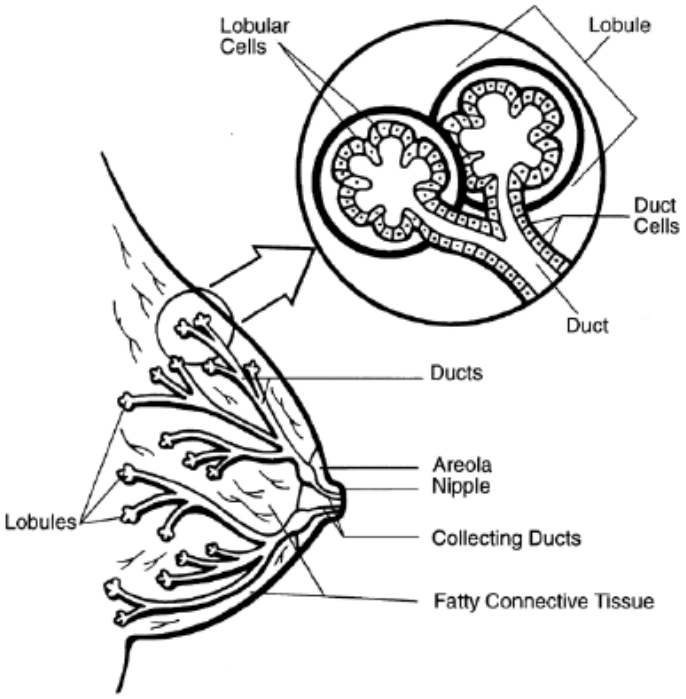

Figure 1.1: A schematic representation of the breast (1).

Changes in the breasts may be caused either by benign conditions or cancer. Most breast lesions detected are benign, which don't grow uncontrollably or spread, but they may be linked to breast cancer risk (2, 3). Benign breast diseases constitute heterogeneous groups of lesions including developmental abnormalities, inflammatory lesions, fibrocystic changes, proliferative stromal lesions, and neoplasms (3). Ectopic breast, which has been described as both supernumerary and aberrant breast tissue, is the most common congenital abnormality of the breast. Supernumerary breast tissue is seen mostly along the milk line; the most frequent sites are the chest wall, vulva, and axilla. However, malignancies in ectopic breasts are very rare (4, 5). Inflammatory and related lesions include mastitis, mammary duct ectasia and fat necrosis. Among those, mastitis is often caused by a breast infection and is most often seen in lactating women. Although mastitis does not raise a women's risk of developing breast cancer, an uncommon type of inflammatory breast cancer has symptoms that are a lot like mastitis. Mammary duct ectasia also called periductal mastitis. The most important histological feature of this disorder is the dilatation of major ducts in the subareolar region. There is no evidence indicating it is associated with an increased risk for breast cancer. Fat necrosis of the breast is a benign nonsuppurative inflammatory process of adipose tissue. Fibrocystic changes constitute the most frequent benign disorder of the breast. They comprise both cysts and solid lesions, including adenosis, epithelial hyperplasia with or without atypia, apocrine metaplasia, radial scar, and papilloma. In order to determine the risk factors for fibrocystic changes, they are subdivided into nonproliferative lesions, proliferative lesions without atypia, and proliferative lesions with atypical (atypical hyperplasia) (6-8). Proliferative stromal lesions include diabetic fibrous mastopathy and pseudoangiomatous

stromal hyperplasia of the breast. Neoplasms include fibroadenoma, lipoma, adenoma, hamartoma and granular cell tumor. Specifically, fibroadenoma is the most common lesion of the breast and it occurs in 25% of asymptomatic women. The peak incidence of fibroadenoma is between the ages of 15 and 35 years.

Breast cancer begins in the lobules and ducts (**Figure 1.1**). According to the extent of spread, breast cancer can be determined as in situ (noninvasive) or invasive. For in situ breast cancers, there are abnormal breast changes in the cells lining the breast ducts or lobules. The noninvasive breast tumors include ductal carcinoma in situ (DCIS), lobular carcinoma in situ (LCIS), and other in situ breast cancers have characteristics of both DCIS and LCIS. For invasive breast cancers, the abnormal cells have broken through the ductal or glandular walls and grown into surrounding breast tissue. Invasive breast cancers include ductal carcinoma, which is the most common type, invasive lobular carcinoma, medullary carcinoma, mucinous carcinoma, tubular carcinoma and invasive papillary carcinoma (9).

1.2 Medical Imaging for Breast Tumor

About 1 in 8 women in the United States will develop invasive breast cancer over her lifetime. Its high incidence and associated mortality makes it an important public health problem (2, 10). Finding breast cancers when they remain localized results in 5-year relative survival rates of 99% (2). The current clinical standard for breast screening is x-ray mammography which can often identify cancer several years before physical symptoms develop (2). The significant decrease in breast cancer mortality, which amounts to nearly 30% since 1990, is due in large part to the earlier detection of breast

cancer through mammographic screen (11). However, mammography is hampered by a significant false-positive rate, which is especially high for women with dense breast tissue. The dense breast population is a particularly important subset of women because they experience higher incidence and mortality rates from the disease (12, 13).

Other imaging modalities used as adjunctive screening tools for breast cancers include x-ray computed tomography (CT), magnetic resonance imaging (MRI), positron emission tomography (PET) and ultrasonography (14-16). For women with dense breasts, ultrasound imaging yields an incremental cancer detection rate. However, there are issues related to high false-positive rates, operator dependency of the examination and inability to image most DCIS. For women with the highest risk of developing breast cancer, screening MRI is adopted to provide higher screen sensitivity. However, considerable cost (i.e., larger than $50,000 per cancer) is added. PET scan can provide physiological information on the uptake of glucose and its metabolism, both of which are increased in malignant tissue (17). Combined PET/CT systems are increasingly available, which fuse PET and CT images to provide combined physiologic and anatomic imaging (18). However, both PET and CT are not used for primary tumor detection (invasive tumor with diameter smaller than 1 cm) and they are recommended for detection of metastases and recurrent disease in breast cancer (17, 18).

1.3 Optical Imaging for Breast Tumor

Optical imaging is currently emerging as a promising new addition to medical imaging, which provides biologists and clinicians new ways to detect, diagnose and study disease (19). Optical microscopy imaging with high spatial resolution for cancer research

has been paid much attention in the past few decades (20-23). Laser scanning confocal fluorescence microscopy provides high resolution, depth resolved, 3-D images (24). Two-photon fluorescence microscopy has later been invented which reduced photo damage compared with fluorescence confocal microscopy and achieves even higher spatial resolution and deeper penetration into tissues (20). Optical coherence tomography, which is analogous to ultrasound, performs high resolution cross-sectional imaging of tissue scattering (21, 22). While these techniques are all extremely useful, they have a common limitation. They can only be used to image tissue near the surface. Confocal microscopy penetrates up to depths of about 50 μm. Two-photon microscopy allows one to look slightly deeper, up to hundreds of micrometers. OCT goes even deeper, but only to depths of at most 2-3 mm in highly scattering tissue. The shallow imaging depth inhibits the use for non-destructive *in vivo* imaging of breast tumor.

On the other hand, macroscopic imaging allows for larger fields of view and deeper depths of penetration ranging from millimeters to centimeters. Photoacoustic tomography (PAT) combines ultrasonic-scale resolution and penetration depth with high sensitivity to tissue light absorption (25-27). For breast tissue imaging, PAT can visualize vasculature inside the tissue by virtue of its high hemoglobin content compared to surrounding breast parenchyma (19, 28-30). However, most currently available PAT systems require the tissue and ultrasonic detectors to be in contact with a coupling fluid, complicating experimental procedures. Diffuse correlation spectroscopy (DCS) and near-infrared spectroscopy (NIRS) have been developed to probe blood flow , hemoglobin concentration and oxygen saturation in deep tissue vasculature (several centimeters). A well-known 'biological window' exists in the NIR range (600-900 nm) (**Figure 1.2**),

wherein tissue absorption is relatively low, so that light can penetrate into deep/thick volumes of tissue (31). For imaging with NIRS/DCS (i.e., diffuse optical/correlation tomography [DOT/DCT]), multiple points on the tissue boundary are usually illuminated in a time-sharing fashion and diffuse light patterns are collected around the boundary using photodetector sets. NIRS/DOT has been used over decades to detect oxygenation alternations in breast tumors (32-36).

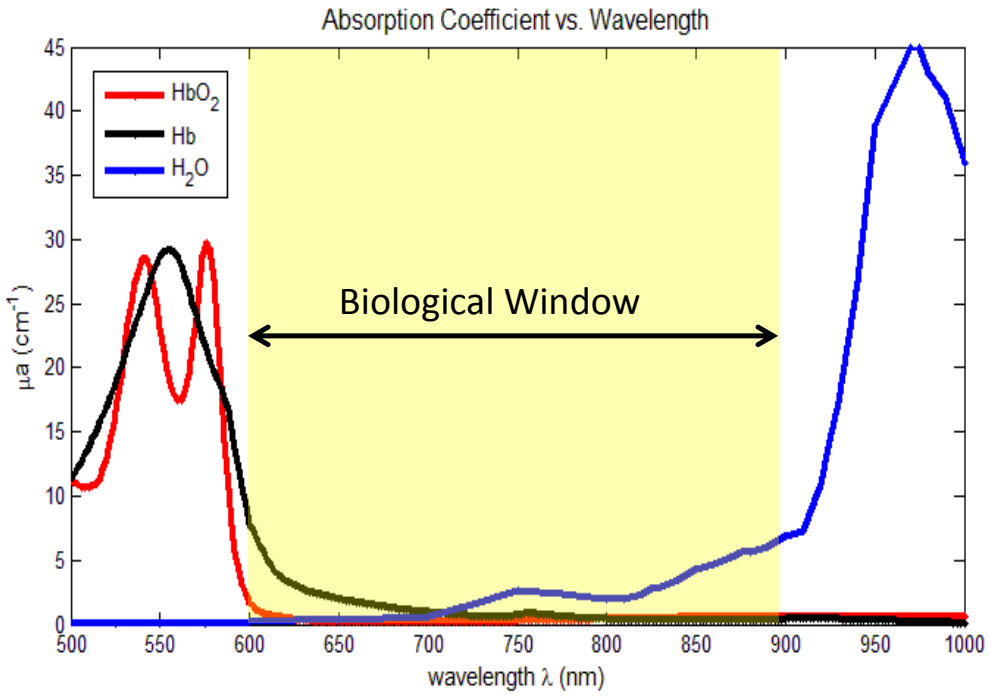

Figure 1.2: Absorption Spectra of Hemoglobin and Water. Tissue absorption coefficients (μa) shown as a function of wavelength (λ) for oxygenated hemoglobin (HbO_2), deoxygenated hemoglobin (Hb), and water (H_2O). Within the NIR spectral window (~600 – 900 nm), light is able to penetrate deep tissue due to low absorption.

1.4 Diffuse Correlation Spectroscopy (DCS)

DCS is an emerging new technique which provides direct measurement of blood flow index (BFI) in deep tissues (37-43). DCS takes advantage of the same biological window

as traditional NIRS techniques, but employs long-coherence (> 5 meter) NIR continuous-wave laser as the light source. DCS blood flow measurement is accomplished by monitoring speckle fluctuations of photons resulting from moving scatterers in biological tissues. Moving red blood cells (RBCs) inside vessels are primarily responsible for these fluctuations. In most dynamic experiments, the temporal statistics of light speckle fluctuations are monitored and the electric field temporal autocorrelation function or its Fourier transform is quantified. Using a correlation diffusion equation describing the propagation of electric field temporal autocorrelation function through tissues, the measured signal is then related to the motion of RBCs and, consequently, BFI is determined. Relative change in blood flow (rBF) can then be determined by normalizing BFI to its baseline value (e.g. before physiological change). DCS provides several attractive new features for blood flow measurement in tissue microvasculature, including noninvasiveness (i.e., no ionizing radiation, no contrast agents), high temporal resolution and relatively high penetration depth (up to several centimeters (44)).

DCS technology has been extensively validated in various tissues through comparisons with laser Doppler flowmetry (45, 46), Doppler ultrasound (47, 48), power Doppler ultrasound (49, 50), Xenon-CT (51), fluorescent microsphere flow measurement (52), and arterial spin labeled magnetic resonance imaging (39, 44).

Since measurements of blood flow provide insight about oxygen delivery and the clearance of metabolic by-products (53), *in vivo* diffuse optical measurement of blood flow has been explored for tumor characterization and prediction of treatment outcomes (54). A few pilot studies of breast tumors using DCS have found increased blood flow inside the tumor in contrast to surrounding normal tissues (53, 55). Real-time monitoring

of breast tumor blood flow response to neoadjuvant chemotherapy also demonstrated the potential of DCS for assessing cancer therapies (56, 57).

1.5 Current Study Limitations and Thesis Outline

Despite advances in DCS technologies, there have been limited imaging applications of DCT for tumor detection. An early probe-tissue contact based DCT approach was applied to tissue phantoms (58), but was disadvantaged in vivo due in part to compression-induced hemodynamic alterations. A few noncontact-based DCT examinations have been conducted using the camera lenses positioned between a sample and optical fibers connected to source and detection elements (59, 60). These arrangements, however, were only tested on the brain of small animals with limited probing depth (< 5 mm). Another limitation of these imaging studies was their reliance on analytical solutions that assumed a simple semi-infinite flat tissue geometry. As such, there have been no reports of studies using DCT for 3-D imaging of blood flow distributions in tumors (54).

The focus of my graduate work is to develop a novel noncontact DCT (ncDCT) system for 3-D imaging of tumor-to-normal blood flow in deep tissues and apply the system to clinical diagnosis of breast tumors. I have contributed to the development of DCT theory, to the design and validation of the imaging system (computer simulations and tissue phantom experiments) and to the clinical applications of diffuse optical techniques (patients with breast tumors). In addition, I have also explored the use of different mode fibers for photon collection to improve the signal-to-noise ratio (SNR) of DCS flow-oximeter measurements. In this thesis, I summarize these technique

developments and report our first step to adapt the ncDCT system for 3-D imaging of blood flow contrasts in human breast tumors.

This thesis is organized into the following chapters. Chapter 2 describes the theoretical background of NIRS and DCS and the development of DCT for 3-D flow contrast imaging. Chapter 3 depicts the ncDCT instrumentation, measurement procedures and initial validation work on tissue-like phantoms under semi-infinite geometry. The recipes and fabrication procedures for making liquid and solid phantoms are also included in the appendix. In Chapter 4, further computer simulations are performed to characterize the performance of ncDCT system for imaging an anomaly (tumor) with varied flow contrasts and depths inside the tissue volumes with breast-shaped surface boundaries. Chapter 5 presents in vivo imaging results of blood flow distribution in 28 human breast tumors using ncDCT. Chapter 6 demonstrates the possibility of improving SNRs of DCS flow-oximeter measurements using single-, few- and multi-mode fibers for detection. Finally, chapter 7 summarizes the novelties of the present work, my contributions to the field, study limitations as well as directions for future research.

CHAPTER 2 DIFFUSE CORRELATION SPECTROSCOPY AND TOMOGRAPHY: THEORY

2.1 Introduction

In this chapter I provide a theoretical background for the traditional diffuse optical techniques, including NIRS for tissue optical properties and consequently absolute oxygenation measurements (**Chapter 2.2**) and single-wavelength DCS for flow monitoring (**Chapter 2.3**). Contributions to further development of DCS/DCT technologies are then presented including (1) an ncDCT technique for 3-D flow imaging of deep tissue based on finite element framework (**Chapter 2.4.1**) and (2) a noise model for ncDCT for evaluating the influence of measurement noises on image reconstruction accuracy (**Chapter 2.4.2**).

2.2 NIRS

The 'biological window' in NIR (600-900 nm, see **Figure 1.2**) has made possible the application of diffuse optical imaging and spectroscopy in biological tissues. In this window, the absorption coefficients (μ_a) of water and hemoglobin are low, allowing photons to travel deeply into tissues (millimeters to centimeters depending on the wavelength used and tissue optical properties) (61). However, due to the factor that reduced scattering length ($1/\mu_s' \approx 1\,mm$) is much shorter than the absorption length ($1/\mu_a \approx 100\,mm$), scattering events dominate the propagation of photons inside the tissue. Beyond a few millimeters deep inside tissue, the photons may have been scattered

multiple times and their directions become random. Thus, the photon propagation in tissue over a long distance can be treated as a diffusive process (62, 63).

The propagation of photons in highly scattering media such as biological tissues can be modeled by the diffusion approximation to the radiative transport equation (63, 64). This diffusion equation, which governs the photon fluence rate, $\Phi(\boldsymbol{r},t)$ $[Watt \cdot cm^{-2}]$ inside the medium, is written in the frequency domain (FD: using modulated light as the source) as follows (63, 65):

$$\nabla \cdot \big(D(\boldsymbol{r})\nabla\Phi(\boldsymbol{r},t)\big) - \upsilon\mu_a(\boldsymbol{r})\Phi(\boldsymbol{r},t) + \upsilon S(\boldsymbol{r},t) = \frac{\partial\Phi(\boldsymbol{r},t)}{\partial t} \qquad (2.1)$$

Here, $\boldsymbol{r}$ is the position vector, t [s] is time and υ $[\mathrm{cm} \cdot s^{-1}]$ is the speed of light in the medium. $\mu_a(\boldsymbol{r})$ $[cm^{-1}]$ is the absorption coefficient, and $D(\boldsymbol{r}) \equiv v/3\big(\mu_a(\boldsymbol{r}) + \mu_s'(\boldsymbol{r})\big) \approx v/3\mu_s'(\boldsymbol{r})$ $[cm^2 \cdot s^{-1}]$ is the photon diffusion coefficient, where $\mu_s'(\boldsymbol{r})$ $[cm^{-1}]$ is the reduced scattering coefficient of the tissue. $S(\boldsymbol{r},t)[Watt \cdot cm^{-2}]$ is the isotropic source term which gives the number of photons emitted at position **r** and time t per unit volume per unit time. The right hand side of **Equation 2.1** shows the change rate of photons within a sample volume. This rate equals the number of photons scattered into the volume per unit time from its surroundings, minus the number of photons absorbed per unit time within the volume, plus the number of photons emitted per unit time from any sources in the volume (65). This diffusion approximation is valid when $\mu_a \ll \mu_s'$ and the distance between sources and detectors is much greater than the random walk step length (~ 1 mm in breast tissue).

For point sources of the form $S(\boldsymbol{r},t) = S_0\delta(\boldsymbol{r}-\boldsymbol{r}_s)\exp(-\mathrm{i}\omega\mathrm{t})$, where S_0 is a constant, ω is the modulation frequency and r_s is the source location**,** **Equation 2.1** simplifies to (66):

$$\nabla\cdot\left(\left(\frac{D(\boldsymbol{r})}{v}\right)\nabla\Phi(\boldsymbol{r})\right)-\left(\mu_a(\boldsymbol{r})+\frac{i\omega}{v}\right)\Phi(\boldsymbol{r}) = S_0\delta(\boldsymbol{r}-\boldsymbol{r}_s) \qquad (2.2)$$

where $\Phi(\boldsymbol{r},t) = \Phi(\boldsymbol{r})\exp(-\mathrm{i}\omega\mathrm{t})$.

To apply the NIR technique for measuring tissue absorption and scattering, photodetectors were typically used to detect the diffused light at known distances of a few millimeters to centimeters from point sources. **Figure 2.1a** shows a simple measurement setup with one pair of source and detector in reflection geometry. Light injected into the tissue through a source fiber can be detected by the detector fiber placed at a distance ρ from another fiber. The sensitive region of diffuse light is usually described as a "banana pattern" with the penetration depth of ~ρ/2 (65, 67, 68) (see **Figure 2.1a**). The analytical solution for **Equation 2.2** in this semi-infinite geometry can be obtained (69):

$$\Phi(\rho) = \frac{vS_0}{4\pi D}\left(\frac{\exp(-Kr_1)}{r_1}-\frac{\exp(-Kr_2)}{r_2}\right) \qquad (2.3)$$

where $K^2 = 3\mu_s'(-\frac{i\omega}{v}+\mu_a)$, $r_1 = \sqrt{\rho^2+z_0^2}$ and $r_2 = \sqrt{\rho^2+(z_0+2z_b)^2}$, ρ is the distance from the source to detector measured along the sample surface, z_b is the distance above the tissue surface at which the fluence rate extrapolates to zero and z_0 is the effective depth of the source. We use $z_0 = 1/\mu_s'$ and $z_b = \frac{2}{3\mu_s'}\frac{1+R_{eff}}{1-R_{eff}}$, $R_{eff} = -1.44n^{-2}+0.71n^{-1}+0.668+0.064n$, $n \approx 1.33$(for both tissue and phantom). The

R_{eff} term accounts for the mismatch between the medium and the air indices of refraction with n being the ratio between them.

Multidistance measurements of the phase and the amplitude of the photon fluence rate $\Phi(\boldsymbol{r}, t)$ with FD system enable to extract optical properties (μ_s' and μ_a) of the measured medium by fitting the known analytical solution (**Equation 2.3**) to the measured boundary data (70-72). In the NIR region, the dominant chromophore in tissue is hemoglobin (deoxyhemoglobin Hb and oxyhemoglobin HbO_2). Since the absorption spectra of Hb and HbO_2 are different (see **Figure 1.2**) (62), the concentrations of [Hb] and [HbO_2] in biological tissue can be calculated by knowing μ_a at two wavelengths (46, 73). Total hemoglobin concentration (THC) and blood oxygen saturation (StO_2) can be derived based on [Hb] and [HbO_2] consequently.

Besides the modulated light used in the FD system, there are other two types of light sources commonly used in diffuse optics: continuous-wave (CW) and time-resolved (TR) (see **Figures 2.1b-2.1d**) (19, 74). The simplest type is CW light where the light intensity remains constant over time. CW systems enable fast data acquisition and the use of simple detectors and detection electronics, but cannot determine μ_a and μ_s' simultaneously. The FD paradigm uses intensity modulated light to illuminate the tissue, and measures both light intensity attenuation and phase shift at the detector, allowing simultaneously determination of μ_a and μ_s'. The TR light source delivers short light pulses to the medium, which are temporally broaden as they propagate through the medium. At the detector, the detected temporal pulse shape contains the information to determine μ_a and μ_s'. TR system yields more output than other two modalities but require more complicated equipment and data analysis.

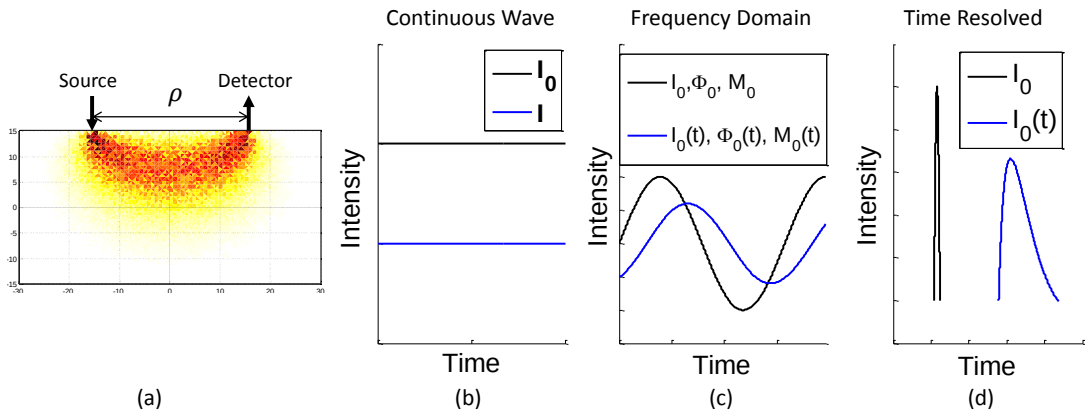

Figure 2.1: Sample input and output intensity signals representing the three types of NIRS techniques. Panel (a) is computer simulated "banana pattern" showing the sampled volumes in the reflection geometries. Panel (b) shows a CW NIRS, in which attenuated intensity of continuous illumination is monitored. Panel (c) shows FD NIRS, in which input light is modulated and the amplitude attenuation and phase shifts are detected. Panel (d) shows TR NIRS, in which an impulse of light is emitted into the tissue, and the intensity change with respect to time is detected. Here, I_0 and I represent input and detected intensities, Φ_0 represents phase, and M_0 represents the frequency of modulation.

2.3 DCS

Similar to CW NIRS, DCS also utilizes NIR light and the same measurement geometry to probe deep tissue properties. While NIRS employs the static method of diffuse optical technique to detect slow intensity variations induced by tissue absorption and scattering, DCS uses the dynamic method to monitor the fast motion of red blood cells.

When using DCS to detect tissue blood flow, a pair of source and detector fibers is usually placed along the tissue surface with separation distance of a few millimeters to centimeters. NIR light generated by a CW long coherent laser (coherence length > 5 m) emits into tissues through the source fiber. The diffused light transported throughout the tissue is detected by a single or few-mode fiber connected to a single-photon-counting

detector. Photons travel inside tissue in a diffusive manner (45, 65), and experience absorption by tissue absorbers (e.g., hemoglobin and water) and, more often, scattering by static or dynamic scatterers (e.g., organelles, mitochondria, moving red blood cells) (see **Figure 2.2a**). The motions of moving scatterers cause temporal fluctuations in light intensity, leading to changes in the speckle pattern of interference (38, 41, 54, 58, 65, 67, 75-78). In most dynamic experiments the temporal statistics of light speckle fluctuations are monitored and the electric field temporal autocorrelation function or its Fourier transform is quantified. Using a correlation diffusion equation describing the propagation of electric field temporal autocorrelation function through tissues, the measured signal is then related to the motion of RBCs and, consequently, blood flow is determined.

The normalized light intensity temporal autocorrelation function is calculated to characterize these speckle intensity fluctuations at multiple delay time τ:

$$g_2(\boldsymbol{r},\tau) = \langle I(\boldsymbol{r},t)\cdot I(\boldsymbol{r},t+\tau)\rangle / \langle I(\boldsymbol{r},t)\rangle^2 \tag{2.4}$$

Here $I(\boldsymbol{r},t)$ is the detected light intensity at position $\boldsymbol{r}$ and time t, and $\langle\cdots\rangle$ denotes a time average (38). Faster intensity fluctuations, which are associated with higher blood flow, correspond to steeper decay in $g_2(\boldsymbol{r},\tau)$ curve (**Figures 2.2b** and **2.2c**).

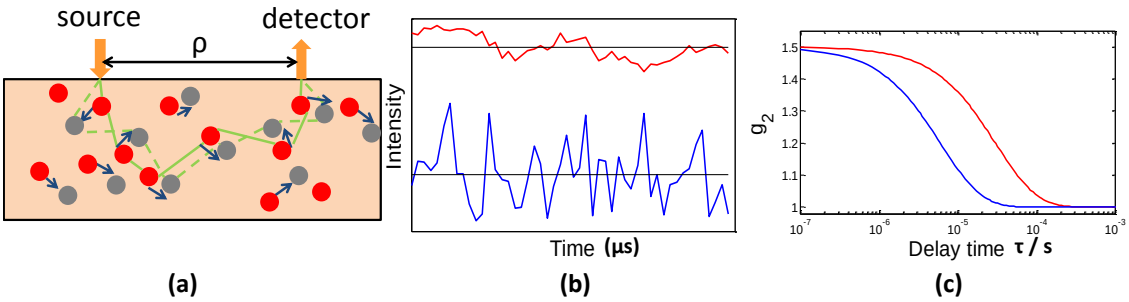

Figure 2.2: (a) Schematic for multiple scattering along a single photon path in a turbid media with semi-infinite reflection geometry. Solid green line indicates the photon path at time t, while the dashed green line represents the photon path at time t+τ. The red and grey disks indicate blood cell at time t and t+τ, the blood cell is scattered certain distance during the delay time τ (indicated by blue arrows). (b) Example of detected light intensity fluctuations from measurements with higher (blue curve) and lower (red curve) blood flow. (c) Normalized intensity autocorrelation functions $g_2(\boldsymbol{r},\tau)$ calculated from detected light intensities in (b). The decay of the intensity autocorrelation function curves is related to the tissue blood flow.

In order to extract blood flow information from measured $g_2(\boldsymbol{r},\tau)$ curve, the normalized electric field temporal autocorrelation function $g_1(\boldsymbol{r},\tau) = G_1(\boldsymbol{r},\tau)/G_1(\boldsymbol{r},0)$, which contains the information of red blood cell motion, is derived with a correlation diffusion approach (65). The blood flow index (BFI) is ascertained by fitting the analytical expression of $g_1(\boldsymbol{r},\tau)$ to the experimentally measured $g_2(\boldsymbol{r},\tau)$ using the Siegert relation (79):

$$g_2(\boldsymbol{r},\tau) = 1 + \beta|g_1(\boldsymbol{r},\tau)|^2 \tag{2.5}$$

Here, $\beta = 1/N$ is a coherence factor depending mainly on the laser coherence and detection optics, and is inversely proportional to the number of guided modes/speckles (N) (80). It can be determined experimentally from measured $g_2(\boldsymbol{r},\tau)$ via $\beta = g_2(\boldsymbol{r},\tau) - 1$.

The analytical expression of $g_1(\boldsymbol{r},\tau)$ is converted from the electric field temporal autocorrelation function $G_1(\boldsymbol{r},\tau) = \langle E(\boldsymbol{r},t)\cdot E^*(\boldsymbol{r},t+\tau)\rangle$. In order to model the

propagation of $G_1(\boldsymbol{r},\tau)$ in biological tissues, the correlation diffusion equation in homogeneous medium for CW light source is developed (38, 58, 81):

$$\nabla\left(\left(\frac{D(\boldsymbol{r})}{v}\right)\nabla G_1(\boldsymbol{r},\tau)\right)-\left(\mu_a(\boldsymbol{r})+\frac{1}{3}\mu_s'(\boldsymbol{r})k_0^2\alpha\langle\Delta r^2(\tau)\rangle\right)G_1(\boldsymbol{r},\tau)=-S_0\delta(\boldsymbol{r}) \qquad (2.6)$$

where v is the light speed in the medium, $S_0\delta(\boldsymbol{r})$ is the CW source term and S_0 is a constant, $k_0=2\pi n/\lambda$ is the wave number of the incident light, n = 1.33, λ is the source light wavelength, and $D(\boldsymbol{r})\approx v/3\mu_s'(\boldsymbol{r})$. $\langle\Delta r^2(\tau)\rangle$ is the mean square displacement of the moving scatterers inside the tissue during a time interval τ. A Brownian diffusion model $\langle\Delta r^2(\tau)\rangle=6\,D_B(\boldsymbol{r})\tau$ is often employed with $D_B(\boldsymbol{r})$ denoting the *effective* diffusion coefficient of the moving scatterers (66, 82). $D_B(\boldsymbol{r})$ depends on the exponential decay rate of the measured correlation functions. An α term (ranging from 0 to 1) is added to account for the fact that not all scatterers in biological tissues are dynamic, and α is defined as the ratio of moving (dynamic) scatterers to total (dynamic and static) scatterers. The combined term, $\alpha D_B(\boldsymbol{r})$, is referred to as the blood flow index (BFI) in tissues and its relative change is commonly used to calculate the relative change of blood flow (rBF) compared with the baseline BFI before physiological changes. In contrast to tissue samples, all scatterers in liquid phantom solutions are considered dynamic with $\alpha\approx 1$, and the flow index is thus reported as simply $D_B(\boldsymbol{r})$.

The analytical solution of **Equation 2.6** with point source impinging upon a semi-infinite homogeneous medium (**Figure 2.2a**) is generated as (65):

$$G_1(\rho,\tau)=\frac{vS_0}{4\pi D}\left(\frac{\exp(-K(\tau)r_1)}{r_1}-\frac{\exp(-K(\tau)r_2)}{r_2}\right) \qquad (2.7)$$

where $K^2(\tau) = 3\mu_s'\mu_a + {\mu_s'}^2 k_0^2 \alpha \langle \Delta r^2(\tau) \rangle$, r_1, r_2 and ρ are the same as in **Equation 2.3**. Consequently, the analytical expression for $g_1(\boldsymbol{r}, \tau)$ is derived as:

$$g_1(\boldsymbol{r}, \tau) = \left(\frac{\exp(-K(\tau)r_1)}{r_1} - \frac{\exp(-K(\tau)r_2)}{r_2}\right) \Big/ \left(\frac{\exp(-K(0)r_1)}{r_1} - \frac{\exp(-K(0)r_2)}{r_2}\right) \quad (2.8)$$

Thus the measurements of $g_1(\boldsymbol{r}, \tau)$ can be fitted the analytical expression based on **Equation 2.8** to yield αD_B, using given values of ρ and values of μ_s', μ_a from NIRS measurements or literature (65, 66, 83).

2.4 Diffuse Correlation Tomography (DCT)

The extension of DCS to DCT is comparable to that of DOS to DOT which models the propagation of light in diffuse tissue, called "forward problem", based on **Equation 2.1** and solves the "inverse problem" for spatial distribution of optical parameters (e.g., μ_a and μ_s') (60, 84). Similarly, the forward problem for DCT is to calculate the electric field autocorrelation at the detectors given a geometric model of the optical parameters, flow index, and source and detector locations and functionality based on **Equation 2.6**. The inverse problem for DCT is to recover the flow index distribution through boundary measurements of autocorrelation function.

Previous studies involving DCT have used perturbation method to derive the forward problem (58-60), however, this method relies on analytical solution of autocorrelation function which precludes the transition to complex boundaries and imperfect heterogeneities. The finite element framework has been applied in DOT as a numerical approximation of partial differential **Equation 2.1** for light propagation model and image

reconstruction algorithms. This numerical method can resolve the geometry and heterogeneity limitations for DOS/DOT (85-87). Because of the mathematical similarity of correlation diffusion equation (**Equation 2.6**) and photon diffusion equation (**Equation 2.2**), the implementation of finite element framework in DCS/DCT has been developed (37)， adopting software package NIRFAST (for DOT) (87) as a shortcut.

Recall **Equation 2.6**, the term $\frac{1}{3}\mu_s'(\boldsymbol{r})k_0^2\alpha\langle\Delta r^2(\tau)\rangle$ can be reshaped as $\mu_a^d(\boldsymbol{r},\tau) = 2\mu_s'(\boldsymbol{r})k_0^2\alpha D_B(\boldsymbol{r})\tau$, and is considered as "effective dynamic absorption" due to dynamic processes on the correlation with τ (37). DCT is conceptualized as a formulation of DOT which computes $G_1(\boldsymbol{r},\tau)$ instead of photon fluence rate $\Phi(\boldsymbol{r},t)$, by updating "static absorption" $\mu_a(\boldsymbol{r})$ to $\mu_a^{total}(\boldsymbol{r},\tau) = \mu_a(\boldsymbol{r}) + \mu_a^d(\boldsymbol{r},\tau)$, and reconstructing $\mu_a^{total}(\boldsymbol{r},\tau)$ instead of $\mu_a(\boldsymbol{r})$ only (37).

2.4.1 Forward and Inverse Models

Chart 1 and **Chart 2** illustrate the main commands executed for solving the forward and inverse problems respectively in DCT using NIRFAST. A homogeneous background tissue volume mesh with assigned initial optical properties of $\mu_a(\boldsymbol{r})$ and $\mu_s'(\boldsymbol{r})$ is first generated in the forward solution (see **Chart 1**). All S-D pairs corresponding to the actual or simulated scanning of ncDCT probe are placed on the surface of the background mesh. However, only those with valid links between sources and detectors are configured as effective pairs for image reconstruction. For simulations, an anomaly region (mimicking a tumor) inside the background volume mesh is defined and assigned a BFI contrast relative to the surrounding background. Based on the designed distributions of BFIs, $\mu_a^{total}(\boldsymbol{r},\tau)$ is updated for each voxel inside the entire tissue volume within a certain

range of τ. The autocorrelation functions $G_1(\boldsymbol{r},\tau)$ for multiple τ values from all effective S-D pairs are then calculated by running the forward model. The boundary BFI data at all effective S-D pairs are then extracted by fitting $G_1(\boldsymbol{r},\tau)$ to the analytical expression of **Equation 2.7** under semi-infinite homogeneous geometry.

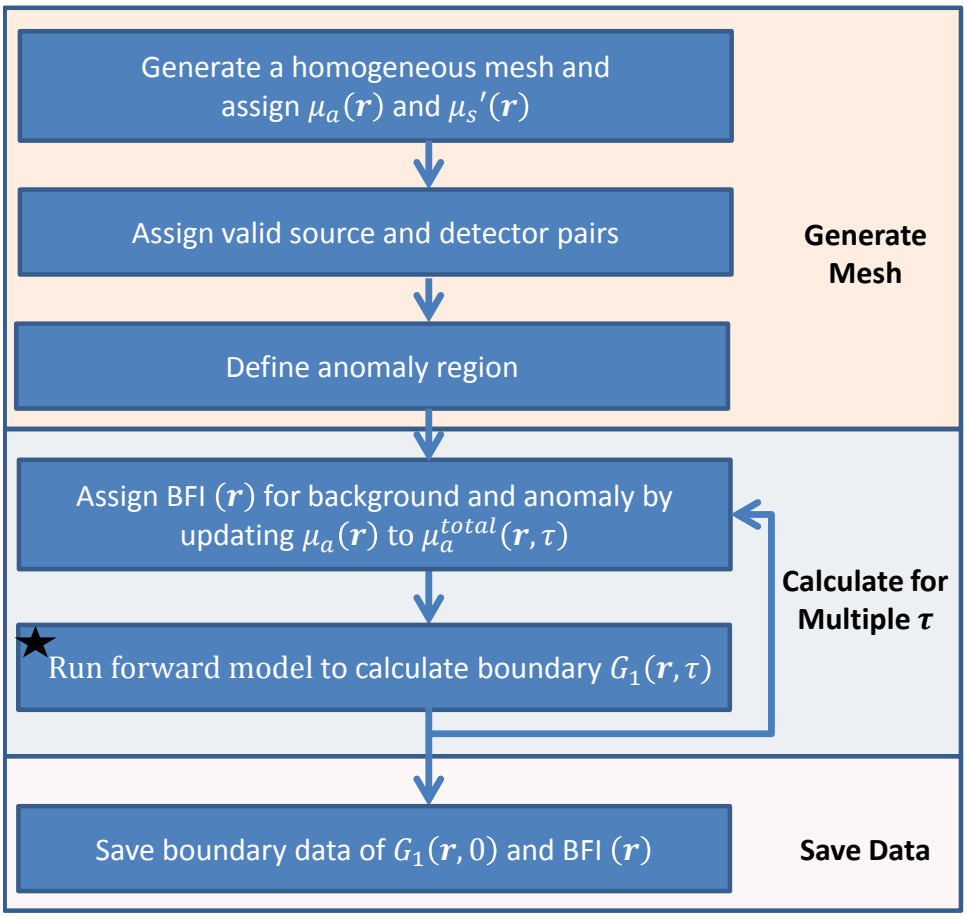

Chart 1: Flowchart outlining the sequence and commands used in the modified NIRFAST to generate a forward model for ncDCT.

Solving the inverse problem for image reconstruction is conducted on a second mesh with a coarse finite element division (pixel basis) (87, 88) (see **Chart 2**). Initial values of background BFI and optical properties ($\mu_a(\boldsymbol{r})$ and $\mu_s'(\boldsymbol{r})$), along with the selected τ are

assigned to generate a homogeneous inverse mesh. The simulated or measured boundary BFI data are converted to $g_1(\boldsymbol{r},\tau)$ at the selected τ using the semi-infinite analytical expression of **Equation 2.8** (67, 83, 89, 90), and further converted to $G_1(\boldsymbol{r},\tau)$ by multiplying with $G_1(\boldsymbol{r},0)$. The boundary $G_1(\boldsymbol{r},\tau)$ functions are then input into the inverse model to reconstruct the $\mu_a^{total}(\boldsymbol{r},\tau)$ distribution inside the entire tissue volume. The BFI distributions are finally extracted through the definition of $\mu_a^d(\boldsymbol{r},\tau)$. Note that even though we can reconstruct $\mu_a^{total}(\boldsymbol{r},\tau)$ distribution directly from the simulated or measured boundary $G_1(\boldsymbol{r},\tau)$ data, we chose to extract boundary BFI values first and then convert them back to $G_1(\boldsymbol{r},\tau)$ for image reconstruction. This seemingly redundant procedure is yet essential for the normalization of BFIs in real measurements (see **Chapter 5.2.3**) as well as reducing the noise influence on the measured $G_1(\boldsymbol{r},\tau)$.

2.4.2 Noise Model for DCT

To evaluate noise influence on image reconstruction through simulations, randomized noise varying at different τ are generated based on a noise model originally derived for DCS (83, 91). The noise level depends on the detected photon count rate (i.e., light intensity) at each S-D pair, which is estimated using the light intensity detected from in vivo tissues (e.g., breast tissue). This noise is applied to the simulated $g_2(\boldsymbol{r},\tau)$ curves. Multiple $g_2(\boldsymbol{r},\tau)$ curves with noise are generated for each S-D pair and then averaged to improve the signal-to-noise ratio. This simulation mimics our in vivo measurements and data averaging process. Finally, $g_2(\boldsymbol{r},\tau)$ curves are converted to $G_1(\boldsymbol{r},\tau)$ to generate boundary BFI data.

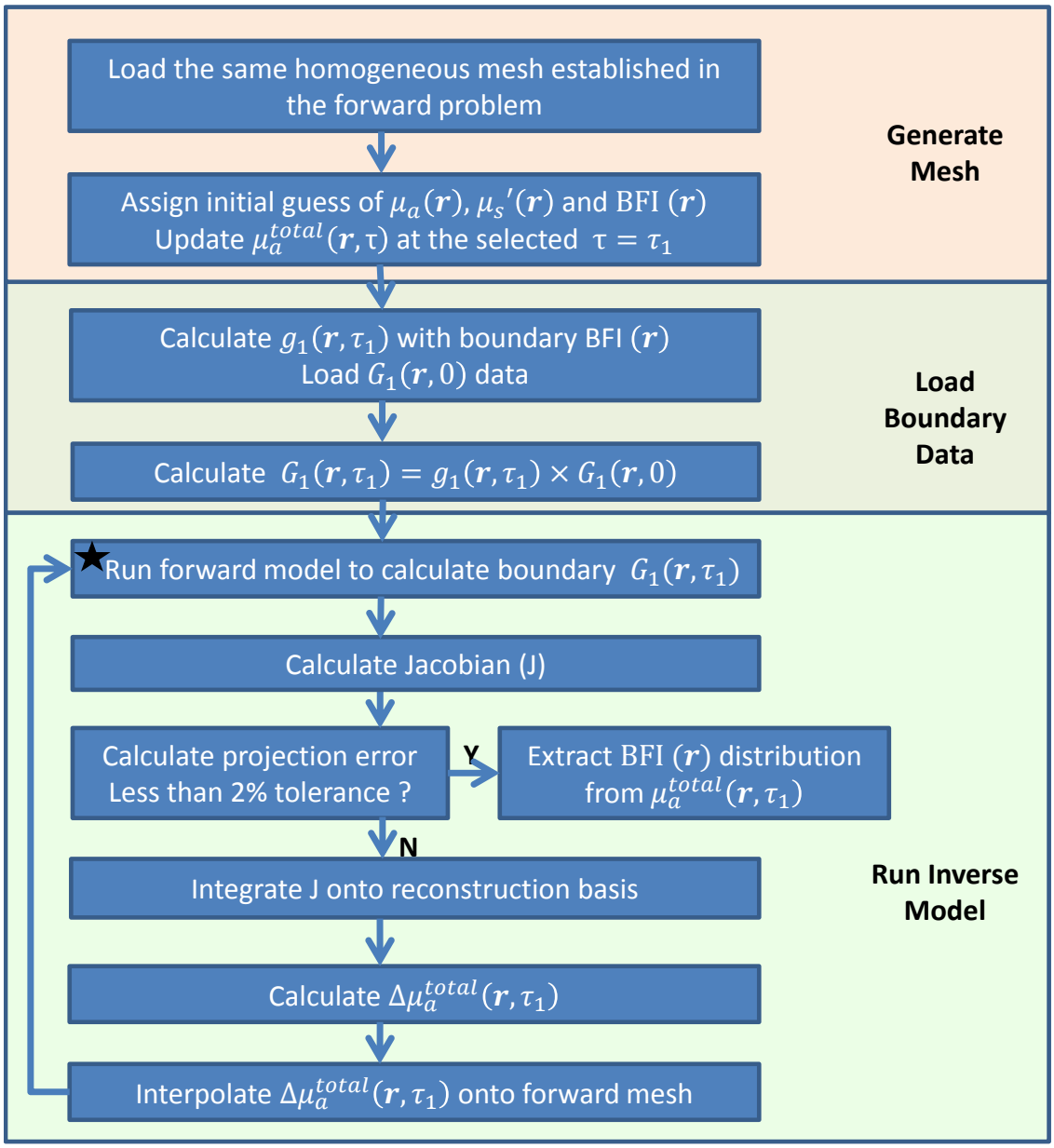

Chart 2: Flowchart outlining the sequence and commands used in the modified NIRFAST to solve DCT inverse problem.

CHAPTER 3 NONCONTACT DIFFUSE CORRELATION TOMOGRAPHY (NCDCT) SYSTEM

3.1 Introduction

Most DCS systems employ contact-based interaction with the sample. However, in tissues, contact measurements can promote hemodynamic variations induced by probe compression or disturbing sensitive areas. Our lab has recently developed a noncontact DCS system that uses a lens-focusing technique to avoid the contact influence (89, 92). The probing depth of the noncontact DCS measurement was fixed due to the single source-detector (S-D) separation design. To further extend the DCS technique to tomographic imaging, an ncDCT system has recently been developed. The ncDCT probe has multiple S-D measurement pairs (10-30 mm S-D separations) and the system employs a motorized stage for automatic and precise scanning over the region of interest (ROI) (37). In addition, the finite-element-method based facilitation of DCT image reconstruction as mentioned above enables blood flow imaging on arbitrary boundary geometries. Finally, validation efforts have been made including computer simulations and phantom tests. The unique noncontact imaging system remedies many of the concerns mentioned at beginning of the thesis (**Chapter 1.3**).

In this chapter, the ncDCT system instrumentation is first presented in **Chapter 3.2**. **Chapter 3.3** describes the procedures to perform blood flow imaging, which includes ncDCT scanning (**Chapter 3.3.1**) and FD NIRS measurements (**Chapter 3.3.2**). To validate the imaging capability of the ncDCT system, computer simulations and tumor-like phantom experiments with varied flow contrasts are provided based on a simple slab-shaped tissue boundary (i.e., semi-infinite geometry) (**Chapter 3.4**) (37). Since liquid

(Intralipid solution) and solid phantoms (silicone) are commonly used in instrument calibration/characterization and algorithm validation, the fabrication procedures for phantoms are provided at the end of this section (**Chapter 3.5**).

3.2 ncDCT Instrumentation

Extending DCS to DCT attaches the burden of collecting many boundary measurements. As such, our noncontact probe was upgraded to have two identical laser source paths and one detector path configured in a linear array (**Figure 3.1c**). In each source path, output from a multimode source fiber (WF200/220/245, CeramOptec, MA, USA) connected to a laser (825 nm) on the DCS instrument is projected onto the tissue through lenses (**Figure 3.1a**). Fifteen single-mode detector fibers (SM800-5.6-125, Fibercore, CA, USA) are equally arranged in a 7 mm line to cover a 20 mm range through the magnification of lenses (**Figure 3.1c**). The S-D separations vary from 10 to 30 mm, thus enabling up to ~15 mm penetration depth (37). Two long coherence lasers at 825 nm (coherence length >5 m, CrystaLaser, NV, USA) emit light to tissue through individual source paths, alternatively. The photons traveling through the tissue sample are collected by the detector array of 15 avalanche photodiodes (APD, Perkin Elmer, Canada) through the detector path. A multi-channel autocorrelator (Correlator.com, NJ, USA) takes the APD outputs and calculates 15 intensity correlation functions simultaneously (**Figure 3.2a**). A motorized stage (CR1-Z7, Thorlabs, NJ, USA) is integrated into the optical system which rotates the ncDCT probe around the nipple for scanning a ROI on the breast surface (**Figure 3.1a**). A linear stage (5236A16, McMASTER-CARR, IL, USA) and a custom-made rotational platform were used to manually align the axis of probe

head at the center of ROI and perpendicular approximately to the breast tissue surface (**Figure 3.1a**). The outcomes from this scanning are the boundary data of intensity autocorrelation functions collected at hundreds of S-D pairs on the ROI.

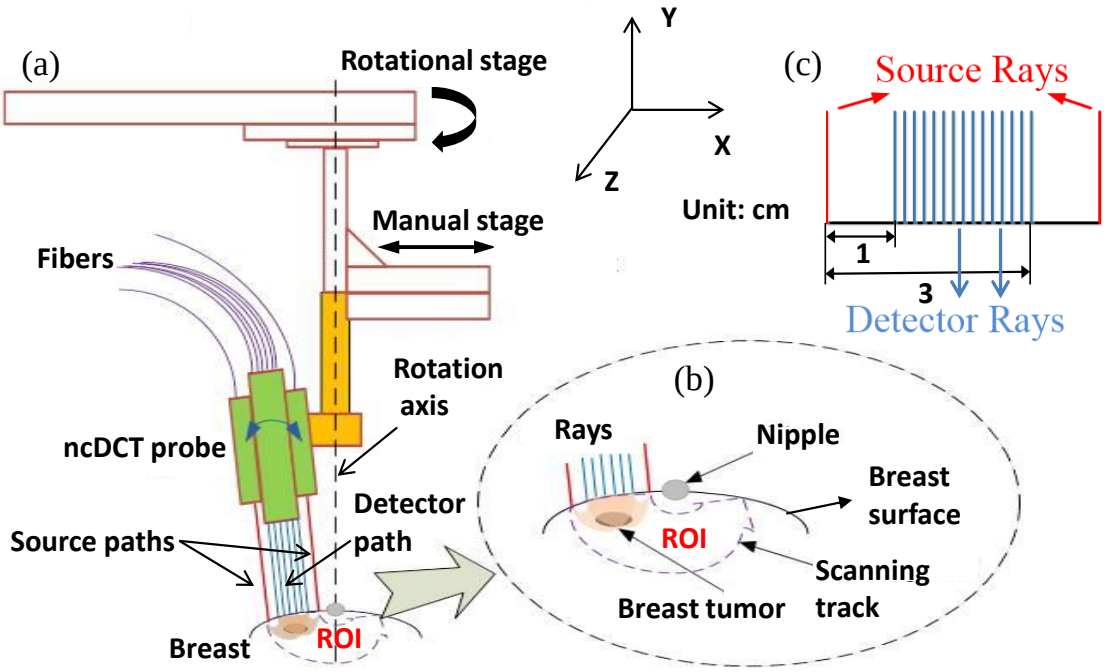

Figure 3.1: The schematic diagram of ncDCT scanning system. (a) A motorized rotational stage was used to scan over a representative ROI on the breast and the rotation axis was aligned through the nipple; (b) During scanning procedure, the source and detector rays were perpendicular to the breast surface and rotationally scanned around the nipple to cover the tumor bearing ROI; (c) Fifteen single-mode detector fibers were equally projected onto breast surface to cover a 2 cm range while two multimode fibers were projected onto two sides of the linear arrays, enabling S-D separations to span from 1cm to 3 cm.

3.3 Blood Flow Imaging Protocols

3.3.1 ncDCT Scanning

To demonstrate the scanning protocol for 3-D blood flow imaging in breast tissue, a plastic mannequin is placed on the bed to mimic patients lying in a supine position

(**Figure 3.2b**). A red mark made on the mannequin breast surface indicates a tumor beneath the skin surface. The rotation axis in the ncDCT probe (**Figure 3.1a**) is first aligned with breast nipple. The probe is then rotated to the top of the red mark and adjusted the working distance and projection angle to make the two source rays approximately perpendicular to the mannequin breast surface. In order to scan over the ROI, the probe is rotated back to the first scanning position and then scans certain degrees over a ROI through multiple steps with a 3-degree increment per step. The first and last scanning steps cover healthy breast tissue and the middle step is usually on top of the lesion mark. Total scanning time was ~25 minutes with 60 s sampling time per step at 1 Hz DCS sampling rate for each laser source. During the scanning process, two projected source pairs at the first and last steps are marked on the breast surface using a marker pen.

3.3.2 Commercial 3-D Camera Scanning

After ncDCT probe scanning, a commercial 3-D camera (NextEngine, CA, USA) is used to take the surface geometry of the mannequin breast with source and rotation center marks. The working distance is ~17 inch from breast surface, the field of view (FOV) is 10″ × 13″ (**Figure 3.2b**), and the total acquisition time is ~5 minutes. After that, the mannequin is removed and a small foam pad perpendicular to the rotation axis is attached to ncDCT probe as a reference plane (RP) (**Figure 3.2c**). The 3-D camera is used to take an image of the RP to co-register the two coordinate systems: ncDCT system and 3-D camera, which enables the alignment of the scanned source and detector locations onto the breast-shaped mesh. The sequence of taking RP image by 3-D camera is after all

measurements in *in vivo* measurement due to busy clinical workflow and it is described in later chapter (**Chapter 5.2.2**).

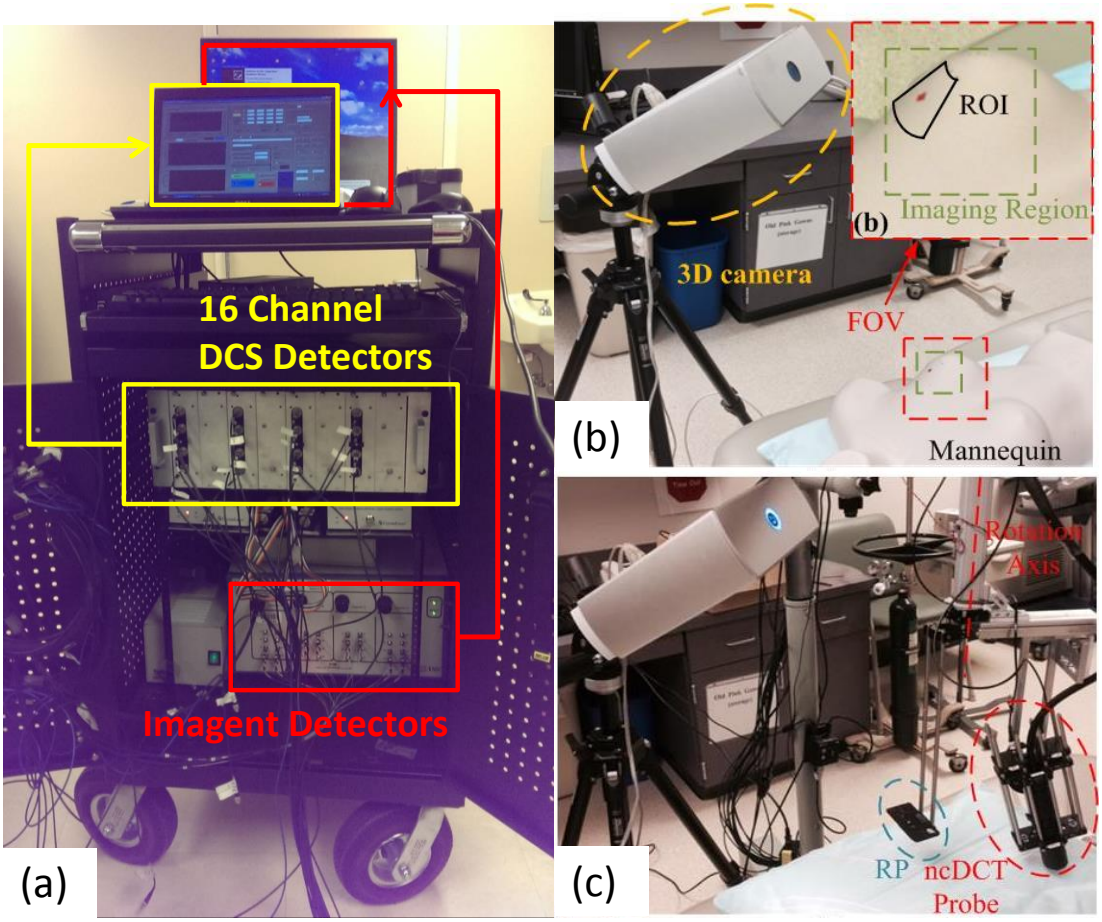

Figure 3.2: (a) Photo of the combined ncDCT imaging system and a commercial frequency-domain tissue oximeter for tissue optical properties measurement. (b) The breast surface with source marks was imaged by the 3-D camera. (c) After the mannequin was removed, a small foam pad was attached to the DCS scanner. The 3-D camera took another image to include the small foam pad whose surface (RP) was adjusted perpendicularly to the rotation axis. The RP was used for the co-registration of two coordinates: 3-D camera and ncDCT system.

3.3.3 Frequency-domain NIRS Measurements

Following the ncDCT measurement, a commercial FD tissue oximeter (Imagent, ISS, IL, USA) (71) was used to measure μ_s' and μ_a of the breast tissue. The Imagent instrument includes 110 MHz modulated sources at 4-wavelength (690, 750, 780, and 830 nm), photomultiplier tubes, and desktop computer control, which ultimately calculates tissue optical properties (μ_a and μ_s') (**Figure 3.2a**). Source and detector fibers are embedded in a black flexible probe and the probe is gently placed on the skin surface to measurement breast tissue optical properties at certain positions. The measurement usually takes ~ 5 minutes.

3.4 ncDCT Validation Results

In this subsection, initial validation work including computer simulations and phantom experiments on slab-shaped geometry with linear probe scanning were performed to evaluate the accuracy of our ncDCT system. To test our theoretical DCT technique, computer simulation was first conducted in homogeneous situation (i.e., no anomaly) to evaluate the forward solution (**Chapter 3.4.1**). Computer simulations and phantom experiments embodied recovery of anomaly flow contrasts were performed to further evaluate the inverse solution (**Chapter 3.4.2**). Background optical properties mismatch was also induced in computer simulations and phantom experiments to evaluate their crosstalk on reconstructed flow contrasts (**Chapter 3.4.3**).

3.4.1 Forward Solution Validation

A slab mesh simulating liquid phantom solution [dimension (mm): 90 (*H*) × 90 (*W*) × 35 (*D*)] was first generated in SolidWorks® (Dassault Systemes, MA, USA) and then segmented into finite elements using ANSYS® (ANSYS, PA, USA). A total of 73949 nodes were created with node distances of 2 mm. The segmented mesh nodes and elements information were then input into MATLAB® (MathWorks, MA, USA) to generate all mesh files needed for the simulations with NIRFAST. Optical properties were set throughout at $\mu_s' = 8.00$ cm^{-1} and $\mu_a = 0.045$ cm^{-1} close to breast tissue values (93). The blood flow index (BFI) for the background was set as 1×10^{-8} cm^2/s close to Intralipid phantom values (58, 67). The noncontact probe scanned linearly (mimicked in simulation) across the ROI in 15 steps with an increment of 4 mm/step generating a scanning area of 40 mm × 56 mm and 450 (15 steps × 15 APDs × 2 sources) effective S-D pairs (**Figure 3.3**). The forward solution (i.e., $G_1(\boldsymbol{r}, \tau)$) was calculated by the modified NIRFAST with τ from 0 to 8×10^{-6} s. Minimal simulation aberrations over the measured ROI (1% mean discrepancy and 1.45% standard deviation) were observed between BFI extracted using the established semi-infinite analytical solution (37) in **Equation 2.6** (**Chapter 2**) and the assigned BFI. The computer simulation validated the algorithm for calculating forward solution using **Equation 2.6** based on NIRFAST.

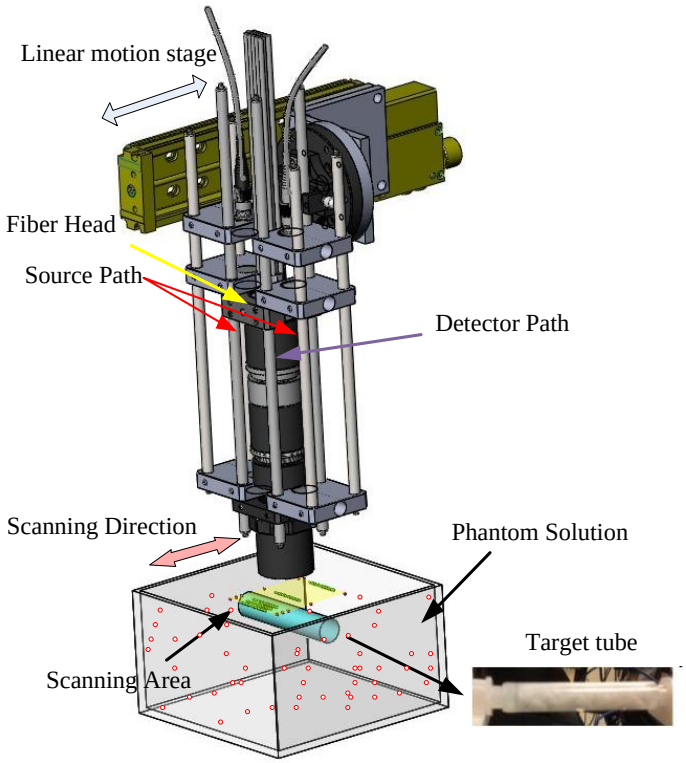

Figure 3.3: Illustration of the ncDCT system linearly scanning across the ROI of liquid phantom surface with a pump-connected cylindrical tube placed inside the tank.

3.4.2 Inverse Solution Validation

Computer Simulations. A cylindrical tube-shaped anomaly [dimension (mm): 13 (Dia.) × 80 (L)] was inserted beneath the middle of the ROI with a depth of 12.5 mm from the tube center to the ROI surface (**Figure 3.3**). The μ_a and μ_s' inside the anomaly were matched to the background tissue. The attributed anomaly BFI was increased from 0-fold to 20-fold at 4-fold increment per step. Reconstruction was conducted on the same mesh with a pixel basis of $20 \times 20 \times 25$ (node number: 11,025) and at selected delay time $\tau_1 = 3.2 \times 10^{-6}$ s. Due to limited ROI dimensions along the tube, only partial anomaly reconstruction was possible (**Figure 3.4a**). For percentage flow change

comparison, the reconstructed anomaly peak flow value was normalized to the averaged step differences of BFI. Both the shape (**Figure 3.4a**) and relative anomaly peak flow contrast changes (**Figure 3.4b**) were well reconstructed (regression slope = 1.00, R^2 = 1.00 and $p < 10^{-5}$). The anomaly was extracted with the full width half-maximum (FWHM) criterion (94) on the reconstructed DCT image. The averaged BFI of the reconstructed anomaly was computed by averaging the BFIs within the anomaly. An excellent linear relationship was also observed between the reconstructed and assigned percentage flow changes (data are not shown; regression slope = 1.00, R^2 = 1.00 and $p < 10^{-5}$).

Phantom Experiments. A background of tissue-like liquid phantom was placed in an aquarium and a pump-connected cylindrical tube anomaly was filled with liquid and small pieces of solid phantom (**Figure 3.3**). The tissue-like liquid phantom (**Chapter 3.5.1**) was comprised of Intralipid, distilled water and India ink, and has been used extensively for DCS calibrations (92). Intralipid particles (Fresenius Kabi, Sweden) provide control of scattering (μ_s') and Brownian motion (D_B; $\alpha \approx 1$) while India ink controls absorption (μ_a). We set $\mu_s' = 8.10\, cm^{-1}$ and $\mu_a = 0.044 cm^{-1}$ while quantifying them with Imagent (**Figure 3.2a**). To create flow index contrasts against the background, a clear plastic tube [dimension (mm): 13.5 (*Dia.*) × 80 (*L*)] with a very thin wall (0.35 mm) was placed at ~12.5 mm (tube center to ROI surface) into the background liquid phantom (**Figure 3.3**). The tube was mostly filled with small pieces of solid phantom ($\mu_s' = 10.00$ cm^{-1} and $\mu_a = 0.10$ cm^{-1}) to randomize pumped particle motions as Brownian motion and generate a diffusive circumstance for photons. Solid phantoms were comprised of titanium dioxide, silicon and carbon black (**Chapter 3.5.2**). A

peristaltic pump (HV-77201-60, Cole Parmer, IL, USA) connected in series with a hydraulic capacitor that damped fluid pulsations was employed to create step increases in steady flow from 0 to 20 ml/min at 4 ml/min increments within the tube. The noncontact probe was first calibrated to the homogeneous liquid phantom region. The scanning procedure was linear as assumed in simulations. Total scanning time was ~20 minutes with 60 s sampling time per step at 0.5 Hz DCS sampling rate for each laser. We used identical reconstruction parameters as the simulation including slab mesh and delay time τ_1 with the exception of a median filter application. This latter addition assisted in stabilizing inherent experimental noise not encountered in the ideal simulation (87). The relationship between macro pumped flow (unit: ml/min) and micro particle motion (αD_B unit: cm^2/s) is complicated, but was confirmed linear (95). For this case the assigned flow represents the macro flow (pump speed) rather than DCS indices. **Figure 3.4d** presented relative macro and micro flow changes using the same way as in simulations. A tube-shaped anomaly was clearly observed after image reconstruction (**Figure 3.4c**). The reconstructed flow indices accurately captured the flow changes in the tube when quantified with the peak value (**Figure 3.4d**; linear regression slope = 0.97, R^2 = 1.00 and $p < 10^{-5}$) and with the mean of extracted anomaly (data are not shown; linear regression slope = 0.99, R^2 = 0.96 and $p < 10^{-3}$).

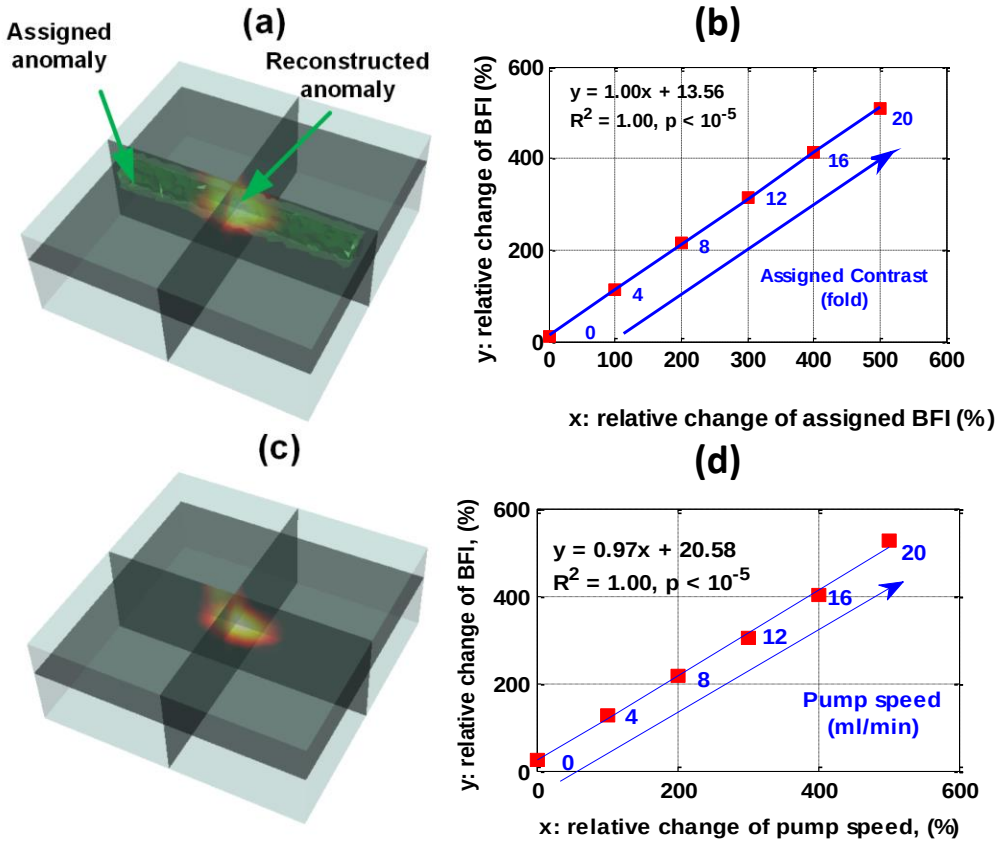

Figure 3.4: Results of computer simulation and phantom experiment utilizing a homogeneous slab background and internally placed tube-shaped anomaly of varied flow contrast. The reconstructed anomaly from the last step with highest flow contrast is shown (a) 3-D overlaid on the assigned anomaly and (c) in the phantom experiment. Both (b) and (d) show a linear relationship between the assigned anomaly and reconstructed flow indices expressed as ratios of relative changes respectively in the simulation and phantom experiment. 3-D data are displayed with open source visualization software PareView (Kitware, NY, USA).

3.4.3 Influence of Optical Property Mismatch on ncDCT Accuracy

We note that no optical property mismatch between anomaly and background was induced, i.e., $\Delta\mu_s' = 0$ and $\Delta\mu_a = 0$, in the computer simulations and phantom tests performed earlier. However, our previous published studies have showed that the mismatch of μ_a and μ_s' can result errors in estimating DCS flow index (67). In the

following computer simulation and phantom experiments, the influence of μ_a and μ_s' mismatch on ncDCT flow contrast reconstruction is presented below.

The Influence of μ_s' on DCT. Recall that $\mu_s' = 8.00$ cm^{-1} and $\mu_a = 0.045$ cm^{-1} in the previous experiments. In this computer simulation, the μ_s' of background was changed to 3.2 cm^{-1} to generate a 250% μ_s' contrast (8.0/3.2) in the anomaly. For the phantom experiment, the new background μ_s' was accomplished by adjusting the concentration of Intralipid and was measured/verified by Imagent. Flow indices were reconstructed under two experimental conditions: (1) assign homogenous optical properties in the forward and inverse solutions ($\mu_a = 0.045\ cm^{-1}$, $\mu_s' = 8.0\ cm^{-1}$) for both the anomaly and background; (2) assign separate property values for the anomaly ($\mu_a = 0.045\ cm^{-1}, \mu_s' = 8.0\ cm^{-1}$) and background ($\mu_a = 0.045\ cm^{-1}, \mu_s' = 3.2\ cm^{-1}$) in the forward solution and use a homogenous mesh ($\mu_a = 0.045\ cm^{-1}, \mu_s' = 3.2\ cm^{-1}$) for image reconstruction. The differences in the reconstructed flow index contrasts between the two conditions were compared.

Figure 3.5 shows the computer simulation results. In **Figure 3.5a**, the reconstructed flow index contrasts under Condition #2 were normalized to those under Condition #1 for comparisons. The underestimations of μ_s' contrasts under Condition #2 (i.e., assuming $\mu_s' = 3.2\ cm^{-1}$ in the anomaly) resulted in similar overestimations (ratios) of flow contrasts at different flow levels. However, the relative changes of flow contrasts over the large range of flow variations were not influenced by the incorrect assumptions of μ_s' (**Figure 3.5b**). **Figure 3.6** shows the phantom experimental results, which are very similar to those in computer simulations (**Figure 3.5**).

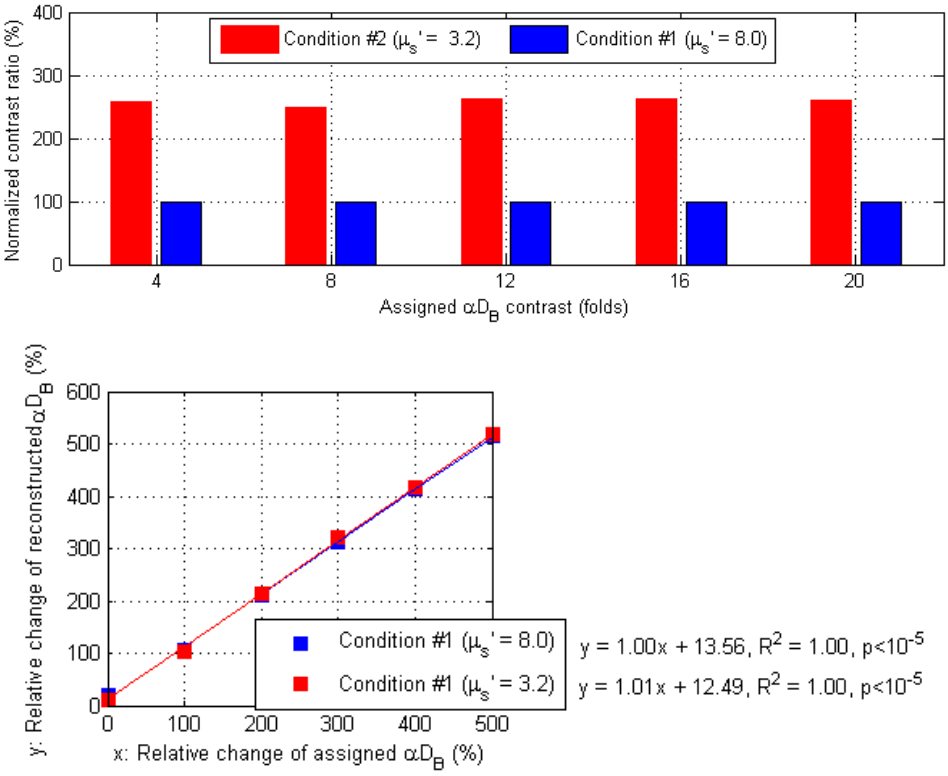

Figure 3.5: Computer simulation results. **(a)** The underestimations of μ_s' in the anomaly generated the overestimations of flow contrasts (red bars). **(b)** Linear relationships between the assigned and reconstructed flow index contrasts expressed as ratios of relative changes reconstructed under Condition #1 (blue dots) and Condition #2 (red dots).

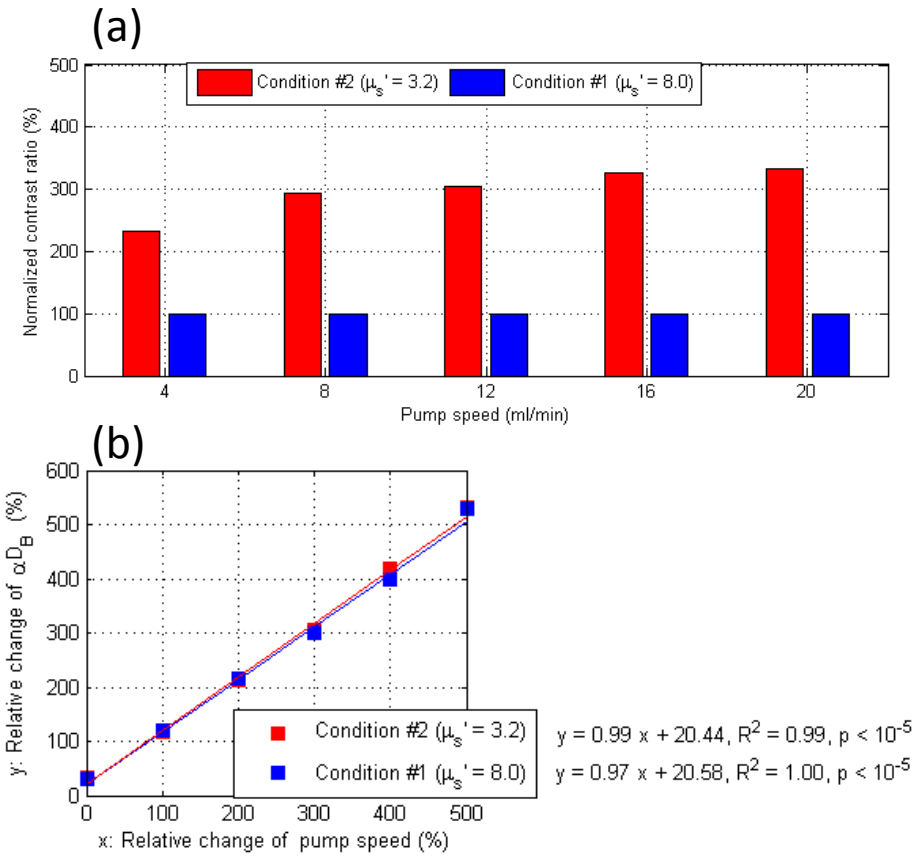

Figure 3.6: Phantom experimental results. **(a)** The underestimations of μ_s' in the anomaly generated the overestimations of flow contrasts (red bars). **(b)** Linear relationships between the assigned and reconstructed flow index contrasts expressed as ratios of relative changes reconstructed under Condition #1 (blue dots) and Condition #2 (red dots).

The Influence of μ_a on DCT. Similar to the evaluation of μ_s' influence, we use computer simulations to set up 2- and 3-fold contrasts of anomaly μ_a with the background. In the reconstruction, we ignored the variations of μ_a in the anomaly ($0.09\ \mathrm{cm}^{-1}$ and $0.135\ \mathrm{cm}^{-1}$) and reconstructed flow contrasts using the background optical properties ($\mu_a = 0.045\ cm^{-1}$ and $\mu_s' = 8.0\ cm^{-1}$). Reconstructed flow contrasts were normalized to the homogeneous case (i.e., no μ_a anomaly/background contrast). **Figure 3.7** shows that the underestimations of μ_a contrasts resulted in the

underestimations in flow contrasts (**Figure 3.7a**). However, the relative changes of flow index contrasts over the large range of flow variations were not influenced by the incorrect assumptions of μ_a (**Figure 3.7b**).

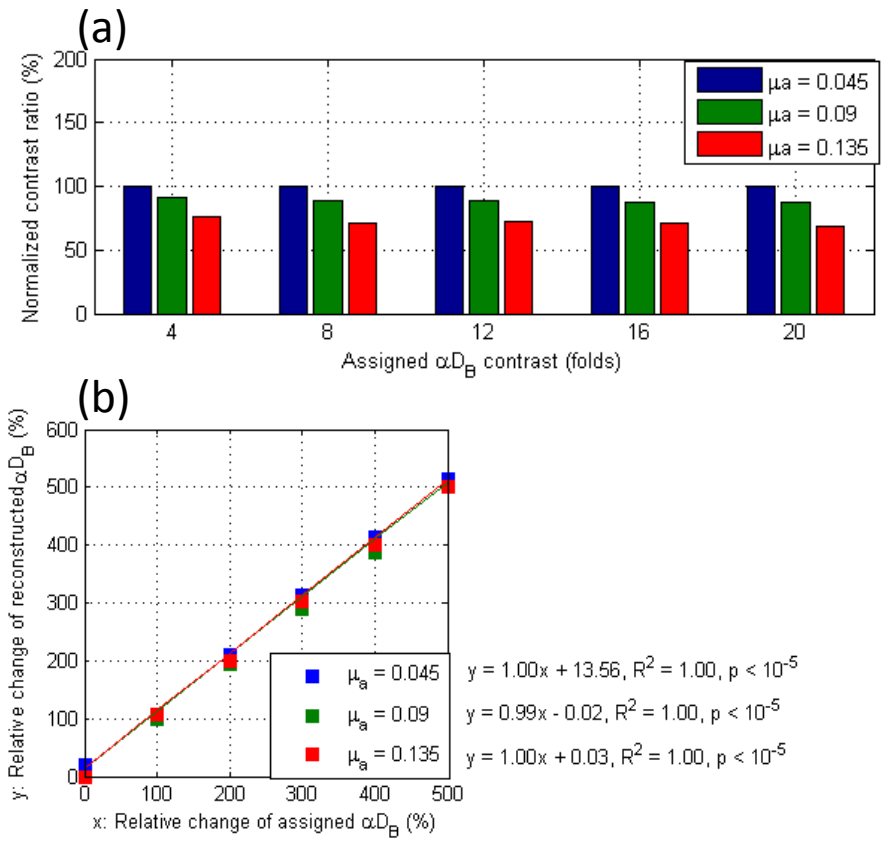

Figure 3.7: Computer simulation results. **(a)** The underestimations of μ_a generated the underestimations of flow contrasts (green and red bars). **(b)** Linear relationships between the assigned and reconstructed flow indices expressed as ratios of relative changes reconstructed using different μ_a values.

In summary, inaccurate μ_s' assumptions resulted in much greater flow index errors than inaccurate μ_a assumptions. Specifically, ~250% underestimation of μ_s' led to $245 \pm 2\%$ overestimation of flow indices in simulations and $297 \pm 40\%$ overestimations in phantom experiments, whereas 200% to 300% underestimation of μ_a led to $11.5 \pm 2\%$ to $26 \pm 3\%$ underestimations of flow indices, respectively. All these results are

consistent with our previous studies using DCS (67, 83). Nevertheless, the relative changes of flow index contrasts over the large range of flow variations can be accurately reconstructed even with the incorrect assumptions of optical properties.

3.5 Discussion and Conclusions

In this chapter, the instrumentation of our newly developed ncDCT system for 3-D blood flow contrast imaging was reported. A plastic mannequin was used to demonstrate the blood flow imaging protocol for breast tumor detection. The procedures to collect breast boundary blood flow index and surface geometry were described in detail.

We further validated the ncDCT system for the flow contrast imaging using computer simulations and tissue phantom tests. The results indicated that the cylindrical tube-shaped anomaly inside homogenous background tissue can be clearly reconstructed and high correlation was observed between the reconstructed and assigned anomaly flow contrast. We also found inaccurate μ_s' assumptions resulted in much greater flow index contrast errors than inaccurate μ_a. These findings suggest that investigations involving significant μ_a and μ_s' changes should concurrently measure flow indices and optical properties for avoiding over/underestimation of flow indices. However, the relative changes of reconstructed flow index contrasts can be accurately reconstructed even with the incorrect assumptions of optical properties.

In conclusion, a novel ncDCT system was built for blood flow contrast imaging in deep biological tissue. The imaging capability was validated through both computer simulations and phantom experiments based on slab-shaped geometry with linear scanning protocol.

3.6 APPENDIX: Recipes for Making Tissue-like Phantoms

Optical phantoms are constructed to mimic the optical absorption and scattering, and particle Brownian motion (only liquid phantom) of tissue. In our lab, liquid and solid phantoms are made to provide a tissue model for probe calibrations, titration experiments and testing image reconstruction algorithms.

3.6.1 Liquid Phantom Creation: Intralipid

In our lab, distilled water, India ink (Black India 44201, Higgins, MA) and Intralipid (30%, Fresenius Kabi, Uppsala, Sweden) are utilized in constructing liquid phantoms which provide a homogeneous tissue model (41, 67, 92). India ink is used to manipulate μ_a (λ) and has minimal influence on phantom scattering. The μ_a (λ) values at certain wavelengths are calculated based on the concentration of India ink. Intralipid is used to control μ_s' (λ) via changing its concentration and provides particle Brownian motion (D_B; $\alpha \approx 1$). The absorption of the lipid particles is negligible. Distilled water contributes little to both absorption and scattering, allowing for larger phantom volumes to facilitate satisfying the semi-infinite geometry model. Based on the desired values of μ_a (λ) and μ_s' (λ) for the phantom, the liquid phantom creation procedure is given bellow.

Calculation of Ink Volumes for Desired Absorptions. The India ink needs to be diluted to 10% concentration (or lower concentration, which depends on the volume of the aquarium holding liquid phantom), due to the very high absorption of pure India ink. The absorbance of the 10% ink solution should be measured with the spectrometer (Beckman Coulter, CA, USA). Since the 10% ink solution is not within the measurable range of our spectrometer, it is further diluted to 0.025% concentration. Multiple samples

of 0.025% ink solution are measured by spectrometer at 690, 750, 780 and 830 nm (matching the Imagent source wavelengths) and the measured absorbance is further converted to absorption coefficient by the equation: $\mu_a(\lambda) = \ln(10) \times Absorbance\ (\lambda)$ (9). This $\mu_a(\lambda)$ is for 0.025% concentration ink solution. Therefore, one needs to multiply $\mu_a(\lambda)$ by a factor of 400 for the absorption coefficient of 10% ink solution ($\mu_{a\ ink}(\lambda)$). As Intralipid is primarily comprised of water, it is assumed to have an absorption coefficient equivalent to water ($\mu_{a\ water} = \mu_{a\ Intralipid}$). The $\mu_{a\ water}(\lambda)$ values at those wavelengths can be obtained from the literature (96). Knowing the desired value of absorption coefficient for the phantom ($\mu_{a\ phantom}(\lambda)$) and the volume of total phantom solution ($V_{phantom}$), the volume of 10% ink solution (V_{ink}) can be determined as:

$$\mu_{a\ water}(\lambda) \times \left(V_{phantom} - V_{ink}\right) + \mu_{a\ ink}(\lambda) \times V_{ink} = \mu_{a\ phantom}(\lambda) \times V_{phantom} \quad (3.1)$$

The volume of distilled water is simply the remaining volume to be filled (i.e., $V_{water} = V_{phantom} - V_{ink} - V_{Intralipid}$).

For the titration experiment, 10% ink solution is added to the phantom at each step to increase $\mu_{a\ phantom}(\lambda)$. The volume of 10% ink solution to be added is described by the following equation:

$$\mu_a^{before}{}_{\text{phantom}}(\lambda) \times V_{phantom}^{before} + \mu_{a_{\text{ink}}}(\lambda) \times V_{ink}^{add} = \mu_a^{after}{}_{\text{phantom}}(\lambda) \times \left(V_{phantom}^{after} + V_{ink}^{add}\right) \quad (3.2)$$

where the "before" and "after" indicate the procedure of adding ink solution.

Calculation of Intralipid Volume for Desired Scattering. According to van Staveren's Mie theory approximation (97), $\mu_s'(\lambda)$ of 10% Intralipid is given by the equations:

$$\mu_s = 2.54 \times 10^9 \times \lambda^{-2.4} \tag{3.3}$$

$$g = 1.1 - 0.58 \times 10^{-3}\lambda \tag{3.4}$$

$$\mu_s' = \mu_s(1 - g) \tag{3.5}$$

where λ is in [nm] and μ_s and μ_s' are in [cm^{-1}]. The $\mu_s'(\lambda)$ of 10% Intralipid multiplies a factor of three can generate $\mu_s'(\lambda)$ of 30% Intralipid (denoted as $\mu_{s\ Intralipid}'(\lambda)$). As there are expected to be no contributions to the phantom scattering by the 10% ink solution or distilled water, both are ignored in calculation. Knowing the desired value of reduced scattering coefficient ($\mu_{s\ phantom}'(\lambda)$), the volume of 30% Intralipid to be used can be calculated by equation:

$$\mu_{s\ Intralipid}'(\lambda) \times V_{Intralipid} = \mu_{s\ phantom}'(\lambda) \times V_{phantom} \tag{3.6}$$

3.6.2 Solid Phantom Creation: Silicone

Solid phantoms are useful for simulating tissue-like geometry and do not deteriorate as the liquid phantom. Among the choices of solid phantoms, there are mainly three kinds of phantom matrix, including gelatin, resin and room temperature vulcanization (RTV) silicone (98, 99). The gelatin (also called agar) phantom is the cheapest, however, it is the least usable and can become fragile and crumble under applied stress. Both of the other two phantoms are stiff and stable. Their fabrication procedures and functions are very similar. Previous study showed by reducing the hardener in RTV silicone phantom,

stiffness of the phantom can be reduced, shaping this material into more biologically relevant configuration (100). In our lab, the RTV silicone phantom is used.

Soft rubber texture similar to stiff tissue phantom can be made out of silicone and used for years. Titanium dioxide (TiO_2) and carbon black are added to provide scattering and absorption contrast. Careful preparation is required for prevention of bubbles and proper curing. A recipe and fabrication procedure is listed below.

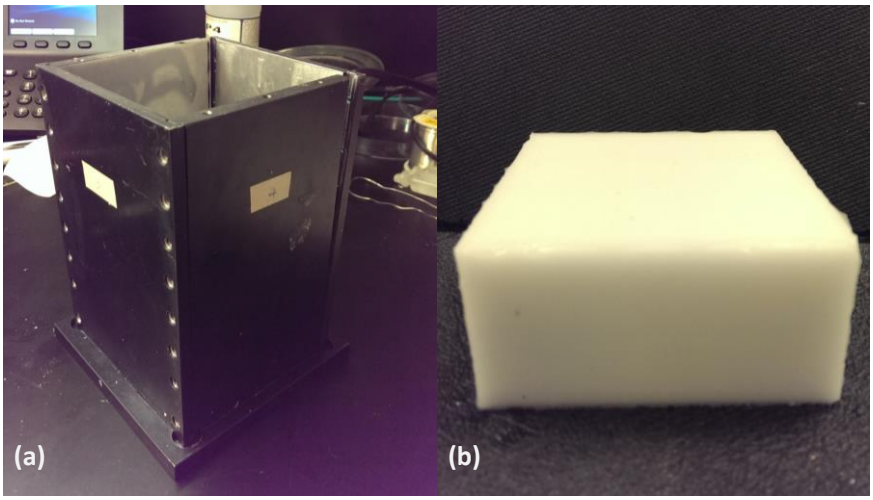

Figure 3.8: Photographs of (a) an empty mold that four facets can be disassembled and (b) a cured silicone phantom

RTV Silicone Phantom Recipe

Ingredients: 1. Silicone and hardener (RTV-615 silicone optical 2-part flow clear RTV SS4120-1P primer required, Circuit Specialists Inc, Mesa, AZ)

2. Scatterer (Titanium (IV) Oxide, Alfa Aesar, Chicago, IL)

3. Absorber (Carbon Black (99.9+% pure), Alfa Aesar, Chicago, IL)

Tools: 1. Mold (**Figure 3.8a**, do not use silicone or rubber molds)

2. Mixing bowl

3. Mortar and pestle for mixing TiO_2 and carbon black

4. Spatula for mixing silicone and hardener

5. Blender with at least a 0.25 HP motor and a 1 liter container

6. Balance (scales) with at least 0.01g mass resolution and weighing paper

7. Rubber gloves

8. Dust mask

9. Tight-lidded containers, suitable for long-term storage

10. Hair dryer

Assembly Sequence:

Since the amount of carbon black (CB) needed is tiny compared with TiO_2, we usually first make sufficient amount of 1:100 CB/TiO_2 mixture and then mix the CB/TiO_2 mixture with pure TiO_2 to achieve the expected optical properties.

1. Make the 1:100 carbon black (CB) / TiO2 mixture.

1) Weigh out 1.8 g TiO_2 and 0.2 g CB to make 1: 9 CB / TiO_2 mixture and mix them completely with mortar and pestle. Then transfer the mixture to a container.
2) Weigh $0.1*N$ g mixture made in 1) and $0.91*N$ g pure TiO_2 to make 1:100 CB / TiO_2 mixture. The mixture should be completely mixed with clean mortar and pestle. Then transfer the final mixture to a container and label it.

Because the exact ratio of CB to TiO_2 in a mixture is hard to control or determine, the absorptivity of each mixture must be found. (Since carbon black is very “sticky”

and very little is used, it is difficult to account for all the carbon black lost to the insides of the mortar/pestle, etc.)

2. Determine the absorptivity of the mixture in units of cm^{-1}·g^{-1}·306 g *silicone kit*.

1) Make a test silicone phantom with certain amounts of 1:100 CB/TiO_2 mixture and pure TiO_2. According to the experience, ~ 0.0446 g 1:100 CB/TiO_2 mixture and ~0.4177 g pure TiO_2 make $\mu_a \approx 0.061\ cm^{-1}$ and $\mu_s' \approx 10.3\ cm^{-1}$.
2) Measure the optical properties μ_a and μ_s' with the commercial frequency-domain tissue oximeter. Measured μ_a subtract 0.01 cm^{-1} is the μ_a contributed by CB at 750 nm wavelength (the μ_a of silicone is constant at ~0.01 cm^{-1}).
3) Divide the mass of the mixture used by the corrected absorption coefficient. This is the absorptivity of the CB/TiO2 mixture in units of cm^{-1}·g^{-1}·306 g *silicone kit*.

$$a_{CB/TiO2} = \frac{(\mu_a - 0.01)}{M_{CB/TiO2}} \tag{3.7}$$

where $a_{CB/TiO2}$ is the absorptivity, μ_a is the measured absorption coefficient, and $M_{CB/TiO2}$ is the mass of 1:100 CB/TiO_2 mixture used to make the test phantom. Here it is assumed that one 306 g *silicone kit* was used to make the phantom.

3. Make the solid phantom with target optical property

1) Calculate the mass of CB/TiO2 mixture needed according to the targeted μ_a of the phantom:

$$M_{CB/TiO_2} = \frac{(\mu_a - 0.01)}{a_{CB/TiO_2}} NK \tag{3.8}$$

where μ_a is the expected absorption coefficient, a_{CB/TiO_2} is the absorptivity of the CB/TiO2 mixture measured from the test phantom, and NK is the number of 306 g *silicone kit* used (can be fraction). Previous study using similar CB as absorbing agent

has reported the linear relationship between the mass of CB and phantom μ_a under $\mu_a = 0.1$ cm^{-1}(9).

2) Calculate the mass of TiO2 needed according to the targeted μ_s' of the phantom. The relationship between the mass of TiO_2 used and the μ_s' is roughly 0.024 cm^{-1}·g^{-1}·306 g *silicone kit*, at 750 nm wavelength.

$$M_{total-TiO_2} = \frac{\mu_s'}{0.024} \cdot NK \tag{3.9}$$

where $M_{total-TiO_2}$ is the mass of TiO_2, μ_s' is the targeted μ_s' and NK is the number of 306 g *silicone kit* used. The value, 0.024 is only a rough estimate based on previous phantom made with the same TiO_2 powder. Then the mass of pure TiO_2 added besides the CB/TiO_2 mixture is:

$$M_{added-TiO_2} = M_{total-TiO_2} - M_{CB/TiO_2} \tag{3.10}$$

3) Mix the CB/TiO2 mixture and pure TiO_2 powder.

Mix the new mixture completed in the mixing bowl. Then transfer it to the NK · 306 g silicone in the blender. Mix them for totally 10 min with 10 sec at each time.

4) Mix the silicone with hardener.

First, weigh $\frac{1}{10} \cdot NK \cdot 306$ g silicone hardener. It should be noted that reduce the amount of hardener may decrease the stiffness of the cured phantom. Then, transfer the mixture to a clean mixing bowl after the power and silicone mixture is completely cooled off and no bubbles left. The hair dryer on "cool" can be used to blow air on the surface of the phantom to break up any bubbles or foam. Slowly add the hardener to the silicone. Gently and thoroughly mix them with the spatula. Make sure no air bubble is induced.

5) Transfer the mixture equally into the phantom mold. Cover the mold with clean sheet and let it sit in the room temperature for ~1 day.
6) After the phantom is cured, disassemble the mold and remove the phantom. Since the cured phantom attaches the mold very tightly, it is not easy to remove the phantom from the mold. The mold we used is customized that the four facets can be disassembled.
7) Clean the tools.

Since the silicone is very viscous, it may flow very slowly. It cannot dissolve in the water. So to clean the blender, just place the blender bottle upside down in a place lined with a plastic bag overnight and most of the silicone may flow away.

CHAPTER 4 COMPUTER SIMULATIONS FOR NCDCT OF BREAST TUMORS

4.1 Introduction

The recently developed ncDCT in our laboratory provides a unique tool for three-dimensional (3-D) flow imaging of deep tissue (37). Initial validation efforts for the innovative ncDCT system have been made using computer simulations and tumor-like phantoms on a simple semi-infinite geometry (see **Chapter 3**). To translate this novel technique to clinical use for breast tumor imaging, the imaging ability of arbitrary boundaries (e.g., breast shape) is necessary. In this chapter, computer simulations are carried out to characterize the performance of ncDCT system for imaging an anomaly (tumor) with varied flow contrasts and depths inside the tissue volumes under breast-shape tissue boundary.

4.2 Computer Simulation Protocols

We conducted several computer simulations to characterize the performance of ncDCT system. The first simulation tested the abilities of ncDCT in recovery of an anomaly (tumor) beneath the surfaces of a slab and a female plastic mannequin breast (**Chapter 4.2.1**). The second simulation evaluated the reconstruction accuracies of the anomaly with varied depths and flow contrasts in the same plastic mannequin breast. The influence of noise on ncDCT image reconstruction was also assessed and compared with the results without noise (**Chapter 4.2.2**). The next simulation applied a priori structural knowledge of the anomaly in the inverse mesh to improve the accuracy of flow image reconstruction (**Chapter 4.2.3**). The last simulation evaluated the influence of different

delay time τ selection on ncDCT image reconstruction and the optimized τ selection was provided (**Chapter 4.2.4**).

4.2.1 Reconstruction of a Tumor in Slab-shaped and Breast-shaped Tissue Volumes

To evaluate the reconstruction of an anomaly inside a background tissue volume with a simple semi-infinite geometry, a slab volume [dimension (mm): 100 (*H*) × 100 (*W*) × 40 (*D*)] was first generated in SolidWorks and then segmented into finite elements using ANSYS. A total of 15996 nodes were created with node distances of 3 mm and 6 mm in the region of interest (ROI) and the surrounding region, respectively (**Figure 4.3a**). Different mesh resolutions were employed to reduce the total node number while maintaining appropriate spatial resolution in the ROI. The segmented mesh nodes and elements information were then input into MATLAB to generate all mesh files needed for the simulations with NIRFAST. The slab volume mesh represented a healthy background tissue volume. A spherical anomaly with a diameter of 10 mm mimicking a tumor was then placed at the ROI center and the anomaly centroid location was 7 mm beneath the surface of background tissue volume (**Figure 4.3a**). Optical properties for both tumor and background tissues were set homogeneous throughout the entire slab as $\mu_s' = 6.00\ cm^{-1}$ and $\mu_a = 0.06\ cm^{-1}$. The blood flow indices for the background and anomaly were set as $1 \times 10^{-8}\ cm^2/s$ and $10 \times 10^{-8}\ cm^2/s$, respectively, resulting in a 10-fold flow contrast between the tumor and surrounding normal tissues (**Figure 4.3c**). The ncDCT probe with a linear S-D array scanning rotationally over the ROI was simulated for 21 steps with 3 degrees per step to collect the boundary data (**Figure 4.3a**). There were totally 42 sources and 315 detectors distributed on the ROI according to the

scanning procedure. Thus, 630 (315×2) source-detector (S-D) pairs were effectively available and used for image reconstruction. The autocorrelation functions $G_1(\boldsymbol{r}, \tau)$ from the effective S-D pairs were calculated by the modified NIRFAST software with τ ranging from 0 to 3.2×10^{-5} s (50 consecutive τ values). Reconstruction was conducted on the same mesh with a pixel basis of $20 \times 20 \times 25$ and a $\tau_1 = 8.7 \times 10^{-6}$ s. The τ selection is discussed in the following section (**Chapter 4.2.4**). The presenting anomaly was extracted with the full width half-maximum (FWHM) criterion (94) on the reconstructed DCT image. The averaged BFI and the center location of the reconstructed anomaly were computed by averaging the BFIs and node coordinates within the anomaly.

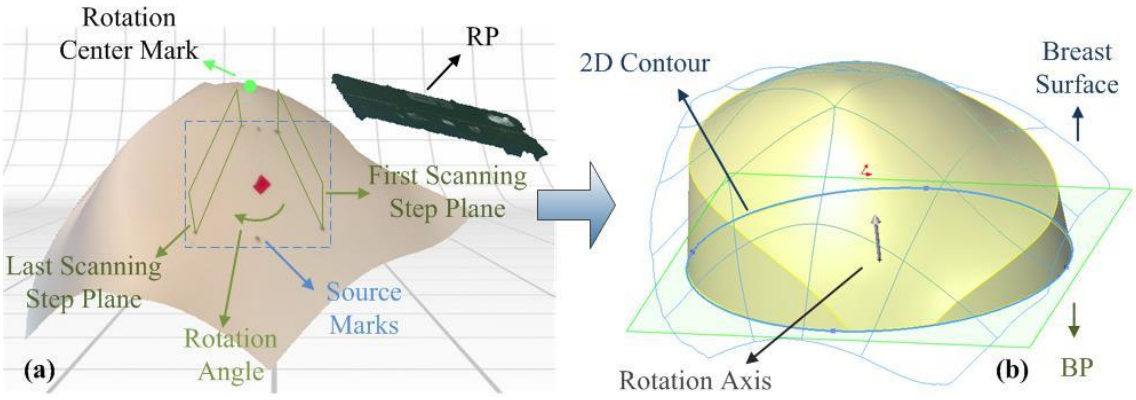

Figure 4.1: Procedures converting the breast surface image to a solid breast model. **(a)** 3-D surface geometry of mannequin breast and the reference plane (RP) recorded by 3-D camera. The lesion mark (red square), three pairs of source marks and the rotation center mark can be clearly seen. **(b)** A bottom plane (BP) parallel to the RP was created and a 3-D solid breast model was then generated by enclosing the 2-D contour of BP and the 3-D breast surface.

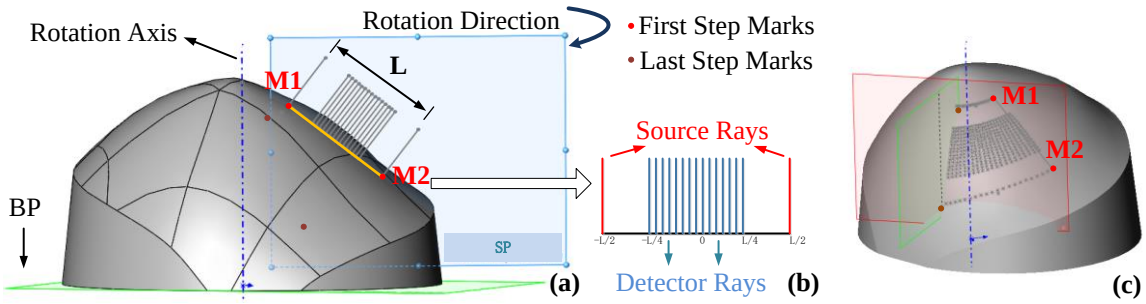

Figure 4.2: Alignment of sources and detectors on the surface of solid breast model. **(a)** A scanning plane (SP) perpendicular to the breast surface and crossing the optical rays of sources and detectors was first aligned passing through the first pair of source marks (M1 and M2). **(b)** Each source or detector path was simplified as a single optical ray perpendicular to the straight line across the source marks (M1 to M2). The sources and detectors along the optical rays were then projected onto the surface of solid breast model. The SP was then rotated around the rotation axis step-by-step with a 3-degree increment per step for projecting sources and detectors at all scanning steps. (c) The alignment of all scanned source and detector coordinates.

In order to assess the ability of ncDCT for imaging a tumor inside breast, I conducted a computer simulation on a female plastic mannequin breast. The surface geometry of the mannequin breast with source marks of ncDCT were scanned by a commercial 3-D camera, which was further converted to a solid breast tissue volume using SolidWorks (**Figure 4.1**). The scanned source and detector coordinates were then aligned on the surface of the solid breast model based on two pairs (at first and last scanning steps) of source marks (**Figure 4.2**). The probe scanning procedure was simulated by SolidWorks. Similar to the slab meshing, the solid breast volume was segmented into finite elements with node distances of 3 and 6 mm in the ROI and surrounding region. A solid volume mesh [largest dimension (mm): 100 (H) × 78 (W) × 70 (D)] with total nodes of 14717 was generated for simulations. A spherical tumor with a diameter of 10 mm and a node distance of 3 mm was then placed at the ROI center and the tumor centroid location was 7 mm beneath the breast surface (**Figure 4.3e**). For comparisons, we assigned the same

optical properties and BFI contrast as those used in slab-tissue simulation. The boundary data were also collected in the same manner over the ROI on the breast surface. Identical breast-shaped mesh with a pixel basis of $20 \times 20 \times 30$ and $\tau_1 = 8.7 \times 10^{-6}$ were used for image reconstruction.

4.2.2 Quantification of Tumor Location and Flow Contrast in the Breast-shaped Tissue Volume

This simulation used the same tumor model in the breast-shaped mesh with the same configuration and optical properties as assigned in **Chapter 4.2.1** (see **Figure 4.3e**). The tumor was placed beneath the surface of the breast-shaped mesh with varied central depths from 7 mm to 15 mm at 1 mm increment per step. It is noted that breast tumors with their centroid locations within the sensitive region of diffuse light (i.e., the detected penetration depth of NIR light is ~1/2 of the S-D separation (65, 67, 101)) were our most interested study population, since more reliable reconstructions can be generated. At each depth, the tumor-to-normal flow contrast was increased from 0-fold to 20-fold at 5-fold increment per step. The reconstructed tumor depth was characterized as the shortest distance from the reconstructed anomaly center to the breast mesh surface. The measurement accuracy of ncDCT system was assessed by quantifying the discrepancies between the reconstructed and assigned values in tumor central location and flow contrast.

To evaluate the noise influence on image reconstruction, I added noise on the subsets of boundary data collected from the tumor with 10-fold flow contrast throughout all varied depths. Forty $g_2(\boldsymbol{r}, \tau)$ curves with noises were generated and averaged at each effective S-D pair for DCT image reconstruction.

4.2.3 Reconstruction with A Priori Knowledge of Tumor Location and Volume

To improve the reconstruction accuracy of anomaly blood flow contrast, the soft-constraint method (94, 102-104) in NIRFAST package was tested in this simulation. A priori structural information of tumor (i.e., central location and tumor volume) was included in the inverse mesh by labeling the nodes in the inverse mesh according to the regions of tumor or surrounding tissues. A regularization matrix L was applied to the penalty term in the minimization function for DCT inverse problem, which was equivalent to applying a Laplacian-type filter to minimize variation within each region. Simulations were done with the spherical anomaly (10-fold flow contrast and diameter = 10 mm) placed at either 7 mm or 15 mm central depth beneath the breast surface and with or without noise.

4.2.4 Evaluation of Image Reconstruction Accuracy with Different τ Values

Previous DCT studies emphasized assigning a selective delay time τ to each S-D pair based on the analytical expression for $g_1(\boldsymbol{r},\tau)$ (**Equation 2.6**) which relies on simple geometry and homogeneous optical properties (60)(59). By contrast, we proposed to use a uniform τ for flow contrast imaging (37). From the view of $\mu_a^d(\tau,\boldsymbol{r}) = 2\mu_s'(\boldsymbol{r})k_0^2\alpha D_B(\boldsymbol{r})\tau$, assigning uniform τ unifies the $\mu_a^d(\tau,\boldsymbol{r})$ on the same time scale such that τ does not generate extra $\mu_a^d(\tau,\boldsymbol{r})$ contrast. However, since the accuracy of the numerical model and computation of Jacobian matrix in NIRFAST software rely on optical properties (105) (here indicates $\mu_a^d(\tau,\boldsymbol{r})$), τ selection could influence ncDCT image reconstruction. To evaluate the τ selection influence, twenty τ values ($1.0 \times 10^{-7} \leq \tau \leq 6.4 \times 10^{-5}$) from the entire range (generally from 1.0×10^{-7} to 1.0×10^{-3}

s) were used to reconstruct DCT images. With each selected τ value, anomaly (tumor) was assigned 5-, 10- and 15-fold flow contrasts and the central depth was set at 7 and 10 mm beneath the breast-shaped mesh surface. The reconstruction accuracies in tumor location and flow contrass were compared.

4.3 Results

4.3.1 ncDCT Recovered an Anomaly inside both Slab-shaped and Breast-shaped Tissue Volumes with Similar Accuracies

Figure 4.3 illustrates 3-D (**Figures 4.3a, 4.3b, 4.3e and 4.3f**) and 2-D cross-section (**Figures 4.3c, 4.3d, 4.3g and 4.3h**) views of blood flow distributions in the slab-shaped (top panel) and breast-shaped (bottom panel) tissue volumes, respectively. **Figures 4.3a, 4.3e, 4.3c** and **4.3g** show the originally assigned/simulated anomaly inside tissue volumes and **Figures 4.3b, 4.3f, 4.3d** and **4.3h** show the reconstructed results for comparisons. To clearly visualize the anomaly inside the tissue volume, 3-D background meshes were presented with 30% transparency of their original colors. The reconstructed anomalies were presented with FWHM thresholds in 3-D images (**Figures 4.3b** and **4.3f**) and without thresholds in 2-D cross-section views (**Figures 4.3d** and **4.3h**). **Table 4.1** summarizes the discrepancies between the assigned and reconstructed anomalies inside the slap-shaped and breast-shaped tissue volumes. These results indicate that the ncDCT system can recover the anomaly inside both slap-shaped and breast-shaped tissue volumes with similar accuracies.

Table 4.1: Computer simulation results in recovering an anomaly* inside slab-shaped and breast-shaped volume meshes.

	Anomaly central depth (mm) / % error	Anomaly diameter (mm) / % error	Peak flow contrast (fold) / % error	Average flow contrast (fold) / % error
Slab-shaped	6.4 / 8.6%	7.2 / 28%	12.8 / 28%	9.3 / 7%
Breast-shaped	6.6 / 5.7%	7.5 / 25%	12.2 / 23%	8.1 / 19%

*A spherical anomaly with a diameter of 10 mm and 10-fold flow contrast was placed at 7 mm beneath the surface of background tissue volumes.

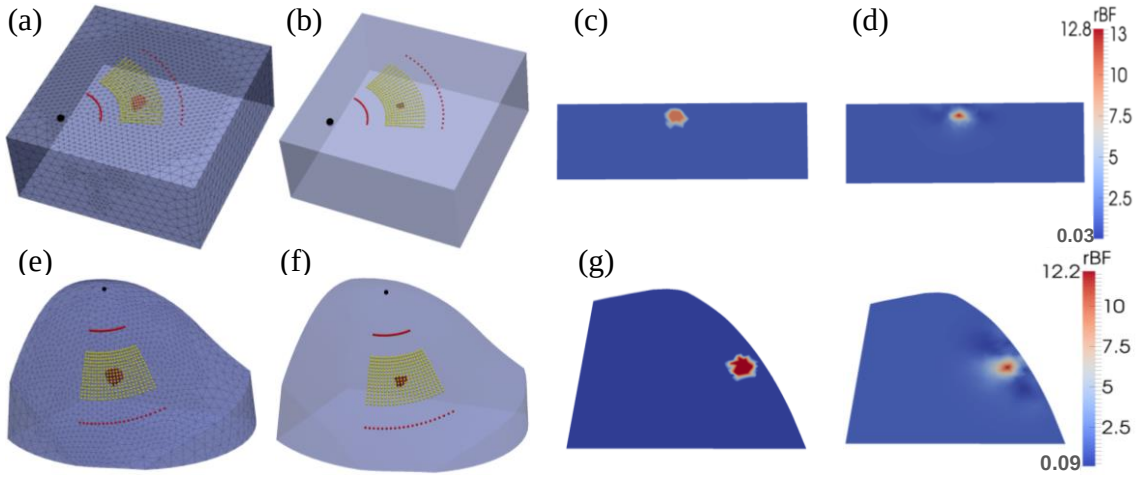

Figure 4.3: Recovery of anomaly blood flow contrasts inside the slab-shaped and breast-shaped volume meshes. A sphere anomaly with a diameter of 10 mm and 10-fold flow contrast was placed at 7 mm beneath the surface of background tissue volumes. (a) and (e) show the original assigned anomalies inside the volume meshes with sources and detectors aligned on the mesh surfaces; (b) and (f) show the reconstructed anomalies with FWHM thresholds; (c) and (g) show the 2-D cross-section views of original flow contrast distributions through the anomaly centers; (d) and (h) show the 2-D cross-section views of reconstructed flow contrast distributions.

4.3.2 Higher Reconstruction Accuracy Achieved when the Anomaly was within the Sensitive Region of Diffuse Light

The reconstruction results with varied anomaly locations and flow contrasts are presented in **Figure 4.4**. The discrepancies (**Figure 4.4b**) between the reconstructed and assigned central locations of the anomaly were smaller than the mesh node distance (3 mm) at all depths. The reconstructed anomaly locations were more accurate in the sensitive region of diffuse light (errors $\leq$ 0.5 mm at central depths $\leq$ 10 mm) compared to those in deeper depths.

Reconstruction errors in peak and average BFI contrast of the anomaly at varied center location and assigned flow contrasts are displayed in **Figure 4.4c**. The largest reconstruction errors in peak and average flow contrasts ranged from 31.4% to -77.0% and -23.6% to -82.9% respectively through all varied depths and flow contrasts. Similarly, the reconstructed peak and average BFI contrasts were more accurate in the sensitive region of diffuse light (peak and average BFI underestimations $\leq$ 27.8% and 45.3% respectively at central depths $\leq$ 10 mm) compared to those in larger depths.

Figures 4.4d and **4.4e** demonstrate the linear relationships between the assigned and reconstructed peak and average BFI contrasts. The relative anomaly flow contrast changes were well reconstructed from the chosen central depths of 7 mm (peak BFI: linear regression slope = 1.03, R^2 = 0.99, and $p < 0.001$; average BFI: linear regression slope = 1.02, R^2 = 0.99, and $p < 0.001$), 10 mm (peak BFI: linear regression slope = 1.01, R^2 = 0.97, and $p < 0.01$; average BFI: linear regression slope = 1.00, R^2 = 0.97, and $p < 0.01$), 13 mm (peak BFI: linear regression slope = 1.07, R^2 = 0.98, and $p < 0.01$; average BFI: linear regression slope =1.07, R^2 = 0.98, and $p < 0.01$), and 15 mm (peak BFI: linear

regression slope = 1.08, R^2 = 0.98, and $p < 0.01$; average BFI: linear regression slope = 1.08, R^2 = 0.98, and $p < 0.01$). The relationships between the assigned and reconstructed relative anomaly flow contrast changes from other tested depths were similar (results not shown here).

In total, these results indicate that relatively higher accuracies were achieved when the entire anomaly was within the sensitive depth of diffuse light. Also, even though the recovery of anomaly BFI contrasts was not as accurate as its location, the reconstructed anomaly BFI contrast changes were fairly accurate.

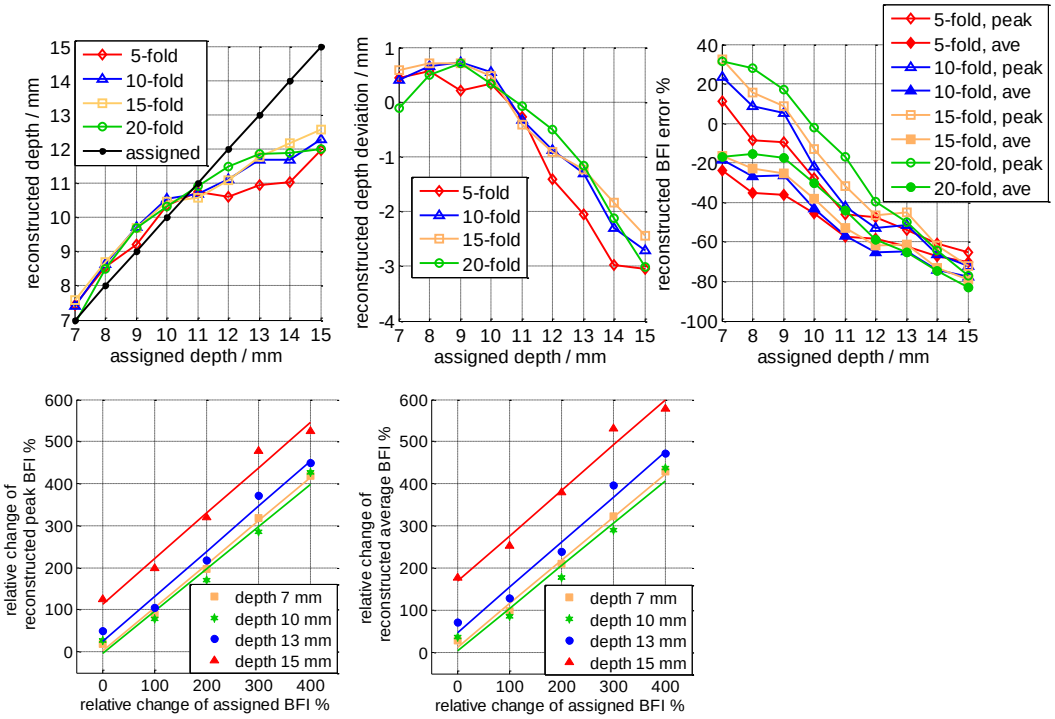

Figure 4.4: Evaluation of reconstruction accuracy of ncDCT in the breast-shape volume mesh. (a) and (b) show the center location and deviation of the reconstructed anomaly at different depths; (c) shows the percentage deviations of anomaly peak and average BFI contrasts at different depths; (d) and (e) show the linear relationships between the assigned and reconstructed peak & average BFI contrasts at different depths.

4.3.3 Noise Reduced Anomaly Recovery Accuracy

Figure 4.5 shows the ncDCT image reconstruction results with simulated noise added to the forward problem. For comparisons, images reconstructed from clean data (no noise) and noisy data are plotted together. When the anomaly volume was within the sensitive region of diffuse light (anomaly central depth ≤ 10 mm), the largest discrepancy between the reconstructed and assigned central locations of the anomaly was 1.2 mm (**Figure 4.5b**), 0.8 mm greater than that (0.4 mm) without noise. Similarly, the largest reconstruction errors in peak and average flow contrasts were 33.2% and 31.0% larger than those reconstructed without noise (**Figures 4.5c** and **4.5d**). Apparently, adding noise reduced reconstruction accuracies in recovery of the anomaly. However, the major conclusions drawn in **Chapter 4.3.2** are still valid.

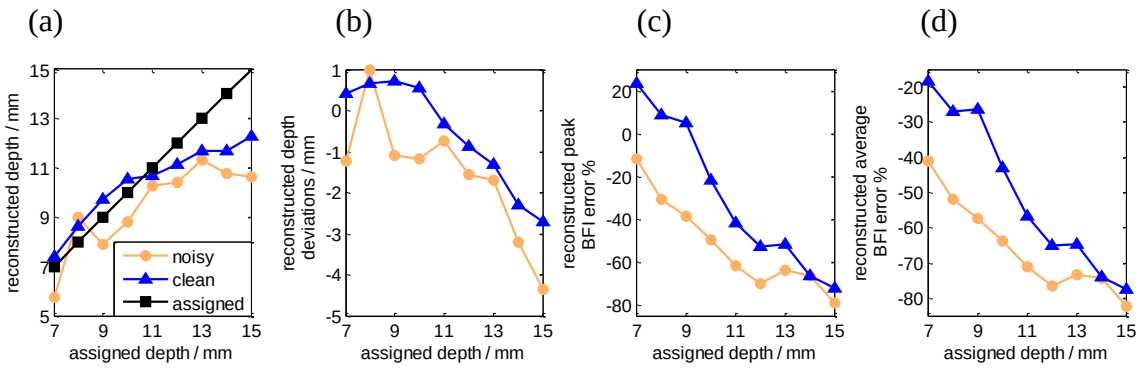

Figure 4.5: Noise influence on imaging accuracy of ncDCT. An anomaly was placed beneath the surface of the breast-shaped mesh with varied central depths from 7 mm to 15 mm. (a) and (b) show the center location and deviation of the anomaly at different depths, reconstructed with or without noise. (c) and (d) show percentage deviations of anomaly peak and average BFI contrasts at different depths, reconstructed with or without noise.

4.3.4 A Priori Knowledge of Anomaly Location and Volume Improved Flow Contrast Reconstruction

Figure 4.6 demonstrates the improvements in the reconstruction of BFI contrasts using a priori knowledge of tumor location and volume in DCT image reconstruction. The top (**Figures 4.6a** to **4.6e**) and bottom (**Figures 4.6f** to **4.6j**) panels show the reconstructed results when the anomaly is at the central depth of 7 and 15 mm beneath the surface, respectively. In each panel, image results without/with a priori information and without/with noise are plotted respectively. The transect plots (**Figures 4.6e** and **4.6j**) show the BFI distributions across the anomaly. The reconstruction accuracies in BFI contrasts were significantly improved when a priori knowledge of anomaly structural information was applied on data with and without noise. The peak/average BFI contrast errors were only 0.1%/4% (without noise) and 12.3%/12.3% (with noise) respectively when using a priori structural information for the anomaly located in the sensitivity region of diffuse light (i.e., at the central location of 7 mm, **Figure 4.6e**). The BFI contrast improvement at the deeper central depth of 15 mm was also remarkable (**Figure 4.6j**).

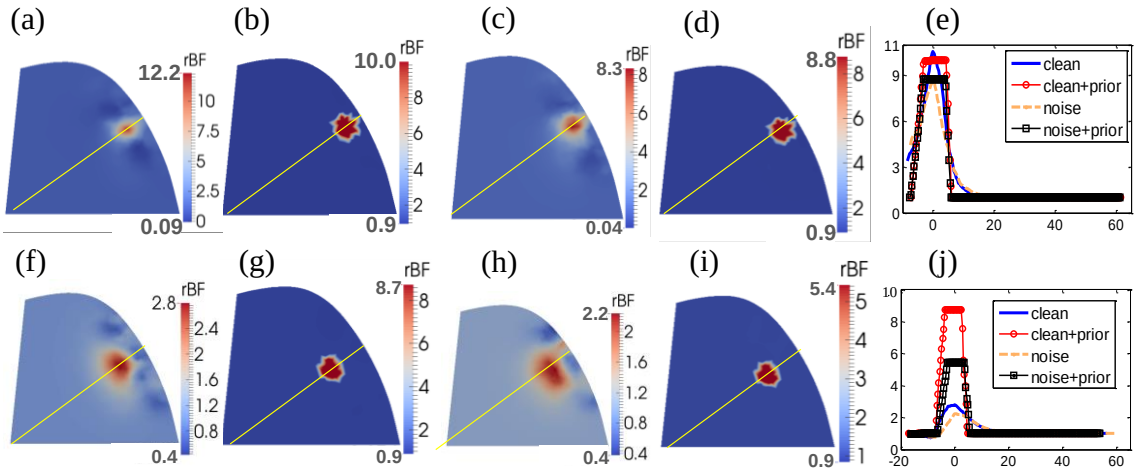

Figure 4.6: Comparison of anomaly reconstructions without and with a priori structural information. The top (a to e) and bottom (f to j) panels show the reconstructed flow contrast distributions of an anomaly (assigned a 10-fold flow contrast) located at 7 and 15 mm central depths, respectively. (a) and (f) show reconstructed results without the a priori structural knowledge of the anomaly; (b) and (g) show the reconstructed results with the a priori structural knowledge; (c) and (h) show the reconstructed results without the a priori structural knowledge and with noise. (d) and (i) show the reconstructed results with the a priori knowledge information and with noise. The flow contrast profiles crossing the yellow lines are shown in (e) and (j).

4.3.5 Optimization of τ Improved Imaging Accuracy

Figure 4.7 shows the errors in the reconstructed anomaly locations and BFI contrasts with different τ selections. The discrepancies (**Figure 4.7a**) between the reconstructed and assigned central locations of the anomaly were smaller than the mesh node distance (3 mm) at all tested anomaly central depths and contrasts. The reconstructed anomaly locations were more accurate when τ was chosen in the range of 5.1×10^{-6} sec to 1.91×10^{-5}sec (between the two vertical lines in **Figure 4.7a**). Reconstruction errors in average BFI contrast with varied τ selections are displayed in **Figure 4.7b**. By choosing proper τ value, the error in reconstructed average flow contrast inside the anomaly can be reduced up to 27.6% (i.e., anomaly with 15-fold flow contrast located at 7 mm depth).

While smaller τ provided more accurate flow contrast reconstruction for anomaly located shallower, larger τ was more preferable for anomaly located deeper from mesh surface. In general, τ selected from certain range ($5.1 \times 10^{-6} \leq \tau \leq 1.91 \times 10^{-6}$ sec) between the two vertical lines shown in **Figure 4.7b** can provide more accurate results in flow contrast and location reconstructions.

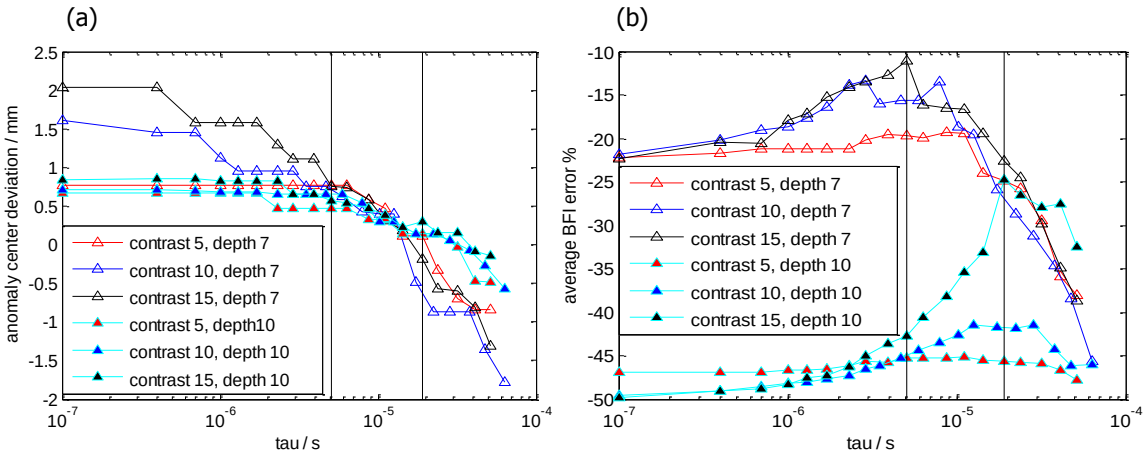

Figure 4.7: Evaluation of reconstruction accuracy of ncDCT with varied τ values based on meshes with 5-, 10- and 15-fold anomaly flow contrasts, and anomaly centroid located at 7 mm and 10 mm depths. (a) Shows deviation of the reconstructed anomaly center locations. Positive/negative values indicate deeper/shallower than original locations. (b) Shows reconstruction errors in average flow contrasts inside anomalies. Two pairs of black vertical lines in (a) and (b) are plotted at the same τ values, respectively, indicating the recommended τ intervals for image reconstruction.

4.4 Discussion and Conclusions

In this chapter, computer simulations were used to investigate the origins of flow reconstruction discrepancies. From the simulations, we observed similar reconstruction accuracies in blood flow contrasts and tumor central locations with slab-shaped and breast-shaped boundaries (see **Figure 4.3** and **Table 4.1**), indicating the ability of ncDCT for reconstructing tumor flow contrast in human breast with irregular geometry. Further

simulations on breast-shaped geometry evaluated reconstruction accuracies when tumors had different flow contrasts and located at different depths. The results suggested that the reconstructed tumor location and flow contrasts were more accurate when the tumor volume was within the sensitive region of diffuse light (see **Figure 4.4**). Based on photon diffuse theory, the penetration depth of diffuse light is ~1/2 of the S-D separation (65, 67, 101). The largest S-D separation of ncDCT was 30 mm, allowing for a penetration depth up to ~15 mm. As such, it was not surprising that the reconstruction errors increased as the tumor center located at a depth deeper than 10 mm.

In contrast to the recovery of tumor location, the reconstruction of tumor blood flow contrasts was more complicated. The reconstructed peak BFIs were overestimated when the tumor located closer to the breast surface and underestimated when the tumor located out of the sensitive region of diffuse light (see **Figure 4.4c**). By contrast, the reconstructed average BFIs were consistently underestimated. These observations are similar to those in DOT for reconstruction of tumor absorption contrasts (106, 107). It is known from the DOT practice that imaging sensitivity is higher at the shallow region beneath tissue surface (108). Therefore, the reconstructed peak BFI from a single node close to the tissue surface tends to be overestimated. However, most of the reconstructed BFIs from the tumor node are prone to be underestimated due to the nature of inverse problem (109). Since the number of boundary data (S-D pairs) in ncDCT is much smaller than the unknowns to be solved (i.e., BFIs at all mesh nodes), the inverse problem is unstable (110), leading to the underestimation (106). In addition, according to the definition of $\mu_a^{total}(\boldsymbol{r},\tau) = \mu_a(\boldsymbol{r}) + \mu_a^d(\boldsymbol{r},\tau)$, BFI reconstruction errors come from both "static" and "dynamic" absorption coefficients. Therefore, dynamic flow contrast errors

may be further enlarged by attributing all reconstruction errors of $\mu_a^{total}(\boldsymbol{r},\tau)$ to dynamic $\mu_a^d(\boldsymbol{r},\tau)$ while ignoring static errors of $\mu_a(\boldsymbol{r})$.

Similar to our previous findings (37), the relative changes of tumor flow contrasts can be accurately reconstructed in a large range of flow contrast variations (see **Figures 4.4d** and **4.4e**). The observed linear relationships with a slope of close to "1" indicate the ability of ncDCT to capture tumor blood flow changes, which can be potentially used to longitudinally monitor tumor hemodynamic responses to interventions.

As expected, adding noise reduced the reconstruction accuracies (see **Figure 4.5**). However, tumors can still be reconstructed clearly from the boundary data with noise (see **Figure 4.5**), indicating the feasibility of ncDCT for in vivo breast tumor detection. More importantly, adding a priori knowledge of the tumor volume and location improved significantly reconstruction accuracy (see **Figure 4.6**), which agrees with previous observations in DOT (94, 102, 104).

Our previous publication has briefly discussed the selection of τ for image reconstruction (37). Five different τ values ($4 \times 10^{-7} \leq \tau \leq 1.9 \times 10^{-5}$ s) were selected for computer simulations, and the results showed little impact on the reconstructed flow contrast. Further investigation with a broad range of experimental configurations was conducted in this study. Simulations with extensive τ selections ($1.0 \times 10^{-7} \leq \tau \leq 6.4 \times 10^{-5}$) have been performed to evaluate the influence on flow contrast and location reconstruction when the tumor was within the sensitive region of diffuse light. Different τ selections have smaller influence in the tumor location recovery compared with the flow contrast recovery. However, within the same range of τ selection ($5.1 \times 10^{-6} \leq \tau \leq 1.91 \times 10^{-5}$) the reconstruction accuracies in both flow contrast and tumor central

location reconstructions are higher than with the other τ values. So we propose to select the range $5.1 \times 10^{-6} \leq \tau \leq 1.91 \times 10^{-5}$ for future ncDCT image reconstruction.

In conclusion, computer simulations based on different boundary geometries were performed to demonstrate the imaging capability of the novel ncDCT system on breast tumor detection. Results suggested that relatively high ncDCT image reconstruction accuracy can be achieved when the entire tumor was within the sensitive region of diffuse light. Image reconstruction with a priori knowledge of the tumor volume and location can significantly improve the accuracy in tumor blood flow contrast reconstruction. The optimized range of τ selection ($5.1 \times 10^{-6} \leq \tau \leq 1.91 \times 10^{-5}$) was provided to reconstruct ncDCT images with higher accuracies. Based on the computer simulation results, future development in instrumentation should increase the effective measurement pairs to reduce the underestimation nature of the inverse problem. Measurements from deep tissue are especially helpful to improve the image reconstruction accuracy. Depth correction algorithms should be integrated for ncDCT image reconstruction (i.e., increase the weights to information obtained from elements located deep inside mesh) such that tumor location recovery is more accurate even though the tumor was outside the sensitive region of diffusive light.

CHAPTER 5 NCDCT OF HUMAN BREAST TUMORS

5.1 Introduction

The autonomic growth and spread of malignant tumors are dependent on increased angiogenesis arising from the increased metabolic demand (111). Since functional alternations in tumors often appear earlier than detectable morphological changes, functional imaging of tumor hemodynamics and metabolism is a new strategy for early cancer diagnosis (112). Previous studies using different imaging modalities have found significant tumor-to-normal blood flow contrast in carcinomas, e.g., up to 12-fold contrast was found in post-menopausal women by PET (14, 113) and 3-fold contrast in flow velocity was also found by Doppler Ultrasound (114). Near-infrared (NIR) diffuse optical technologies provide a noninvasive and relatively inexpensive tool for functional imaging of tumor hemodynamics in deep microvasculature up to several centimeters (53-55, 115). The most commonly used NIR diffuse optical spectroscopy/tomography (DOS/DOT) can quantify total hemoglobin concentration (THC) and blood oxygen saturation (StO_2) in tumors (116, 117). DOS/DOT has been used over several decades to detect oxygenation alternations in breast tumors (32-36). For example, THC was found up to 2-fold higher in malignant lesions than nearby healthy tissues (117). More recently, a novel NIR diffuse correlation spectroscopy (DCS) technique has also been developed for direct measurement of blood flow index (BFI) in deep tissues (37). A few pilot studies of breast tumors using DCS have found increased blood flow inside the tumor in contrast to surrounding normal tissues (i.e., 2- to 10-fold flow contrasts) (53, 55). Real-time

monitoring of breast tumor blood flow response to neoadjuvant chemotherapy also demonstrated the potential of DCS for assessing cancer therapies (53, 56, 57).

Our group has recently developed a novel noncontact DCT (ncDCT) system enabling 3-D imaging of deep tissue blood flow distribution without contacting the tissue (37, 89, 92). The imaging theory (**Chapter 2**), instrumentation of ncDCT system (**Chapter 3**) and validation work including computer simulations and phantom experiments were described (**Chapters 3 and 4**) in previous chapters. In this chapter, I report the first 3-D blood flow contrast imaging of human breast tumors using the noninvasive, noncontact diffuse correlation tomographic technique.

5.2 Methods

5.2.1 Subjects

Twenty-eight female patients with breast tumors were recruited from University of Kentucky Comprehensive Breast Care Center with signed informed consent approved by the University of Kentucky Institution Review Board. According to our ncDCT system design and measurement protocol, patients with lesions located no deeper than 2 cm (central to breast surface, measured by ultrasound imaging) and from 9 o'clock to 3 o'clock on the breast were recruited. There were no wound on patients' breasts and all the patients had their scheduled biopsy procedures following the optical measurements. The biopsy results showed 7 patients had malignant tumors and 21 patients had benign lesions. The average age of the patients was 47.6 $\pm$ 16.3 years (see **Table 5.1**).

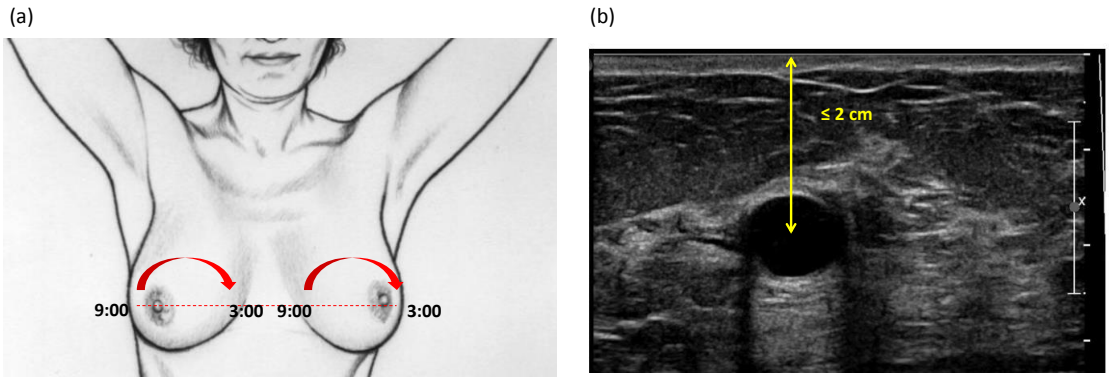

Figure 5.1: Schematic diagram (**a)** and ultrasound image **(b)** of breast lesion locations (118).

5.2.2 Experimental Protocol

The patient was asked to lie in a supine position or on her side (with pillow support) according to the lesion location. The tumor lesion inside breast was determined by radiologists using ultrasound imaging prior to the optical measurement and marks were made on breast surface with mark pens. The tumor mass margin along the radio direction was also marked on the ultrasound images, which was used to compare with our reconstructed flow contrast images.

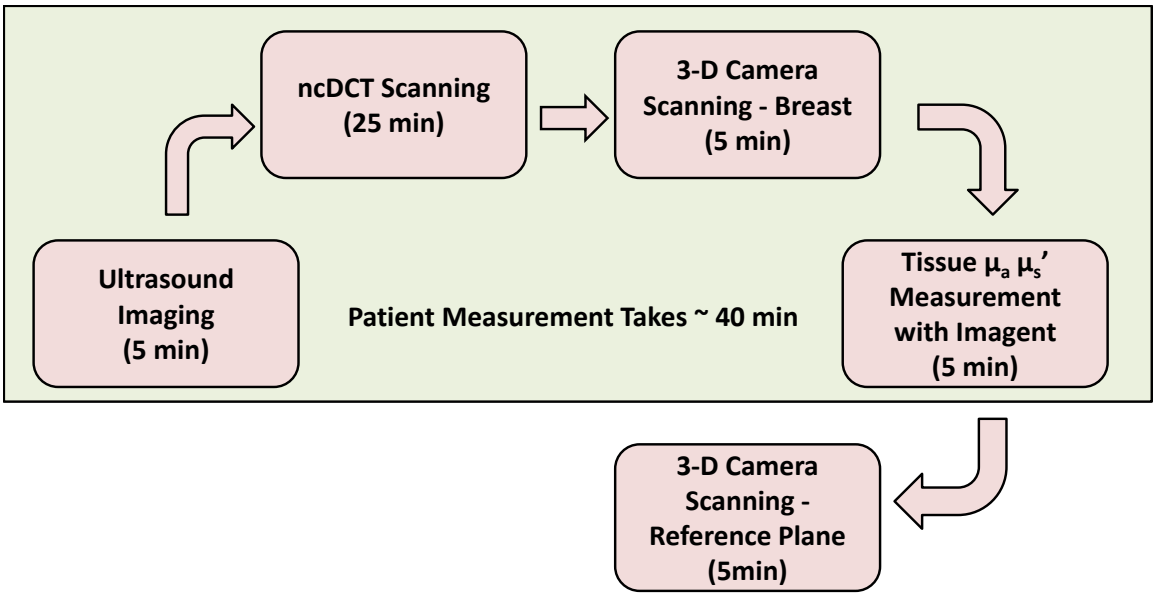

Figure 5.2: Flow chart of experimental protocols.

The ncDCT probe was then aligned perpendicularly on top of the marked lesion region, with two sources evenly distributed on two sides of the lesion along the radio direction. Light intensities injected to breast tissue were adjusted to meet American National Standards Institute standards for laser safety usage (119). The ncDCT probe was then driven by a step motor to scan rotationally around the breast nipple over the region of breast tumor. The scanning procedures were similar to those described previously (**Chapter 4.1.1**). Briefly, multiple rotational scanning steps were taken to cover the tumor bearing region in the breast, with a 3-degree increment per step. For each patient, the number of scanning steps may vary depending on the tumor size and lesion location relative to the breast surface. Forty $g_2(\boldsymbol{r},\tau)$ curves were collected from each source-detector (S-D) pair for each patient. Two source pairs at the beginning and ending steps of scanning procedure and the rotation center were visually marked on the breast surface as references for the alignment of sources and detectors on the surface mesh. The surface

geometry of the breast with the source and rotation center marks was then recorded by a commercial 3-D camera for image reconstruction. Following the ncDCT measurement, the Imagent was used to measure μ_s' and μ_a of the breast tissue at three different locations (**Chapter 3.3.3**) (71). The averaged μ_s' and μ_a over the multiple sites were used as initial inputs for flow image reconstruction. After the patient leaves the measurement bed, another photo of the ncDCT probe and the reference plane was taken for the alignment of the scanned source and detector coordinates onto the breast-shaped mesh. The total measurement time on patient is around 40 minutes (**Figure 5.2**).

5.2.3 Image Reconstruction

The solid breast mesh of the patient was created in the same way as that of plastic mannequin breast (**Chapter 4.1.1**). The node distance was 3 mm in the ROI and 6 mm in the surrounding region. Boundary BFIs on the breast mesh surface were then extracted by fitting the measured $g_2(\boldsymbol{r}, \tau)$ curves from effective S-D pairs. These boundary BFI data were then calibrated to the BFIs collected at the first scanning step where the tissue underneath the probe was outside the tumor region and thus assumed to be homogeneous and healthy. The calibrated boundary data were finally used for DCT image reconstruction.

Noise Influence Evaluation. Apart from the noises mentioned in computer simulations originated from electronics and optics, there were other noises in the breast tissue measurements. Those additional noises include physiological noises such as respiration and heart beating, motion artifacts such as patients' body gesture changes and tumor heterogeneity caused noise during light propagation in tissues. In order to evaluate

the noise influence, the coefficients of variation (C_v) in extracted boundary BFIs from breast tissues and liquid phantoms were compared:

$$C_v = \frac{std\ (BFI)}{mean\ (BFI)} \tag{5.1}$$

For patient measurements, the C_v of boundary BFIs from each scanning step were calculated according to **Equation 5.1**. According to the protocol for breast tissue measurements, there were 40 optical measurements per step from each source-detector pair. For liquid phantom measurements, same measurement procedures were performed following the *in vivo* measurements, with same optical properties and detected light intensities.

The boundary BFI data from one patient with invasive ductal carcinoma (Patient No. 19) was analyzed as an example. This patient kept her body position well during the scanning of ncDCT. **Figure 5.3a** shows the mean values and standard deviations of the normalized boundary BFIs/flow indices obtained at one single S-D pair (2 cm S-D separation) in the breast tissue (over tumor region) and phantom solution. **Figure 5.3b** plots the Cv values at all steps according to **Figure 5.3a**. The averaged Cv values for the breast tissue and phantom measurements were 0.105 ± 0.017 and 0.089 ± 0.004, respectively. Significant differences were found between the two groups of Cv values ($p = 0.005$). Large variations observed from the patient were likely due to the physiological noises in *in vivo* measurements.

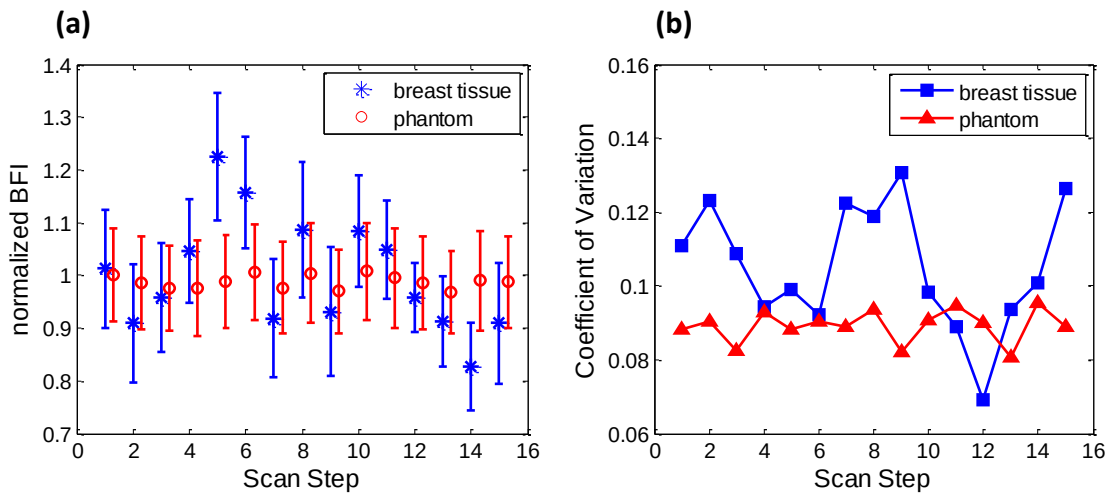

Figure 5.3: The effect of additional noises on in vivo breast tissue measurement from one patient analysis. (a) Normalized boundary BFI measured on breast and phantom solution by recording one source-detector measurement pair through 15 scanning steps. (b) The coefficients of variation derived from (a).

The Cv values from other patients' measurement data may vary due to the stability of patients' body positions during measurements. Therefore, the data with obvious motion artifacts (with large Cv values) were excluded from the image reconstruction.

5.3 Results

5.3.1 Representative Individual Results

Representative 3-D reconstructed images from two patients with malignant cancers and two subjects with benign lesions are shown in **Figures 5.4-5.7**.

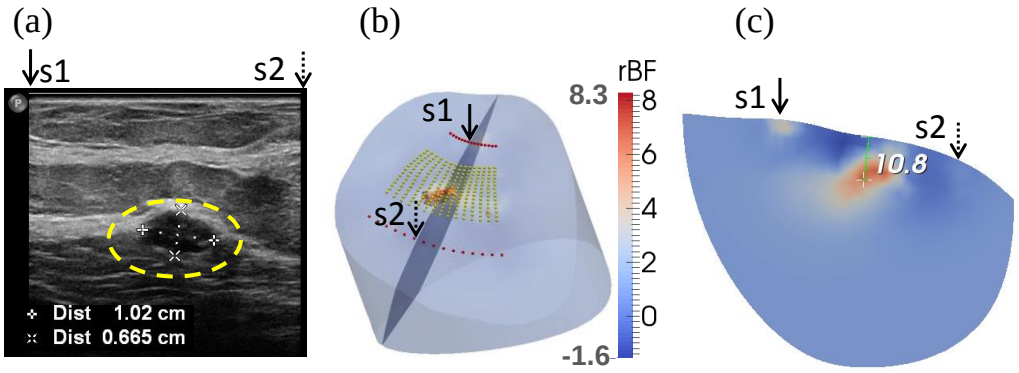

Figure 5.4: Clinical example of ncDCT imaging result from case 1. (a) Patient No. 16 ultrasound image taken from radio direction shows a 10.2 × 6.65 mm^2 oval mass (inside the yellow dashed circle) with circumscribed margins parallel to the skin. The mass center is located at 19.2 mm beneath the skin surface. A core biopsy revealed a ductal papilloma with low-grade ductal adenocarcinoma in situ. (b) Shows the reconstructed 3-D tumor blood flow contrasts with FWHM threshold (pink mass). The red and yellow dots indicate scanned source and detector locations. (c) Shows the cross-section view, which is displayed in (b), through the reconstructed tumor center. The reconstructed tumor center is 10.8 mm deep. S1 and S3 are one pair of projected source locations at one scanning step. (a) was taken with ultrasound transducer aligned from S1 to S2.

Case 1 (Patient No.16): Ductal Papilloma with Low-grade Ductal Adenocarcinoma in situ (malignant)

The first case (Patient No. 16) was a 59-year-old female who had ductal papilloma and low-grade adenocarcinoma in situ. According to the ultrasound imaging (**Figure 5.4a**), the lesion with the dimension of 10.2 × 6.65 mm^2 was located at 19.2 mm beneath the skin surface. The dimension of the reconstructed tumor by ncDCT with the full width half-maximum (FWHM) threshold was approximately 15.1 × 5.8 mm^2 (**Figure 5.4c**), which matched ultrasound image. However, the reconstructed tumor central location was 10.8 mm beneath the breast surface, which differed from the ultrasound image result (19.2 mm). The 2-D cross-section view shown in **Figure 5.4c** was cut along the radio direction of scanning and through the tumor center and breast nipple (see extracted cross-

section in **Figure 5.4b**). The peak and average tumor blood flow contrasts were 8.3-fold and 5.9-fold, respectively. Note that measurement noise caused some artifacts with $\mu_a^{total}(\boldsymbol{r},\tau)$ lower than static $\mu_a(r)$ in the region bordering the reconstructed tumor, leading to some negative flow values.

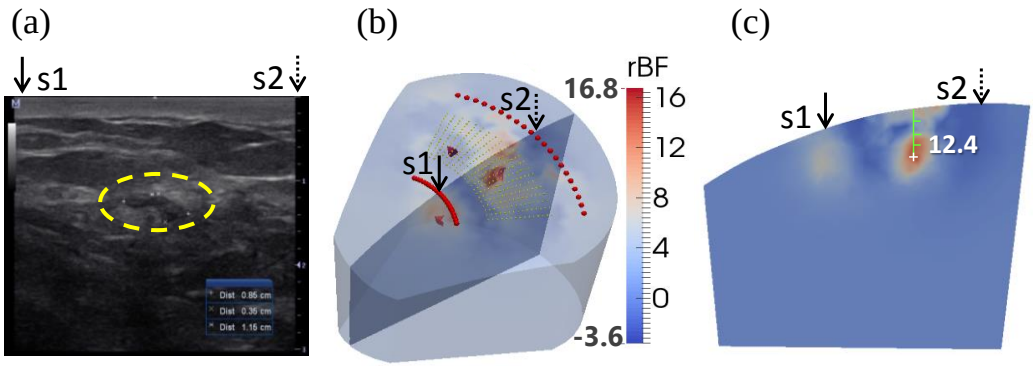

Figure 5.5: Clinical example of ncDCT imaging result from case 2. (a) Patient No. 26 ultrasound image taken from radio direction shows a 8.5 × 3.5 mm^2 mass (inside the yellow dashed circle), located at 13.3 mm beneath the skin surface. A core biopsy revealed atypical ductal hyperplasia and low-grade carcinoma in situ. (b) Shows the reconstructed 3-D tumor blood flow contrasts with FWHM threshold (big pink mass is the reconstructed tumor, the other two masses are artifacts). The red dots indicate scanned source locations. (c) Shows the cross-section view through the reconstructed tumor center. The reconstructed tumor center is 12.4 mm deep.

Case 2 (Patient No. 26): Atypical Ductal Hyperplasia and Low Grade Carcinoma in situ (maligant)

The second case (Patient No. 26) was a 49-year-old female who had an atypical ductal hyperplasia and low-grade carcinoma in situ. Ultrasound images (**Figure 5.5a**) show that the lesion centroid was located at 13.3 mm beneath the skin surface with the dimension of 8.5 × 3.5 mm^2. Our ncDCT imaging results show a clear large tumor lesion with two small suspicious artificial anomalies (**Figure 5.5b**). The dimension of the reconstructed large tumor was approximately 12.3 × 5.1 mm^2 (**Figure 5.5c**) and its

central depth was 12.4 mm beneath the breast surface, which fairly matched the ultrasound imaging result. The peak and average blood flow contrasts were 14.0-fold and 10.6-fold, respectively. Artifacts with negative flow values were also observed in the region bordering the reconstructed tumor.

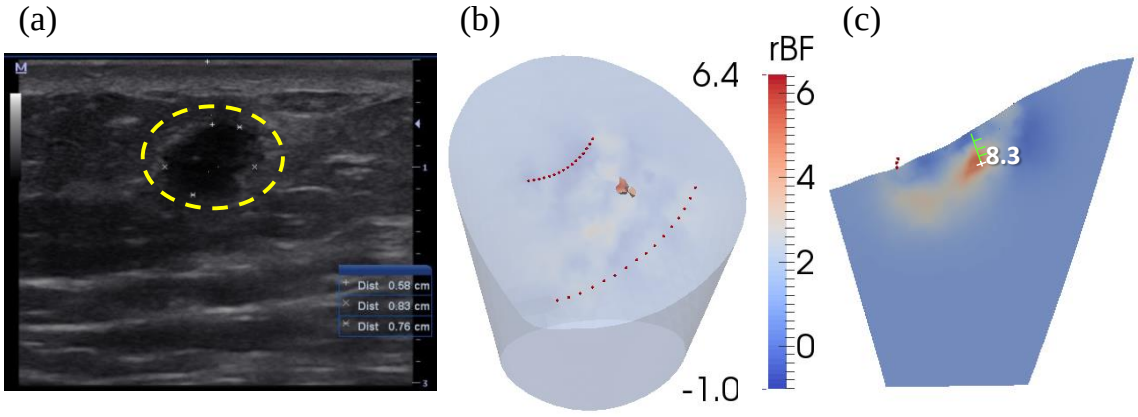

Figure 5.6: Clinical example of ncDCT imaging result from case 3. (a) Patient No. 22 ultrasound image taken from radio direction shows a 8.3 × 7.6 mm^2 mass (inside the yellow dashed circle), located at 10.0 mm beneath the skin surface. A core biopsy revealed a lymphocytic lymphoma. (b) Shows the reconstructed 3-D tumor blood flow contrasts with FWHM threshold (pink mass). The backgrounds are presented with 30% transparency of the original color clarity. (c) Shows the cross-section view through the reconstructed tumor center. The reconstructed tumor center is 8.3 mm deep.

Case 3 (Patient No. 22): Lymphocytic Lymphoma (benign)

The third case (Patient No. 22) was a 61-year-old female who had lymphocytic lymphoma. According to the ultrasound imaging (**Figure 5.6a**), the lesion with the dimension of 8.3 × 7.6 mm^2 was located at 10.0 mm beneath the skin surface. The dimension of the reconstructed tumor with FWHM threshold was approximately 4.5 × 10.5 mm^2 (**Figure 5.6b**) and its central depth was 8.3 mm beneath the breast surface

(**Figure 5.6c**), which matched ultrasound imaging result. The peak and average tumor blood flow contrasts were 6.5- and 4.9-fold, respectively.

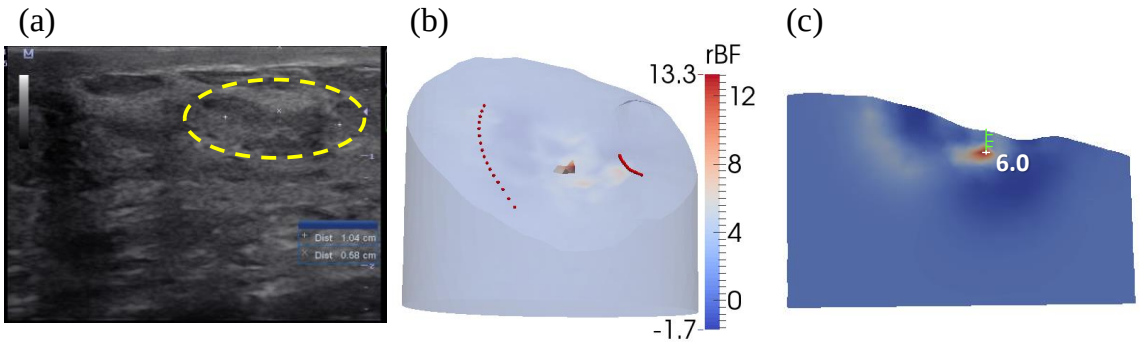

Figure 5.7: Clinical example of ncDCT imaging result from case 4. (a) Patient No. 20 ultrasound image taken from radio direction shows a 10.4 × 2 mm^2 mass (inside the yellow dashed circle), located at 5.8 mm beneath the skin surface. A core biopsy revealed a fibroadenoma, no atypical features identified. (b) Shows the reconstructed 3-D tumor blood flow contrasts with FWHM threshold (pink mass). (c) Shows the cross-section view through the reconstructed tumor center. The reconstructed tumor center is 6.0 mm deep.

Case 4 (Patient No. 20): Fibroadenoma (benign)

The fourth case (Patient No. 20) was a 24-year-old female who had fibroadenoma without atypical features. According to the ultrasound imaging (**Figure 5.7a**), the lesion with the dimension of 10.4 × 2.0 mm^2 was located at 5.8 mm beneath the skin surface. The dimension of the reconstructed tumor was approximately 7.1 × 2.6 mm^2 (**Figure 5.7b**) and its central depth was 6.0 mm beneath the breast surface (**Figure 5.6c**), which matched ultrasound image. The peak and average tumor blood flow contrasts were 13.3-fold and 8.6-fold, respectively. Artifacts with negative flow values were observed in the region bordering the reconstructed tumor.

5.3.2 Group Results

Table 5.1 summarized group imaging results from *in vivo* breast tumor measurements. Higher tumor-to-normal blood flow contrasts were observed in the majority of patients measured by our ncDCT system (18 out of 28). The peak/average tumor-to-normal blood flow contrasts, the reconstructed tumor location and dimension were quantified, using the same methods described in **Chapter 4**.

Reconstructed tumor depths and dimensions matched ultrasound images well when the tumors were within the sensitive region of diffuse light (depth of ~ 1.5 cm). For the benign group with observed blood flow contrasts (n = 14), the averaged blood flow contrasts in the reconstructed tumor regions were 18.0 ± 7.0 (peak flow) and 12.6 ± 4.7 (mean flow) folds, while the corresponding blood flow contrasts in the malignant group (n = 4) were 16.0 ± 6.1 (peak flow) and 10.6 ± 3.3 folds (mean flow). No significant difference was found in blood flow contrasts between the two groups.

Tumor-to-normal blood flow contrasts were not observed in some patients' reconstruction results. Among those cases, three patients' data was contaminated by motion artifacts, one patients' lesion region was not able to be covered completely by ncDCT probe (patient No. 5, lesion was 55 mm long located beneath the nipple), and three patients' data collection procedures were normal. The lesion types for three patients with smooth measurements were non-proliferative fibrocystic changes (patient No. 3, 8.7 mm dimension, 12.7 mm central to surface depth), duct ectasia (patient No. 6, 3.5 mm dimension, 11.6 mm depth) and breast tissue with no significant pathologic abnormality (patient No. 28, 9.9 mm × 2.4 mm dimension, 8.1 mm depth). In addition, three patients' reconstruction results were excluded from image reconstruction since the measurement

procedures were incorrect (n = 2) and the measurement was stopped due to the instrument malfunction (n = 1).

Table 5.1: Group imaging results from *in vivo* breast tumor measurements.

No.	Race	Age	Tumor biopsy results		ncDCT imaging			US imaging depth / mm
			Type	Description	Peak flow / fold	Mean flow / fold	Depth / mm	
1	W	44	B	fibroadenoma	Excluded (reason A)			NA
2	W	46	B	intraductal papilloma	Excluded (Reason A)			20.3
3	W	36	B	non-proliferative fibrocystic changes	No contrast observed (Reason C)			12.7
4	W	60	B	complex fibroadenoma	Excluded (Reason B)			12.0
6	W	57	B	duct ectasia	No contrast observed (Reason C)			11.6
9	W	22	B	fibroadenoma with usual ductal hyperplasia	20.2	14.3	9.7	12.8
10	B	30	B	fibroadenoma	19.1	13.2	9.1	14.1
11	B	71	B	intraductal papilloma	11.8	8.5	9.2	11.5
12	B	27	B	fibroadenoma	17.6	13.6	13.0	10.3
13	W	55	B	fat necrosis	18.3	13.6	6.2	5.5
15	W	29	B	cellular fibroadenoma	15.7	10.3	10.2	9.5
17	W	63	B	intraductal papillomas with atypical ductal hyperplasia	25.1	17.2	11.2	27.0
18	B	41	B	nodular adenosis with associated microcalcification	18.9	12.6	13.8	15.0
20	B	24	B	fibroadenoma	13.3	8.6	6.0	5.8
21	W	47	B	proliferative fibrocystic features	17.3	12.1	12.3	19.0
22	W	61	B	lymphocytic lymphoma	6.5	4.9	8.3	10.0
23	W	62	B	stromal fibrosis	No contrast observed (reason B)			22.2
24	H	20	B	fibroadenoma with myxoid stroma	26.7	17.9	5.9	12.2
25	W	44	B	cellular fibroadenoma, cannot exclude benign phyllodes	8.2	6.6	10.6	14.8
27	W	40	B	proliferative fibrocystic change with prominent cyst formation and extensive papillary apocrine metaplasia	32.8	22.4	9.7	11.5

Table 5.1 (continued)

28	B	64	B	breast tissue with no significant pathologic abnormality	No contrast observed (Reason C)			8.1
Benign tumor summary		Total number of reconstructed tumors / measured: 14 / 21 Peak flow contrast: 18.0 ± 7.1fold Mean flow contrast: 12.6 ± 4.7 fold						
5	H	32	M	infiltrating moderately to poorly differentiated ductal adenocarcinoma	No contrast observed (Reason A)			20.0
7	W	71	M	invasive moderately differentiated ductal carcinoma	No contrast observed (Reason B)			10.0
8	W	63	M	intracystic/encysted papillary carcinoma in situ	No contrast observed (Reason B)			10.0
14	W	73	M	invasive poorly differentiated ductal adenocarcinoma	21.5	12.4	7.6	19.4
16	B	59	M	ductal papilloma with low-grade ductal adenocarcinoma in situ	8.3	5.9	10.8	19.2
19	W	54	M	invasive ductual carcinoma	20.1	13.4	15.9	20.0
26	W	49	M	atypical ductal hyperplasia and low grade carcinoma in situ	14.0	10.6	12.4	13.3
Malignant tumor summary		Total number of reconstructed tumors / measured: 4 / 7 Peak flow contrast: 16.0 ± 6.1fold Mean flow contrast: 10.6 ± 3.3 fold						

W: White; H: Hispanic; B: Black

M: Malignant; B: Benign

US: Ultrasound

Reasons for no tumor flow contrasts : A – lesion region could not be covered completely by ncDCT probe; B – data was contaminated by motion artifacts (i.e., body gesture changed and coughed); C – data collection was normal, however, no flow contrast was observed.

Excluded reasons: A – measurement procedure was invalid (i.e., source and detector scanning coordinates couldn't be correctly aligned on the mesh); B – measurement was stopped due to the instrument malfunction.

5.4 Discussion and Conclusions

Since increased angiogenesis in breast tumor is commonly associated with blood flow increase, imaging of blood flow distribution in breast tissue is of great importance for tumor detection (111). Previous phantom experiment and computer simulations (**Chapters 3** and **4**) have demonstrated the feasibility of applying ncDCT system for breast tumor flow contrast imaging. The remaining challenge lies in handling potential problems arising from the *in vivo* measurements.

In this chapter, preliminary study of human breast tumor imaging with ncDCT system was performed. Higher blood flow contrasts in the tumor regions compared to the surrounding tissues were observed in most of measured breast tumors. In reconstructed ncDCT images with higher blood flow contrasts, the tumor positions on the x-y plane agreed well with ultrasound imaging results (see examples in **Figures 5.4b-5.7b**). The reconstructed tumor central depth matched the ultrasound image when tumors were located within the sensitive depth of diffuse light (see examples in **Figures 5.5c-5.7c**). For some patients, the reconstructed tumor central depths were shallower than ultrasound imaging result (see example in **Figures 5.4c**). These were likely due to the fact that tumors were deeper than the depth where diffuse light cannot reach with our current ncDCT system.

It has been demonstrated by computer simulations (**Chapter 4.2.4**) that a prior knowledge of tumor location and volume can improve image reconstruction accuracy. However, due to the difficulty of co-registering the 2-D ultrasound image and 3-D ncDCT image, it was not possible in this study to apply the a priori structural knowledge of tumor for improving the accuracy of image reconstruction in patients. Future study

may utilize 3-D anatomical imaging modalities such as MRI or CT to obtain accurate priori structural information of the tumor.

The averaged mean values of tumor-to-normal blood flow contrasts for two groups of breast tumors were 10.6 ± 3.3 -fold (malignant) and 12.6 ± 4.7 -fold (benign). The results were comparable to previously reported flow contrasts of 2- to 10-fold in breast tumors detected by DCS (53, 55). It should be noted that the tumor flow contrasts quantified previously by DCS may be underestimated due to the partial volume effect by the healthy tissues surrounding the tumor. In addition, the potential crosstalk between μ_a, μ_s' and BFI may also result in over- or under-estimation of blood flow contrasts in both DCS and ncDCT (67, 83). According to the definition of μ_a^{total}, μ_a, μ_s' and αD_B, variations cannot be completely separated unless they are independently measured. As previous computer simulations suggested ~250% variation in μ_s' distribution may cause ~297% variation in BFI reconstruction, while 200 to 300% variations in μ_a may cause 11.5% to 26% variations in BFI reconstruction (**Chapter 3.3.2**). So when assuming homogeneous optical properties over the entire breast, the realistic heterogeneous optical properties (mainly due to μ_s') across the tumor can generate errors in tumor BFI contrasts. To overcome this limitation, a separate instrument enabling 3-D imaging of μ_a and μ_s' distributions in the breast is needed (e.g., a frequency-domain or time-resolved DOT (32, 120-122)).

We didn't find difference in the reconstructed blood flow contrasts between the benign and malignant breast tumors. Since the number of reconstructed images from two groups of patients was small (n = 14 for benign and n = 4 for carcinoma), the extracted blood flow contrasts may not be generalizable to two groups of patient populations.

Furthermore, some studies also showed similar densities of microvasculature between the low grade breast carcinomas and benign lesions (123), which might result in the overlap of blood flow contrasts between malignant tumors and benign lesions. In addition, measurement and reconstruction errors as mentioned earlier may cause difficulty in distinguishing different tumor types. For example, the crosstalk between the optical properties (mainly due to μ_s') and BFI may induce errors in the reconstructed tumor-to-normal blood flow contrasts. Tumors located at varying depths may lead to certain amount of over- or under-estimations in BFI reconstruction.

In the future study, we should optimize the imaging system and increase patient number to investigate the possibility of using ncDCT for characterization/classification of breast tumors. Overall, the current study demonstrated the potential of ncDCT system to be used for imaging blood flow distributions in soft and vulnerable tissues without distorting tissue hemodynamics.

CHAPTER 6 OPTICAL FIBER MODE OPTIMIZATION FOR BETTER SIGNAL-TO-NOISE RATIO (SNR)

6.1 Introduction

As described in **Chapter 2**, NIR light has been recently employed to noninvasively measure rBF in deep tissues, which is referred to as NIR DCS (38, 41, 54, 58, 65, 75-77, 124) or diffusing wave spectroscopy (DWS) (82, 125, 126). Further development of DCS technology includes ncDCT for 3-D blood flow imaging (**Chapters 3-5**) and a dual-wavelength DCS flow-oximeter (41, 46, 67, 78, 124, 127), which can simultaneously measure rBF and oxygenation variations. High SNR is crucial when applying DCS technologies in study of human tissues where the detected signals are usually very weak (41, 46, 54, 67, 75-78, 92, 127, 128). In this chapter, I report a study exploring the use of different types of detector fibers to experimentally compare/improve the SNRs of DCS flow-oximeter measurements (129).

When using DCS to detect tissue blood flow, a pair of source and detector fibers is usually placed along the tissue surface. Previous studies have used either single-mode (40, 41, 53, 60, 75, 76, 92, 124, 127, 130) or few-mode (131-134) fibers separately for DCS flow detections. A single-mode fiber is an optical waveguide whose very small core radius is comparable with the wavelength of the transported light (131, 135). Light intensity detected by the single-mode fiber, however, is low due to the fact that only the fundamental mode of light can be transported. By contrast, few-mode fibers allow a few higher order modes of light to be guided through the fiber along with the fundamental mode. Enlarging the fiber diameter and numerical aperture (N_A) with few-mode fibers to cover multiple speckles increases the detected signal intensity, thus improving SNR.

Conversely, the multiple speckles detected by the few-mode fibers are uncorrelated and decrease the coherence factor (β) in a proportional fashion (131-134). As a result, the autocorrelation function curve becomes flatter which may reduce the sensitivity of DCS flow measurements (60, 136). The detected light intensity can be further increased using multi-mode fibers with a large core diameter (e.g., 1 mm), although the autocorrelation function may not be detectable due to very low value of β (i.e., the autocorrelation function curve becomes a straight line) (135, 137).

Dual-wavelength DCS flow-oximeter was developed by including a second laser to the DCS device, which enables the extraction of multiple hemodynamic variables including rBF and changes in oxy-hemoglobin concentration ($\Delta[HbO_2]$) and deoxy-hemoglobin concentration ($\Delta[Hb]$). As mentioned earlier, few-mode and multi-mode fibers collect more photons than single-mode fibers which leads to the following hypothesis. Increased light intensities measured at two wavelengths by few-mode or multi-mode fibers should improve the SNRs in measurements of light intensity as well as tissue blood oxygenation.

In this chapter, three fibers with different modes (i.e., single-mode, few-mode or multi-mode) were examined in tissue-like liquid phantoms with varied optical properties and in human forearm muscles during arterial cuff occlusion. The SNRs of the measured variables were calculated and compared to aid in the selection of fiber(s) for the improvement of DCS flow-oximeter measurements.

The work reported in this chapter has been published (129) and reprint permission for this dissertation has been granted by the publisher.

6.2 Methods and Materials

6.2.1 DCS Flow-oximeter

Flow Measurements. DCS flow indices were quantified by a dual-wavelength DCS flow-oximeter with two CW coherent laser sources at 785 and 853 nm (100 mw, Crystalaser, Inc., NV) (46). The coherence length for both lasers was longer than 5 meters. The two DCS sources emitted NIR light alternately into the tissue via two multi-mode optical fibers with a core diameter of 200 μm (WF200/220/245, Ceramoptec, MA) bundled at the same location on the phantom/tissue surface. Three detector fibers, including a single-mode fiber with a core diameter of 4.3 μm (SM600, Fibercore, CA), a 6-mode fiber with a core diameter of 4.5 μm (SM980, Fibercore, CA) and a multi-mode fiber with a core diameter of 1 mm, were confined by a foam pad at an equal distance of 2.5 cm from the two source fiber bundle (Figure 6.1). These detector fibers were connected respectively to three single-photon-counting APDs (PerkinElmer Inc., Canada) inside the DCS device. The outputs of APDs were sent to a 4-channel autocorrelator board yielding normalized light intensity temporal autocorrelation functions $g_2(\boldsymbol{r},\tau)$. As described in DCS theory section (**Chapter 2.3**), by fitting the analytical expression of $g_2(\boldsymbol{r},\tau)$ with the $g_2(\boldsymbol{r},\tau)$ from measurement, the blood flow index αD_B and coherence factor β are extracted simultaneously.

Optical Property Measurements. DCS for flow measurement needs only one wavelength of light source. Adding a second laser to the DCS device allows for simultaneous measurements of tissue optical properties. Photons emitted by lasers are scattered and/or absorbed when they travel through the tissue from the source to detector, leading to light intensity reductions in detected wavelengths. Similar to CW NIRS, the

relative change in the tissue absorption coefficient ($\Delta\mu_a$) can be derived from the light intensity changes measured at the two wavelengths (138). Variations of $\Delta[HbO_2]$ and $\Delta[Hb]$ relative to their baseline values (determined before physiological changes) can be determined from the measured $\Delta\mu_a$ at two wavelengths, using the modified Beer-Lambert Law (73),

$$\Delta[\mathrm{HbO_2}] = \frac{\varepsilon_{Hb}(\lambda_1)\Delta\mu_a(\lambda_2) - \varepsilon_{Hb}(\lambda_2)\Delta\mu_a(\lambda_1)}{\varepsilon_{Hb}(\lambda_1)\varepsilon_{HbO_2}(\lambda_2) - \varepsilon_{HbO_2}(\lambda_1)\varepsilon_{Hb}(\lambda_2)} \ ,$$

$$\Delta[\mathrm{Hb}] = \frac{\varepsilon_{HbO_2}(\lambda_2)\Delta\mu_a(\lambda_1) - \varepsilon_{HbO_2}(\lambda_1)\Delta\mu_a(\lambda_2)}{\varepsilon_{Hb}(\lambda_1)\varepsilon_{HbO_2}(\lambda_2) - \varepsilon_{HbO_2}(\lambda_1)\varepsilon_{Hb}(\lambda_2)} \ . \qquad (6.1)$$

Here $\Delta\mu_a(\lambda) = \ln(I_{\lambda B}/I_{\lambda T})/(d\mathrm{DPF}_\lambda)$, $\varepsilon_{HbO_2}(\lambda)$ and $\varepsilon_{Hb}(\lambda)$ are the extinction coefficients of oxyhemoglobin and deoxyhemoglobin. $I_{\lambda B}$ and $I_{\lambda T}$ are the measured light intensities at the baseline and time T, respectively. The differential path length factor (DPF_λ) denotes the ratio of the mean photon path length to the distance (d) between the source and detector pair.

6.2.2 Optical Fiber Modes

For an optical fiber the number of guided modes depends on the core radius (a), relative refractive-index difference, and operating wavelength (λ). The relation between the properties of a given dielectric optical waveguide (fiber) and guided waves (number of modes) can be described by introducing a normalized frequency V (135):

$$V = \frac{2\pi a}{\lambda}\sqrt{n_1^2 - n_2^2} \qquad (6.2)$$

Here n_1 and n_2 are the refractive indices of fiber core and cladding, respectively. The square root of (n_1^2 - n_2^2) is defined as numerical aperture N_A. When V is smaller than the

critical cutoff frequency V_C (e.g., 2.405 for a step-index fiber whose refractive index is constant within the fiber core), only the fundamental mode LP_{01} can be guided through the fiber. Notice that a single-mode fiber can transmit two independent orthogonally polarized waves; the fiber is actually "bimodal" (135). The operating wavelength corresponding to V_C is called the cutoff wavelength (λ_C). When the value of V is larger than V_C, the fiber can guide a few higher-order modes along with the fundamental mode; it becomes a few-mode fiber. The propagating vector modes, i.e., the transverse electric mode (TE), transverse magnetic mode (TM), or hybrid mode, can be determined by the following three steps: (1) calculating the V value based on the fiber property using Equation 6.2; (2) using the V value to obtain transported linear polarized (LP) modes corresponding from literature values (139) where the LP modes are the eigen-modes of guided conventional modes (i.e., TE, TM, hybrid mode) and each of them has designation of conventional modes (wave modes) (137); (3) determining the guided wave modes according to the compositions of different LP modes.

We used three detector fibers for photon collection in our experiments. According to the method described above, the single-mode fiber (SM600) has a λ_C of ~600 nm, N_A between 0.1 and 0.14, and fiber core diameter of ~4.3 μm which guides only two orthogonal polarization modes of light at the two operating wavelengths of 785 and 853 nm (135). The few-mode fiber (SM980) has a λ_C of ~970 nm, N_A between 0.17 and 0.19, and fiber core diameter of ~4.5 μm which guides six modes of light operating at both 785 and 853 nm wavelengths. In **Chapter 6.3.1** we experimentally checked and confirmed these calculated numbers of guided modes using measured values of $1/\beta$. The third fiber used is a regular multi-mode fiber with a diameter of 1 mm.

6.2.3 Phantom Experiments

Distilled water, India ink and Intralipid were utilized in constructing liquid phantoms which provided a homogeneous tissue model (see details in **Chapter 3.4.1**) (41, 67, 92).

An optical probe shown in Figure 6.1 was placed on the surface of the liquid phantom solution contained inside a glass aquarium. A custom-made probe holder attached to a lab stand held the probe at the center of solution to simulate a semi-infinite geometry. Room light was turned off during experiments. In order to test the SNR at different levels of light intensity, a titration protocol of gradually varying μ_a was applied. The optical property of liquid phantom was set initially at μ_a = 0.05 cm^{-1} and μ_s' = 8 cm^{-1} at 853 nm. The corresponding μ_a and μ_s' for the second wavelength (785 nm) at each titration step were calculated according to the volumes of water, India ink and Intralipid in the phantom solution (67). The μ_a (853 nm) was then gradually increased up to 0.15 cm^{-1} at a step size of 0.025 cm^{-1} by adding ink to the liquid phantom while μ_s' was kept constant (without changing the concentration of Intralipid). Optical measurements were taken by the DCS flow-oximeter for 10 minutes at each titration step and 260 $g_2(\boldsymbol{r}, \tau)$ curves were collected for each wavelength. The measurement duration for each autocorrelation function at each wavelength was 1 second. Only 150 data points measured at each wavelength and each step were used for data analysis, as the noisy data collected during the periods of adding, stirring and dissolving ink were excluded. At the final step of the titration (μ_a = 0.15 cm^{-1}), the light intensity collected by the single-mode fiber (SM600) reached a minimal value of ~10 kilo counts per second (kcps) that could barely be detected by DCS.

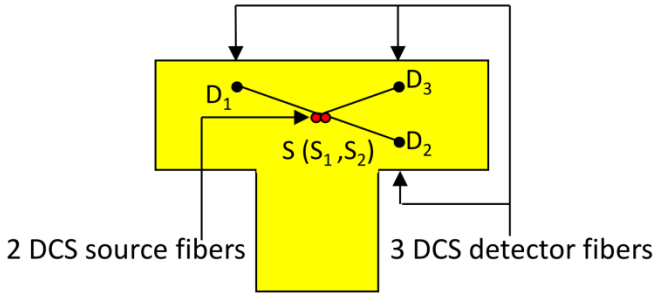

Figure 6.1: A fiber-optic probe consisting of two source fibers (S_1 = 785 nm and S_2 = 853 nm) and three detector fibers (D_1 to D_3). Multi-mode fiber (1mm) locates in D_1, single-mode fiber (SM600) locates in D_2, and few-mode fiber (SM980) locates in D_3. The separations between the sources and detector fibers are equal (i.e., $SD_1 = SD_2 = SD_3 = 2.5$ cm). The separations between detector fibers are $D_1D_2 = 4.6$ cm, $D_1D_3 = 4.3$ cm and $D_2D_3 = 0.8$ cm, respectively.

For flow data analysis theoretical μ_a and μ_s' from the phantom at each titration step were used as inputs when fitting flow index D_B (67). Relative changes in D_B were calculated by normalizing/dividing the time-course data to the mean values of the first titration data. For the analysis of phantom absorption coefficient, $\mu_a(\lambda)$ at the first titration step was assigned to be the theoretical value of the phantom (e.g., μ_a (853 nm) = 0.05 cm^{-1}) and $\mu_a(\lambda)$ values at other titration steps were then calculated by adding the corresponding $\Delta\mu_a(\lambda)$ values measured by the DCS flow-oximeter. Standard deviations of the measured variables were calculated and displayed as error bars along with the mean values.

6.2.4 In vivo Tissue Measurements

The single-mode, few-mode and multi-mode fibers were further used to investigate the SNRs in DCS flow-oximeter measurements on human tissues. The *in vivo* experiments were approved by the University of Kentucky Institutional Review Board.

Seven healthy subjects signed consent forms and participated in this study. Each subject was asked to lay supine on a bed and extend his/her forearm. Prior to the DCS flow-oximeter measurement the commercial tissue-oximeter Imagent with a hand-held probe was used to obtain absolute baseline values of μ_a, μ_s', [Hb] and [HbO_2] in the participant's forearm flexor carpi radialis muscle (71). The hand-held probe was removed and the fiber-optic probe developed for this study (Figure 6.1) was taped on the same location in forearm muscle to continuously monitor rBF, Δ[Hb] and Δ[HbO_2] during 5-minute arterial cuff occlusion. An optical attenuator was attached to the multi-mode detector fiber to avoid saturating the highly sensitive APD. The forearm muscle went through three different physiological stages during the cuff occlusion on upper arm: 5-minute resting baseline, 5-minute cuff inflation (230 mmHg), and 5-minute recovery following cuff deflation.

Similar to the phantom data analysis the baseline μ_a and μ_s' measured by the Imagent were used as inputs when fitting flow index αD_B. Relative changes in αD_B were calculated by normalizing/dividing the time-course data to the mean values of the 5-minute resting baselines. The [Hb] and [HbO_2] were calculated by adding their baseline values measured by the commercial Imagent and the corresponding Δ[Hb] and Δ[HbO_2] measured by the DCS flow-oximeter. To be consistent with the phantom data analysis 150 data points at each stage were used to calculate the corresponding SNRs. Standard errors were calculated over the 7 subjects and plotted as error bars along with the mean values in the figures.

6.2.5 SNR Calculations

The variables measured by or derived from the DCS flow-oximeter include $g_2(\boldsymbol{r},\tau)$, αD_B/rBF, light intensity I, $\Delta\mu_a$, Δ[Hb] and $\Delta[HbO_2]$. SNR calculations for most of these variables follow the conventional definition (140):

$$\text{SNR} = \frac{\text{MEAN}\ (signal)}{\text{STD}\ (noise)} \tag{6.3}$$

Here, *"*STD*"* represents standard deviation, "MEAN" represents mean value, *"signal"* is the measured raw data, and *"noise"* is the high-frequency component of the measured raw data. The high-frequency noises originate from electronics, optics, positioning of the source and detectors, and physiological variations (only applicable to *in vivo* measurements) (9). The electronic noises include shot noise, thermal noise and the noise induced by the dark current of APD. The optic noises arise mainly from the fiber modal noise and the loss/variation of higher order modes due to the fiber bending/vibration. The physiological variations come from the respiration, heartbeat, and subject's movement.

The *"noise"* in **Equation 6.3** for each set of measured raw data (150 data points) was obtained using a first order Butterworth high-pass filter with a corner frequency of 0.05 Hz (83). This corner frequency was determined by analyzing the power spectral densities (PSDs) of the measured hemodynamic signals from forearm muscles, and was selected to be higher than the highest frequency (0.05 Hz) of the valid signals (i.e., slow hemodynamic changes during cuff occlusion) but lower than the DCS sampling rate (~0.4 Hz) and the highest frequency of noises. The MEAN (*signal*) may be equal to 0 for some variables (e.g., rBF ≈ 0 during cuff occlusion), resulting in zero SNR. In this case

the STD (*noise*) was used to evaluate measurement variability.

Unlike those variables (described above) depending only on time (t), $g_2(\boldsymbol{r},\tau)$ is a function of delay time τ at each measurement time point (t). To calculate the SNR of $g_2(\vec{r},\tau)$ at multiple τ, a previously established method is followed (83, 136):

$$\mathrm{SNR}(\tau) = \frac{\mathrm{MEAN}(g_2(\boldsymbol{r},\tau)-1)}{\mathrm{STD}(g_2(\boldsymbol{r},\tau)-1)} \tag{6.4}$$

The calculation was carried out among the 150 datasets of ($g_2(\boldsymbol{r},\tau)$-1). The MEAN and STD of the 150 ($g_2(\boldsymbol{r},\tau)$-1) curves at each delay time τ were used to estimate SNR(τ) according to **Equation 6.4**.

Differences among the three fibers in mean values of SNR or STD averaged over 7 subjects were tested using the SAS (Statistical Analysis System) Version 9.3 software package and assessed by wavelength (only applicable to rBF) and during baseline, cuff occlusion, and recovery stages. Normality of the mean differences over 7 subjects was assessed using Shapiro-Wilks test (141). Any p-value less than 0.10 was considered to result in a departure from normality of the mean difference and a Wilcoxon Signed-Rank test (142) was used to assess whether the mean difference was significant in this case. Where there was no departure from normality the paired t-test was used to assess significance of the mean differences. A p-value of 0.05 was considered significant for the mean differences examined in SNR or STD of rBF between the single-mode and few-mode fibers. A Bonferroni-corrected p-value of 0.017 (0.05/3) was considered significant for the mean differences examined in SNRs or STDs of [Hb] and [HbO_2] between any two groups of single-mode, few-mode and multi-mode fibers.

6.3 Results

6.3.1 Phantom Experimental Results

Flow Measurement. During the phantom titration experiments μ_a (853 nm) was varied from 0.050 cm^{-1} to 0.150 cm^{-1} with a step size of 0.025 cm^{-1} while μ_s' was kept constant (8 cm^{-1}) throughout all steps. Figure 6.2a shows typical $g_2(\boldsymbol{r},\tau)$ data (dots) and fitting curves (solid lines) recorded at 785 nm and collected by the single-mode (SM600) and few-mode (SM980) fibers. The data presented in **Figure 6.2a** were randomly selected from ~150 $g_2(\boldsymbol{r},\tau)$ curves over each titration step. As mentioned in **Chapter 6.2.1**, β and D_B can be simultaneously derived by fitting the measured $g_2(\boldsymbol{r},\tau)$. In addition, β can also be estimated based on the Siegert relation using the measured $g_2(\boldsymbol{r},\tau)$ data at earliest τ and letting the normalized autocorrelation function $g_1 \approx 1$, i.e., $\beta = g_2(\tau \approx 0) - 1$. For example, the β values for the single-mode and few-mode fibers can be estimated by the intercept values of fitted $g_2(\boldsymbol{r},\tau)$ curves, notated as A and B in **Figure 6.2a**. For the first titration (Step 1), the β values calculated over 150 measurements were 0.46 ± 0.013 and 0.16 ± 0.013 for the single-mode (SM600) and few-mode (SM980) fibers, respectively. Correspondingly, $1/\beta$ values were approximately equal to the numbers of guided modes of light (N): ~2 for the single-mode (SM600) fiber and ~6 for the few-mode (SM980) fiber. These numbers agreed with the theoretical values calculated based on fiber properties in **Chapter 6.2.2**. As μ_a increased the $g_2(\vec{r},\tau)$ curves became noisier for both single-mode and few-mode fibers. However, the curves collected by the few-mode fiber were always smoother than those recorded by the single-mode fiber over the titration steps (**Figure 6.2a**). To further quantify the performance of

the two fibers we calculated the SNRs over 150 $g_2(\boldsymbol{r},\tau)$ curves at each delay time τ for all titration steps using the method described in **Chapter 6.2.5**. Results shown in Figure 6.2b indicated that the SNRs of $g_2(\boldsymbol{r},\tau)$ detected by the few-mode fiber were slightly higher than the single-mode fiber, which appeared more obvious at the early decay time τ. Similar results were found at the wavelength of 853 nm (data are not shown).

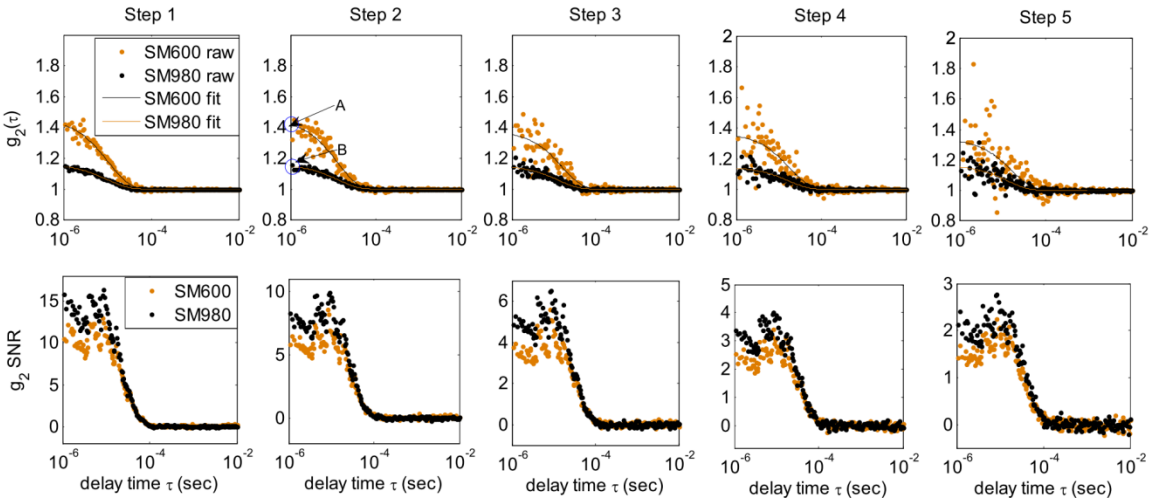

Figure 6.2: (a) Typical $g_2(\boldsymbol{r},\tau)$ data (dots) and fitting curves (solid lines) recorded at 785 nm and collected by the single-mode (SM600) and few-mode (SM980) fibers at five titration steps. The $g_2(\boldsymbol{r},\tau)$ curves are randomly selected at a single measurement time point *t* over 5 steps. The intercepts (e.g., A and B at Step 2) can be used to estimate β values (i.e., β = intercept value -1), which are the inverse of guided mode numbers (~2 for SM600 and ~6 for SM980). (b) Corresponding SNRs calculated from the 150 $g_2(\boldsymbol{r},\tau)$ curves at each titration step.

The relative flow data (normalized D_B) at five titration steps are shown in Figure 6.3a. Vertical lines separate different titration steps. Since multiple uncorrelated speckle fluctuations were collected by the multi-mode fiber (1mm) the measured autocorrelation function curve $g_2(\boldsymbol{r},\tau)$ became completely flat (a straight line) which cannot be fit using the algorithm described in **Chapter 2.3**. Therefore, only flow data (150 data points) collected by the single-mode and few-mode fibers were reported. As μ_a increased relative

flow data recorded at two wavelengths became noisier for both single-mode and few-mode fibers, but the signal fluctuation observed when using the few-mode fiber was less than using the single-mode fiber. The difference in flow variations between the two fibers can be seen more clearly from **Figure 6.3b** where the STDs of noises are illustrated as error bars. Notice that flow increased slightly with the progress of titration which was likely due to the fitting errors at the titration steps with higher μ_a values associated with higher noises (83). **Figure 6.3c** shows the SNRs of relative flow at five titration steps calculated using **Equation 6.3**. The SNRs for both single-mode and few-mode fibers decreased as μ_a increased, and the few-mode fiber achieved slightly higher SNRs than the single-mode fiber. These results are consistent with the findings shown in **Figures 6.3a** and **6.3b**.

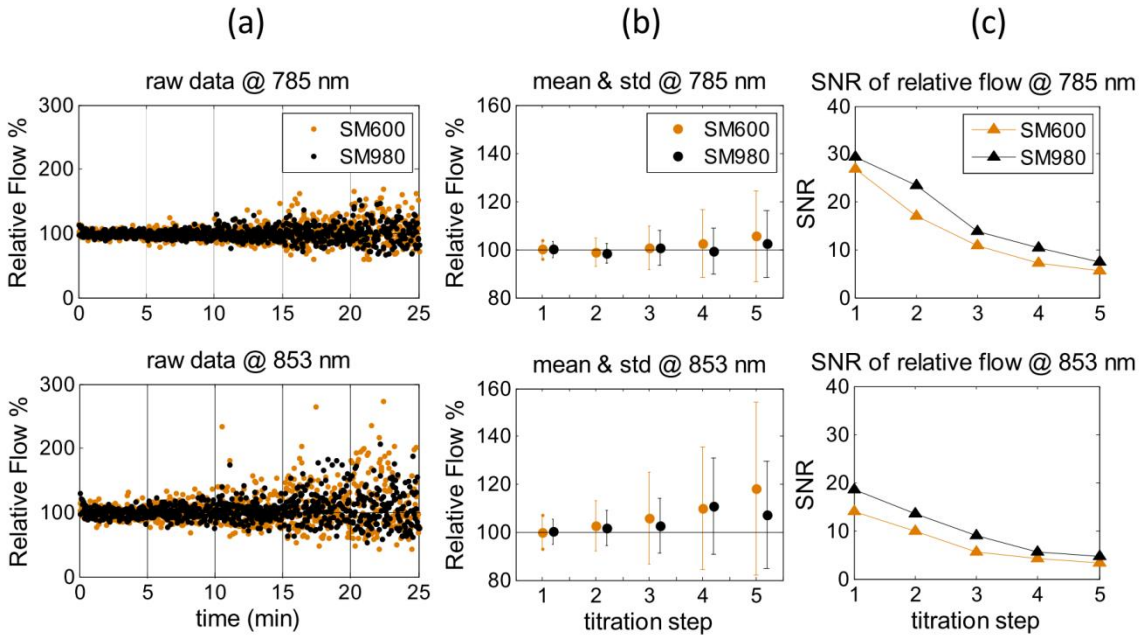

Figure 6.3: (a) Measured relative flow (normalized D_B) during the phantom titration experiment detected by the single-mode (SM600) and few-mode (SM980) fibers at the two wavelengths (785 and 853 nm). (b) Mean values of relative flow and standard deviations of noise (error bars). (c) Corresponding SNRs of relative flow at the two wavelengths and five titration steps.

Optical Property Measurements. **Figure 6.4a** displays the light intensities at two wavelengths collected by the three fibers during titrations. As expected, higher mode fibers collected more photons. **Figure 6.4b** shows the mean values of light intensities and STDs of noises (error bars) at five titration steps. In order to clearly show the error bars they were multiplied by a factor of 100. It can be observed from **Figure 6.4b** that with the increase of light intensity both MEAN (*signal*) and STD (*noise*) increased. The noise level increased because the higher light intensity increased shot noises from the photon detectors and random noises generated by photons transporting through the medium. Nevertheless, the increase of MEAN (*signal*) was larger than the increase of STD (*noise*). As a result, the SNR increased with the increase of light intensity (**Figure 6.4c**). The SNRs tended to decrease with the increase of μ_a, although such decreases were not remarkable at the early titration steps where the light intensities and SNRs were relatively high.

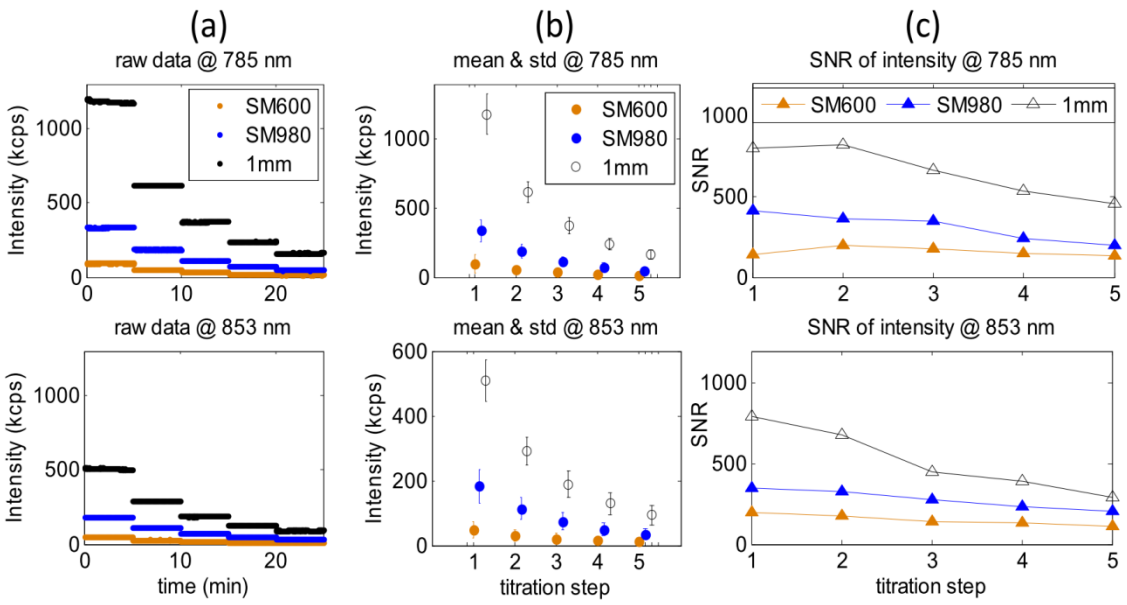

Figure 6.4: (a) Measured light intensities at the two wavelengths (785 and 853 nm) collected by the single-mode (SM600), few-mode (SM980) and multi-mode (1mm) fibers during the phantom titration experiment. The light intensity unit of "kcps" stands for kilo counts per second. (b) Averaged light intensities and standard deviations of noise (error bars) at the two wavelengths. The standard deviations of noise are multiplied by a factor of 100 to clearly display the error bars. (c) Corresponding SNRs of light intensities at the two wavelengths and five titration steps.

The retrieved μ_a values at five titration steps and two wavelengths using the three fibers with different modes are displayed in **Figure 6.5a**. The $\mu_a(\lambda)$ value at the first titration step was assigned to be the theoretical value of the phantom (i.e., μ_a = 0.05 cm^{-1} at the wavelength of 853 nm). **Figure 6.5b** shows the mean values of μ_a and STDs of noises at five steps and two wavelengths. Again, in order to clearly show the error bars they were multiplied by a factor of 100. Horizontal dashed lines displayed in **Figures 6.5a** and **6.5b** indicate the theoretical μ_a values of the phantom at each step. All three fibers were able to extract μ_a with relatively small errors. The measurement error in μ_a was estimated by the percentage difference between the measured and theoretical values. The maximum measurement errors from the few-mode (1.6% at 785 nm and 1.3% at 853

nm) and multi-mode (4.3% at 785 nm and 4.8% at 853 nm) fibers were much smaller than those from the single-mode fiber (6.3% at 785 nm and 11% at 853 nm). Although differences in measurement error existed between the few-mode (≤ 1.6%) and multi-mode (≤ 4.8%) fibers, the measurement errors (< 5%) from both fibers were comparable with previous NIRS results (< 6%) using multi-mode fibers (67, 71). The STDs of measurement noises (error bars) increased with the increase of μ_a and the decrease of fiber mode number. The SNRs of μ_a at the five steps and two wavelengths are displayed in **Figure 6.5c**. It is clear that higher SNRs for μ_a can be achieved by increasing the number of optical fiber modes.

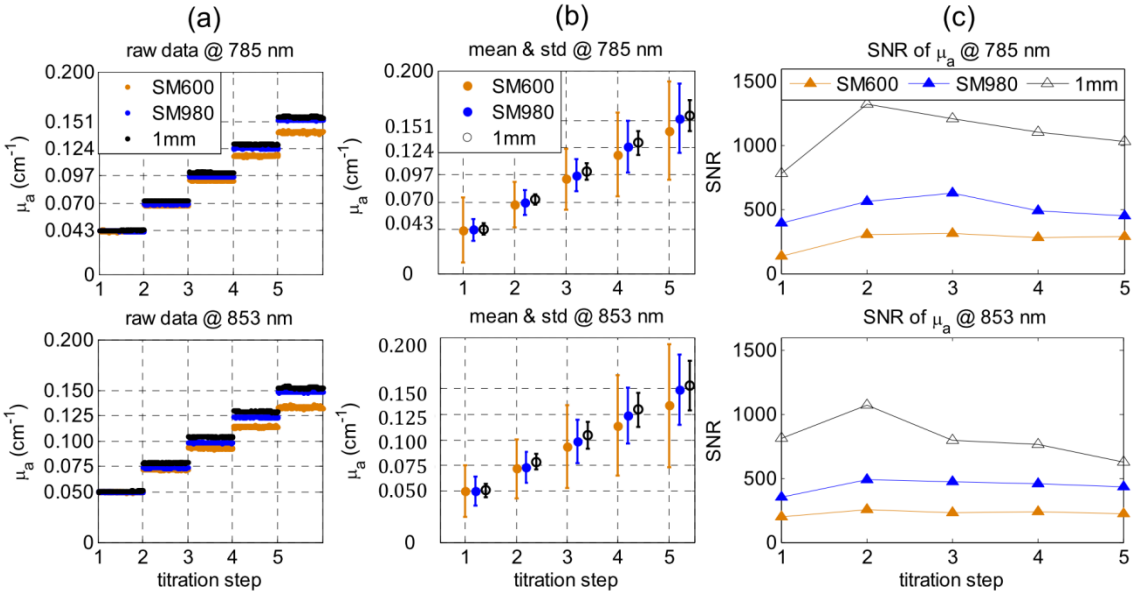

Figure 6.5: (a) Measured μ_a values at the two wavelengths (785 and 853 nm) collected by the single-mode (SM600), few-mode (SM980) and multi-mode (1mm) fibers during the phantom titration experiment. The horizontal dashed lines indicate theoretical μ_a values of the phantom at each step. (b) Averaged μ_a values and standard deviations of noise (error bars) at the two wavelengths. The standard deviations of noise are multiplied by a factor of 100 to clearly display the error bars. (c) Corresponding SNRs of μ_a values at the two wavelengths and five titration steps.

6.3.2 In vivo Tissue Measurement Results

rBF Measurements. **Figure 6.6a** shows typical rBF data at 785 and 853 nm collected by the single-mode and few-mode fibers during 5-minute arterial cuff occlusion from one subject. Similar to phantom measurements the measured $g_2(\boldsymbol{r}, \tau)$ curve collected by the multi-mode fiber (1mm) was a straight line which cannot be used to extract blood flow information. The raw rBF data (150 data points at each stage) were processed by the high-pass filter with a corner frequency of 0.05 Hz to extract the noises (**Figure 6.6b**). Vertical lines in **Figures 6.6a** and **6.6b** separate different stages of occlusion (i.e., baseline, occlusion, recovery). The mean SNRs and standard errors (error bars) over 7 subjects at the baseline and recovery stages are displayed in **Figure 6.6c**. The SNRs of rBF at the occlusion stage were equal to zero and thus not reported. Instead, the STDs of rBF noises and their variations (standard errors shown as error bars) over 7 subjects at all three stages are shown in **Figure 6.6d**. Assessed by SAS software (see **Chapter 6.2.5**), the p-values from the paired t-test/Wilcoxon Signed-Rank tests were larger than 0.222 indicating that the mean differences in SNR/STD of rBF over 7 subjects between the single-mode and few-mode fibers were not significant at all three stages of cuff occlusion.

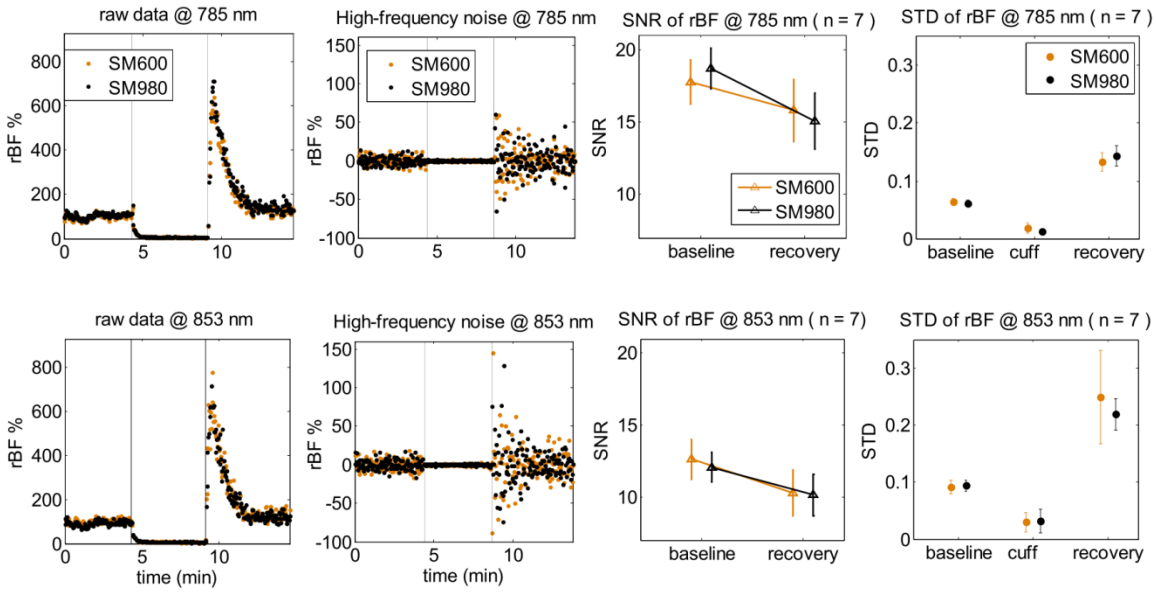

Figure 6.6: (a) Typical forearm muscle rBF responses during 5-minute arterial cuff occlusion collected from one subject using the single-mode (SM600) and few-mode (SM980) fibers. (b) rBF noise processed by the high-pass filter with a corner frequency of 0.05 Hz. (c) Averaged SNRs of rBF and corresponding standard errors (error bars) of noise at baseline and recovery stages over 7 subjects. (d) Averaged standard deviations of high-frequency noises and corresponding standard errors (error bars) at baseline, cuff occlusion, and recovery stages over 7 subjects.

<u>Oxygenation Measurements.</u> **Figure 6.7a** displays the [Hb] and [HbO_2] data during 5-minute arterial occlusion measured by the three fibers with different modes from the same subject shown in **Figure 6.6**. Apparently, [Hb] and [HbO_2] curves became smoother (**Figure 6.7a**) and noises were less (**Figure 6.7b**) when using higher mode fibers. **Figure 6.7c** displays the mean SNRs and their standard errors (error bars) over 7 subjects. Assessed by SAS software (see **Chapter 6.2.5**), the p-values from the paired t-test/Wilcoxon Signed-Rank tests were smaller than 0.016 when evaluating the significance between the few-mode and single-mode fibers and between the multi-mode and single-mode fibers. As noted in **Chapter 6.2.5** a Bonferroni-corrected p-value of < 0.017 was considered significant. This result indicated that the mean SNRs of both [Hb]

and [HbO_2] using the few-mode and multi-mode fibers were significantly higher than those using the single-mode fiber.

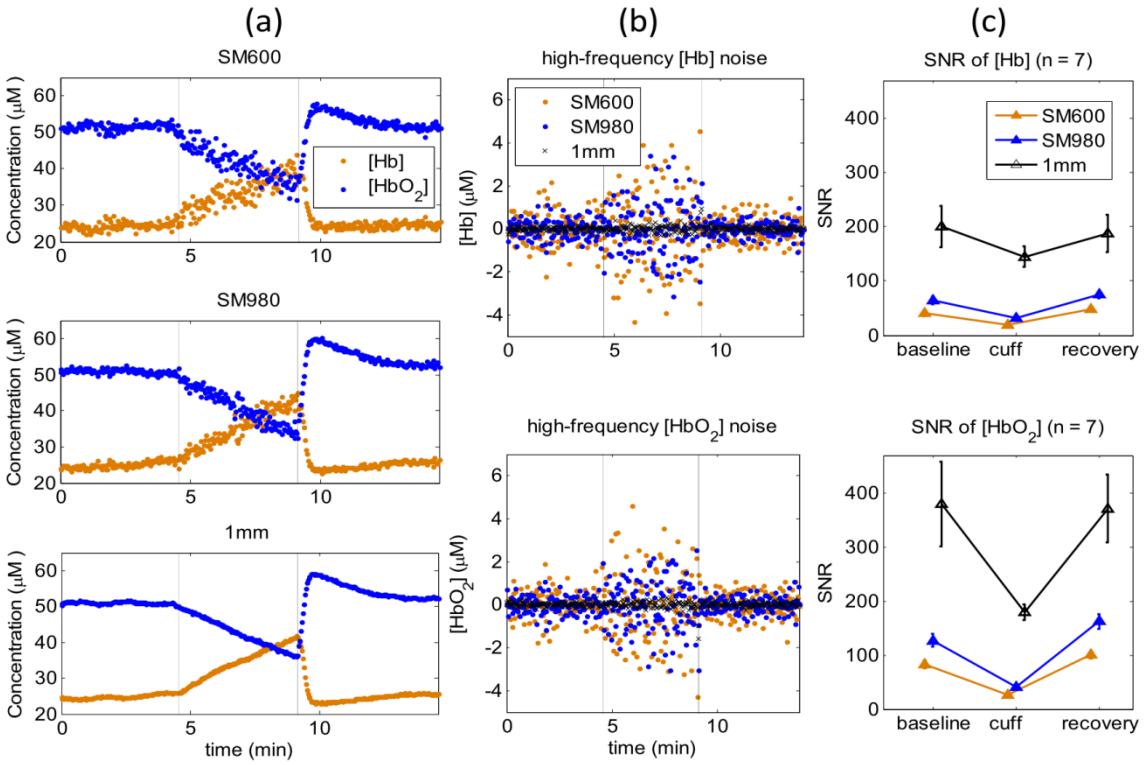

Figure 6.7: (a) Typical [Hb] and [HbO_2] responses during 5-minute arterial cuff occlusion collected from the same subject shown in Figure 6.6 using the single- (SM600), few- (SM980) and multi-mode (1mm) fibers. (b) [Hb] and [HbO_2] noises processed by the high-pass filter with a corner frequency of 0.05 Hz. (c) Averaged SNRs of [Hb] and [HbO_2] and corresponding standard errors (error bars) of noises at baseline, cuff occlusion, and recovery stages over 7 subjects.

6.4 Discussion and Conclusions

Traditional NIRS can measure tissue optical properties including μ_a, μ_s', [Hb] and [HbO_2] while the emerging DCS can measure rBF in deep tissues. By combining these two technologies to form a hybrid instrument, rBF, [Hb] and [HbO_2] can be obtained simultaneously (55, 66). Consequently, relative changes in tissue oxygen metabolism can

be derived using simple models (55, 59, 66). While the hybrid instruments (NIRS + DCS) can be used to measure multiple hemodynamic/metabolic parameters providing deeper insights about tissue physiological status than one parameter alone, they are relatively large, complex and expensive. The dual-wavelength DCS flow-oximeter is an emerging technique enabling simultaneous measurements of tissue blood flow and oxygenation changes (41, 46, 67, 78, 127). Being noninvasive, fast, relatively inexpensive and truly portable (dimensions: 8"× 12"×18"), DCS flow-oximeter is suitable for bedside monitoring in the clinics. Furthermore, the new probe designed for the DCS flow-oximeter shares source and detector fibers for both flow and oxygenation measurements. Therefore, it covers exactly the same tissue volume and avoids any discrepancies between the blood flow and oxygenation measurements owing to the tissue heterogeneity.

For clinical measurements large light penetration is needed to probe optical properties in deep tissues (e.g., adult brain and muscle). According to photon diffusion theory a given source-detector (S-D) pair is mostly sensitive to the area at a depth of 1/3 to 1/2 of the S-D separation (45, 65, 67, 143). However, the larger the S-D separation the weaker the signal detected. Improving SNR is especially crucial when the detected signal is extremely low which is not unusual for DCS measurements in human tissues (40, 41, 54, 75-78).

According to **Equation 6.3**, SNR can be improved by increasing the light intensity injected into the tissue which is, however, not unlimited and has to be controlled to meet ANSI (American National Standards Institute) standards for laser safety usage. An alternative method is to use a low-pass filter to reduce the high frequency noises, but this may not be possible when the bandwidths of signal and noise are overlapped. This study

was designed to investigate the possibility of using the few-mode or multi-mode detection fibers instead of the single-mode fiber to increase the light intensity detected and thus improve SNRs of DCS flow-oximeter measurements. The rationale behind this hypothesis is that few-mode or multi-mode fibers allow higher order modes of light to be guided through along with the fundamental single mode which would increase the light intensity detected (135).

To test the hypothesis the single-mode (SM600), few-mode (SM980) and multi-mode (1mm) fibers were examined in tissue-like liquid phantoms with varied optical properties and in forearm muscles during arterial cuff occlusion. The liquid phantom provided a homogeneous tissue model without the interference of physiological variations that exist in biological tissues (41, 67, 92), while the use of human muscles allowed for the evaluation of fiber performance in real tissues (39, 76, 77, 127, 128).

The results obtained from the phantom titration experiments indicated that the few-mode fiber slightly improved the SNRs of relative flow measurements compared to the single-mode fiber used (see **Figure 6.3c**). Although the slight SNR improvement in flow measurements was somewhat disappointing it was not surprising because the few-mode fiber with larger diameter and numerical aperture increased the detected signal intensity (see **Figures 6.4a** and **6.4b**) but decreased the coherence factor β in a proportional fashion (see **Figure 6.2a**). A smaller β corresponded with a flatter autocorrelation function curve leading to a lower sensitivity of DCS flow measurements (60, 136). Therefore, the SNR of autocorrelation function, depending on both light intensity detected and coherence factor β (136), may not be highly improved (see Figure 6.2b). Although the detected light intensity can be further increased by using the multi-mode

fiber with a large diameter of 1 mm (see **Figures 6.4a** and **6.4b**) the autocorrelation function was not detectable in this case due to the very low value of β. Furthermore, the SNR improvements were not obvious during *in vivo* rBF measurements in forearm muscles (see **Figures 6.6c** and **6.6d**). Unlike phantom experiments *in vivo* measurements could be influenced by many factors such as physiological variations, motion artifacts, fiber-tissue coupling coefficient and tissue heterogeneity which could impact the measurements differently on different fibers (39, 54, 124, 128). Such *in vivo* "noises" may bury the slight SNR improvements of flow measurements observed in phantom experiments.

In contrast to flow measurements, significant SNR improvements were achieved when using the few-mode or multi-mode fiber (versus single-mode fiber) in both phantom measurements of light intensity (see **Figures 6.4c**) and μ_a (see **Figures 6.5c**) and in *in vivo* measurements of [Hb] and [HbO_2] (see **Figures 6.7c**). The significant SNR improvements for these variables were expected as they all depended on the light intensities detected which were highly different among the three fibers (see **Figures 6.4a** and **6.4b**). The larger the number of optical fiber mode the higher the detected light intensity.

The level of the detected light intensity also greatly impacted SNRs of the measured variables at different titration steps and different physiological stages. For example, with the increase of μ_a during the phantom titration the detected light intensity decreased step by step leading to a continual decrease in SNRs for all three fibers and two wavelengths (see **Figures 6.3** and **6.4**). One exception is the derived value of μ_a during phantom experiments where the SNRs of μ_a at the first titration step for both wavelengths were

lower than those at other steps (see **Figures 6.5c**), although the light intensities detected at the first step were higher (see **Figures 6.4a** and **6.4b**). Since the μ_a values at the first titration step were much smaller than those at other steps (e.g., ~1.5 times smaller than the second step) but the STDs of μ_a at all steps didn't vary much, it was not surprising that the SNRs of μ_a at the first titration step for both wavelengths were smaller than those at other steps according to **Equation 6.3**. Furthermore, the SNRs of [Hb] and [HbO_2] during the cuff occlusion stage were lower than those at baseline and recovery stages for all three fibers (see **Figure 6.7c**) which was again due to the lower light intensities detected during occlusion compared to other two stages. In addition, the light intensity detected from the wavelength of 853 nm was ~2 times lower than the 785 nm wavelength (see **Figures 6.4a** and **6.4b**) resulting in lower SNRs for the 853 nm wavelength at most titration steps and physiological stages (see **Figures 6.3** to **6.6**), although laser stability could also impact the SNRs.

Besides the SNR improvements the few-mode and multi-mode fibers measured the optical property μ_a more accurately than the single-mode fiber (see **Figures 6.5a** and **6.5b**). Smaller measurement error represented higher measurement accuracy. The measurement errors in μ_a from the few-mode and multi-mode fibers were < 5% for both wavelengths (**Figure 6.5a**) which were comparable with those (< 6%) observed in previous studies using NIRS with multi-mode fibers (67, 71). The maximum errors from the single-mode fiber (< 11%) were much larger than those from the other two fibers (<5%) (**Figure 6.5a**) and those reported in literature (< 6%), which was again due to less light intensities collected (associated with higher noises) by the single-mode fiber.

In conclusion, the experiments in this chapter demonstrated the advantages of using

the few-mode fiber for DCS flow-oximeter measurements of both blood flow and oxygenation compared to using the single-mode fiber. The few-mode fiber enabled collection of more photons from the phantoms/tissues resulting in higher SNRs in both flow and oxygenation measurements, although the SNR improvements with the few-mode fiber were found to be significant only in oxygenation measurements. The multi-mode fiber can further increase the detected light intensities and SNRs for tissue oxygenation measurements, but the autocorrelation functions for extracting flow information cannot be detected due to the very low value of β.

Based on these results, selection of fibers with certain modes may depend on the particular application. For the measurements of blood flow only either single-mode fiber or few-mode fiber can be used, although the few-mode fiber may generate slightly higher SNRs of flow data. For simultaneous measurements of tissue blood flow and oxygenation using the dual-wavelength DCS flow-oximeter, a few-mode fiber (instead of single-mode fiber) should be used to obtain significantly higher SNRs of tissue oxygenation measurements. An alternative way is to use a detection fiber bundle consisting of one single-mode (or few-mode) fiber and one multi-mode fiber. The single-mode or few-mode fiber can measure autocorrelation functions to extract flow information while the multi-mode fiber can detect light intensities at the two wavelengths with significantly higher SNRs (than both single-mode and few-mode fibers) to extract oxygenation information. However, the latter option requires two detectors connected to the fiber bundle which would increase the instrumentation costs.

This pilot study was limited to comparing the SNRs of DCS flow-oximeter measurements among three types of fibers (i.e., single-mode, few-mode, multi-mode).

The selection of these specific three fibers was mainly based on fiber availability. The optimization of fiber modes used for achieving optimum SNRs in tissue hemodynamic measurements may be the subject of future study.

CHAPTER 7 STUDY SUMMARY, LIMITATIONS, AND FUTURE PERSPECTIVES

7.1 Study Summary

In this dissertation, I reported the development and application of ncDCT system for 3-D blood flow imaging in human breast tumors. The imaging system utilized lens focusing apparatus to project source and detector fibers onto tissue surface. A motorized stage was integrated into the system for automated and customizable ROI scanning around tumor bearing region. A commercial 3-D camera was used to obtain breast surface geometry which was then converted to a solid volume mesh. Furthermore, a finite element framework was integrated to our DCT imaging algorithm which enabled blood flow imaging with arbitrary tissue geometry. System validation work including computer simulations and phantom experiments were performed to demonstrate the imaging ability of the ncDCT system for breast tumor detection. I also reported our first step to adapt the ncDCT system for tumor-to-normal blood flow contrast imaging from patients with breast tumors. In addition to this primary study, an optical fiber study was conducted to improve the SNR of DCS flow-oximeter measurement. The results reported in this dissertation have been presented in conferences and some of them have been published in peer-reviewed journals (see my attached CV).

My major contributions in these studies include the following aspects:

First, I developed the imaging algorithms for ncDCT of breast tumor blood flow contrasts (**Chapter 2**) (37, 144). I designed computer simulations and conducted

phantom experiments to validate and optimize the algorithms and the ncDCT system (**Chapters 3** and **4**).

Second, I participated in the design and construction of noncontact DCS/DCT system (**Chapter 3**) (37, 89, 92). I first involved in the design of a noncontact DCS (ncDCS) probe with single S-D separation. I designed and performed phantom and human tissue experiments to test the ncDCS probe. When extended the ncDCS to ncDCT, I further performed computer simulations to optimize the source and detector arrangement, and the scanning protocol for boundary data collection. To generate breast-shaped mesh, I utilized different commercial software (i.e., ScanStudio, Ansys and SolidWorks) to convert breast surface geometry, taken by a 3-D camera, to solid volume mesh for ncDCT image reconstruction.

Third, for the first time I applied the ncDCT system on clinical breast tumor study (**Chapter 5**) (144). I recruited 28 patients with breast tumors and performed optical measurements. I was able to reconstruct 3-D images of tumor blood flow distributions inside breasts and the majority of reconstructed images showed higher blood flow contrasts in the tumor regions compared to the surrounding normal tissues. Reconstructed tumor depths and dimensions matched ultrasound imaging results when the tumors were within the sensitive region of light propagation. The results demonstrated that ncDCT system has the potential to image blood distributions in soft and vulnerable tissues without distorting tissue hemodynamics.

Last, in order to improve the SNR of DCS flow-oximeter measurements, I experimentally explored using different detector fibers with different modes (i.e., single-mode, few-mode, multimode) for photon collections (**Chapter 6**) (129). The outcomes

from this study provided useful guidance for the selection of optical fibers to improve DCS flow-oximeter measurements.

7.2 Study Limitation and Future Perspectives

Tumor Location Recovery. The ncDCT imaging results from computer simulations and *in vivo* breast tumor measurements suggest that reconstructed tumor depths and dimensions are accurate when the anomaly/tumor was within the sensitive depth of diffuse light. When the tumor locates deeper than the maximal light penetration depth, lower part of the tumor cannot be sampled by the ncDCT probe (**Figure 2.1a**). Consequently, the reconstructed tumor location may be shifted up. Depth correction algorithms should be considered for the imaging process for improvement (106, 107); more weights may be added to elements located deep in the volume mesh when calculating the Jacobian matrix. On the other hand, prior knowledge of tumor location and dimension can also improve the recovery of tumor flow contrasts and locations using anatomical imaging modalities such as MRI or CT. It should be noted that ncDCT cannot detect tumors located deeper than diffuse lights can reach.

Tumor Flow Contrast Recovery. Even though the ncDCT system can detect the majority of breast tumors measured, we were unable to differentiate between malignant and benign tumors with the detected blood flow contrasts. This might be due to the overlap of blood flow contrast in different stages of malignant tumors and different types of benign lesions. Crosstalk between μ_a, μ_s' and BFI may also result in over- or under-estimation of blood flow contrasts in ncDCT (67, 83). To overcome this limitation, a separate instrument enabling 3-D imaging of μ_a and μ_s' distributions of breast tissue is

needed (e.g., a frequency-domain or time-resolved DOT (32, 120-122)). We can also increase the valid boundary measurement pairs by updating our line-shaped sources and detectors arrangement to 2-D array, so that the ill-posed inverse problem could be reduced to improve the flow contrast reconstruction accuracy.

Clinical Limitations and Improvements. Current measurement protocol takes ~40 minutes for each individual measurement. However, sometimes patients may move during the measurement, leading to motion artifacts or even the discontinuity of data collection. In the future, ncDCT measurement time should be reduced. The 2-D array of sources and detectors arrangement mentioned earlier can avoid the scanning procedure and thus avoiding such influence (145).

It is expected that with further instrument and algorithm development and more clinical applications in large patient population, our ncDCT system may emerge as an alternative functional imaging modality to help detect/characterize different kinds of breast tumors. Furthermore, ncDCT can be used for other applications such wound tissue and pressure ulcer without distorting hemodynamic properties.

APPENDIX: GLOSSARY

SYMBOLS

α	Ratio of Dynamic to Static Scatterers (0-1)
D	Photon Diffusion Constant
D_B	Effective Diffusion Coefficient
g_1	Normalized Electric Field Temporal Autocorrelation Function
G_1	Unnormalized Electric Field Temporal Autocorrelation Function
g_2	Normalized Intensity Temporal Autocorrelation Function
I	Intensity
k_0	Wavevector of Photons in Medium ($k_0 = 2\pi n/\lambda$)
λ	Wavelength
n	Ratio of Sample and Air Index of Refraction
N_A	Numerical Aperture
φ	Phase Modulation of NIR Light
ρ	Source-detector Separation
r	Position Vector
$<\Delta r^2(\tau)>$	Mean-square Displacement of Scatterers during τ
S_0	Source-light Distribution
Φ	Photon Fluence Rate
τ	Correlation Function Delay Time
τ_1	Selected Delay Time for DCT Image Reconstruction
μ_s'	Reduced Scattering Coefficient
μ_a	Static Absorption Coefficient

μ_a^d	Effective Dynamic Absorption
μ_a^{total}	Total Absorption Coefficient
ν	Speed of Light in Medium
V	Fiber Normalized Frequency
V_C	Fiber Cutoff Frequency
[x]	Concentration of x
ω	Angular Frequency of Modulation
β	Coherence Factor
λ_C	Fiber Cutoff Wavelength

TERMS

APD	Avalanche Photodiode
BFI	Blood Flow Index (αD_B)
CW	Continuous Wave
CT	Computed Tomogaphy
C_v	Coefficient of Variation
DCS	Diffuse Correlation Spectroscopy
(nc)DCT	(noncontact) Diffuse Correlation Tomography
DWS	Diffusing Wave Spectroscopy
FD	Frequency Domain
FWHM	Full Width Half-maximum
Hb	Deoxy-hemoglobin
HbO_2	Oxy-hemoglobin

J	Jacobian Matrix
NIR	Near-Infrared
NIRS	Near-Infrared Spectroscopy
PET	Positron Emission Tomography
RBC	Red Blood Cell
rBF	Relative Blood Flow
S-D	Source-Detector
SNR	Signal to Noise Ratio
S_tO_2	Tissue Oxygen Saturation
TD	Time Domain
tHb	Total Hemoglobin

REFERENCES

1. "Non-Cancerous Breast Conditions," American Cancer Society, http://www.cancer.org/acs/groups/cid/documents/webcontent/003180-pdf.pdf (2015).

2. Carol DeSantis, Rebecca Siegel, and A. Jemal, "Breast cancer facts and figures 2013-2014," *American Cancer Society* 1-38 (2013).

3. M. Guray, and A. A. Sahin, "Benign breast diseases: classification, diagnosis, and management," *The oncologist* **11**(5), 435-449 (2006).

4. C. Markopoulos et al., "Breast cancer in ectopic breast tissue," *European journal of gynaecological oncology* **22**(2), 157-159 (2001).

5. M. F. O'Hara, and D. L. Page, "Adenomas of the breast and ectopic breast under lactational influences," *Human pathology* **16**(7), 707-712 (1985).

6. W. D. Dupont, and D. L. Page, "Risk factors for breast cancer in women with proliferative breast disease," *The New England journal of medicine* **312**(3), 146-151 (1985).

7. P. L. Fitzgibbons, D. E. Henson, and R. V. Hutter, "Benign breast changes and the risk for subsequent breast cancer: an update of the 1985 consensus statement. Cancer Committee of the College of American Pathologists," *Archives of pathology & laboratory medicine* **122**(12), 1053-1055 (1998).

8. L. C. Hartmann et al., "Benign breast disease and the risk of breast cancer," *The New England journal of medicine* **353**(3), 229-237 (2005).

9. R. Choe, "Diffuse optical tomography and spectroscopy of breast cancer and fetal brain," University of Pennsylvania (2005).

10. R. Siegel et al., "Cancer statistics, 2014," *CA: a cancer journal for clinicians* **64**(1), 9-29 (2014).

11. C. H. Lee et al., "Breast cancer screening with imaging: recommendations from the Society of Breast Imaging and the ACR on the use of mammography, breast MRI, breast ultrasound, and other technologies for the detection of clinically occult breast cancer," *Journal of the American College of Radiology : JACR* **7**(1), 18-27 (2010).

12. N. F. Boyd et al., "Mammographic density and the risk and detection of breast cancer," *The New England journal of medicine* **356**(3), 227-236 (2007).

13. M. Nothacker et al., "Early detection of breast cancer: benefits and risks of supplemental breast ultrasound in asymptomatic women with mammographically dense breast tissue. A systematic review," *BMC cancer* **9**(335 (2009).

14. R. P. Beaney et al., "Positron emission tomography for in-vivo measurement of regional blood flow, oxygen utilisation, and blood volume in patients with breast carcinoma," *Lancet* **1**(8369), 131-134 (1984).

15. N. K. Tafreshi et al., "Molecular and functional imaging of breast cancer," *Cancer control : journal of the Moffitt Cancer Center* **17**(3), 143-155 (2010).

16. K. K. Lindfors et al., "Dedicated breast CT: initial clinical experience," *Radiology* **246**(3), 725-733 (2008).

17. S. Escalona et al., "A systematic review of FDG-PET in breast cancer," *Medical oncology* **27**(1), 114-129 (2010).

18. E. L. Rosen, W. B. Eubank, and D. A. Mankoff, "FDG PET, PET/CT, and breast cancer imaging," *Radiographics : a review publication of the Radiological Society of North America, Inc* **27 Suppl 1**(S215-229 (2007).

19. L. V. Wang, and H.-i. Wu, *Biomedical optics: principles and imaging*, John Wiley & Sons (2012).

20. P. T. So et al., "Two-photon excitation fluorescence microscopy," *Annual review of biomedical engineering* **2**(1), 399-429 (2000).

21. J. G. Fujimoto, "Optical coherence tomography for ultrahigh resolution in vivo imaging," *Nature biotechnology* **21**(11), 1361-1367 (2003).

22. D. Huang et al., "Optical coherence tomography," *Science* **254**(5035), 1178-1181 (1991).

23. S. D. Konecky, "Non-invasive imaging of breast cancer with diffusing near-infrared light," University of Pennsylvania (2008).

24. N. S. Claxton, T. J. Fellers, and M. W. Davidson, "Laser scanning confocal microscopy," *Department of Optical Microscopy and Digital Imaging, Florida State University, Tallahassee, http://www. olympusconfocal. com/theory/LSCMIntro. pdf* (2006).

25. X. Wang et al., "Noninvasive laser-induced photoacoustic tomography for structural and functional in vivo imaging of the brain," *Nature biotechnology* **21**(7), 803-806 (2003).

26. X. Wang et al., "Noninvasive photoacoustic angiography of animal brains in vivo with near-infrared light and an optical contrast agent," *Opt Lett* **29**(7), 730-732 (2004).

27. V. Ntziachristos et al., "Looking and listening to light: the evolution of whole-body photonic imaging," *Nature biotechnology* **23**(3), 313-320 (2005).

28. R. A. Kruger et al., "Photoacoustic angiography of the breast," *Medical physics* **37**(11), 6096-6100 (2010).

29. M. Heijblom et al., "Visualizing breast cancer using the Twente photoacoustic mammoscope: What do we learn from twelve new patient measurements?," *Optics express* **20**(11), 11582-11597 (2012).

30. M. H. Xu, and L. H. V. Wang, "Photoacoustic imaging in biomedicine," *Rev Sci Instrum* **77**(4), (2006).

31. D. A. Boas, C. Pitris, and N. Ramanujam, *Handbook of biomedical optics*, CRC press (2011).

32. R. Choe et al., "Differentiation of benign and malignant breast tumors by in-vivo three-dimensional parallel-plate diffuse optical tomography," *Journal of biomedical optics* **14**(2), 024020 (2009).

33. B. J. Tromberg et al., "Assessing the future of diffuse optical imaging technologies for breast cancer management," *Medical physics* **35**(6), 2443-2451 (2008).

34. Q. Zhu et al., "Early-stage invasive breast cancers: potential role of optical tomography with US localization in assisting diagnosis," *Radiology* **256**(2), 367-378 (2010).

35. Q. Fang et al., "Combined optical and X-ray tomosynthesis breast imaging," *Radiology* **258**(1), 89-97 (2011).

36. M. L. Flexman et al., "Digital optical tomography system for dynamic breast imaging," *Journal of biomedical optics* **16**(7), 076014 (2011).

37. Y. Lin et al., "Three-dimensional flow contrast imaging of deep tissue using noncontact diffuse correlation tomography," *Appl Phys Lett* **104**(12), (2014).

38. D. A. Boas, L. E. Campbell, and A. G. Yodh, "Scattering and Imaging with Diffusing Temporal Field Correlations," *Phys Rev Lett* **75**(9), 1855-1858 (1995).

39. G. Q. Yu et al., "Validation of diffuse correlation spectroscopy for muscle blood flow with concurrent arterial spin labeled perfusion MRI," *Optics Express* **15**(3), 1064-1075 (2007).

40. R. C. Mesquita et al., "Direct measurement of tissue blood flow and metabolism with diffuse optics," *Philos T R Soc A* **369**(1955), 4390-4406 (2011).

41. L. Dong et al., "Noninvasive diffuse optical monitoring of head and neck tumor blood flow and oxygenation during radiation delivery," *Biomed. opt. express* **3**(2), 259-272 (2012).

42. G. Yu, "Diffuse correlation spectroscopy (DCS): a diagnostic tool for assessing tissue blood flow in vascular-related diseases and therapies," *Current Medical Imaging Reviews* **8**(3), 194-210 (2012).

43. C. Zhou et al., "Acute functional recovery of cerebral blood flow after forebrain ischemia in rat," *Journal of Cerebral Blood Flow & Metabolism* **28**(7), 1275-1284 (2008).

44. T. Durduran et al., "Diffuse optical measurement of blood flow, blood oxygenation, and metabolism in a human brain during sensorimotor cortex activation," *Opt Lett* **29**(15), 1766-1768 (2004).

45. T. Durduran, "Non-invasive measurements of tissue hemodynamics with hybrid diffuse optical methods," in *Physics and Astronomy*, p. 266, University of Pennsylvania (2004).

46. Y. Shang et al., "Portable optical tissue flow oximeter based on diffuse correlation spectroscopy," *Optics letters* **34**(22), 3556-3558 (2009).

47. E. M. Buckley et al., "Cerebral hemodynamics in preterm infants during positional intervention measured with diffuse correlation spectroscopy and transcranial Doppler ultrasound," *Optics Express* **17**(15), 12571-12581 (2009).

48. N. Roche-Labarbe et al., "Noninvasive optical measures of CBV, StO(2), CBF index, and rCMRO(2) in human premature neonates' brains in the first six weeks of life," *Hum Brain Mapp* **31**(3), 341-352 (2010).

49. M. C et al., "An integrated approach to measuring tumor oxygen status using human melanoma xenografts as a model.," *Cancer Res.* **63**(21), (2003).

50. G. Yu et al., "Noninvasive monitoring of murine tumor blood flow during and after photodynamic therapy provides early assessment of therapeutic efficacy," *Clin Cancer Res* **11**(9), 3543-3552 (2005).

51. M. N. Kim et al., "Noninvasive Measurement of Cerebral Blood Flow and Blood Oxygenation Using Near-Infrared and Diffuse Correlation Spectroscopies in Critically Brain-Injured Adults," *Neurocrit Care* **12**(2), 173-180 (2010).

52. C. Zhou et al., "Diffuse optical monitoring of hemodynamic changes in piglet brain with closed head injury," *Journal of biomedical optics* **14**(3), (2009).

53. C. Zhou et al., "Diffuse optical monitoring of blood flow and oxygenation in human breast cancer during early stages of neoadjuvant chemotherapy," *Journal of biomedical optics* **12**(5), (2007).

54. G. Yu, "Near-infrared diffuse correlation spectroscopy in cancer diagnosis and therapy monitoring," *Journal of biomedical optics* **17**(1), 010901 (2012).

55. T. Durduran et al., "Diffuse optical measurement of blood flow in breast tumors," *Opt Lett* **30**(21), 2915-2917 (2005).

56. R. Choe, and T. Durduran, "Diffuse Optical Monitoring of the Neoadjuvant Breast Cancer Therapy," *IEEE journal of selected topics in quantum electronics : a publication of the IEEE Lasers and Electro-optics Society* **18**(4), 1367-1386 (2012).

57. D. R. Busch et al., "Towards non-invasive characterization of breast cancer and cancer metabolism with diffuse optics," *PET clinics* **8**(3), (2013).

58. D. A. Boas, and A. G. Yodh, "Spatially varying dynamical properties of turbid media probed with diffusing temporal light correlation," *J Opt Soc Am A* **14**(1), 192-215 (1997).

59. J. P. Culver et al., "Diffuse optical tomography of cerebral blood flow, oxygenation, and metabolism in rat during focal ischemia," *J Cerebr Blood F Met* **23**(8), 911-924 (2003).

60. C. Zhou et al., "Diffuse optical correlation tomography of cerebral blood flow during cortical spreading depression in rat brain," *Opt Express* **14**(1125-1144 (2006).

61. W. G. Zijlstra, A. Buursma, and W. P. Meeuwsen-van der Roest, "Absorption spectra of human fetal and adult oxyhemoglobin, de-oxyhemoglobin, carboxyhemoglobin, and methemoglobin," *Clinical chemistry* **37**(9), 1633-1638 (1991).

62. A. Yodh, and B. Chance, "Spectroscopy and Imaging with Diffusing Light," *Phys Today* **48**(3), 34-40 (1995).

63. B. Chance, and R. R. Alfano, "Proceedings of Optical Tomography, Photon Migration, and Spectroscopy of Tissue and Model Media: Theory, Human Studies, and Instrumentation," *SPIE* (1995).

64. A. Yodh, and D. Boas, "Functional imaging with diffusing light," *Biomedical photonics handbook* **21**(1), 21-45 (2003).

65. D. A. Boas, "Diffuse photon probes of structural and dynamical properties of turbid media: theory and biomedical applications," University of Pennsylvania (1996).

66. C. Cheung et al., "In vivo cerebrovascular measurement combining diffuse near-infrared absorption and correlation spectroscopies," *Phys Med Biol* **46**(8), 2053-2065 (2001).

67. D. Irwin et al., "Influences of tissue absorption and scattering on diffuse correlation spectroscopy blood flow measurements," *Biomed Opt Express* **2**(7), 1969-1985 (2011).

68. M. S. Patterson et al., "Absorption spectroscopy in tissue-simulating materials: a theoretical and experimental study of photon paths," *Applied optics* **34**(1), 22-30 (1995).

69. A. Kienle, and M. S. Patterson, "Improved solutions of the steady-state and the time-resolved diffusion equations for reflectance from a semi-infinite turbid medium," *J Opt Soc Am A* **14**(1), 246-254 (1997).

70. D. M. Hueber et al., "New optical probe designs for absolute (self-calibrating) NIR tissue hemoglobin measurements," *BiOS'99 International Biomedical Optics Symposium* 618-631 (1999).

71. S. Fantini, M. A. Franceschini, and E. Gratton, "Semi-infinite-geometry boundary problem for light migration in highly scattering media: a frequency-domain study in the diffusion approximation," *JOSA B* **11**(10), 2128-2138 (1994).

72. R. Cheng, "Noninvasive Near-infrared Diffuse Optical Monitoring of Cerebral Hemodynamics and Autoregulation," in *Department of Biomedical Engineering*, University of Kentucky (2013).

73. G. Strangman, M. A. Franceschini, and D. A. Boas, "Factors affecting the accuracy of near-infrared spectroscopy concentration calculations for focal changes in oxygenation parameters," *Neuroimage* **18**(4), 865-879 (2003).

74. M. Ferrari, M. Muthalib, and V. Quaresima, "The use of near-infrared spectroscopy in understanding skeletal muscle physiology: recent developments," *Philos T R Soc A* **369**(1955), 4577-4590 (2011).

75. R. Cheng et al., "Noninvasive optical evaluation of spontaneous low frequency oscillations in cerebral hemodynamics," *Neuroimage* **62**(3), 1445-1454 (2012).

76. K. Gurley, Y. Shang, and G. Yu, "Noninvasive optical quantification of absolute blood flow, blood oxygenation, and oxygen consumption rate in exercising skeletal muscle," *J. Biomed. Opt.* **17**(7), 075010 (2012).

77. N. Munk et al., "Noninvasively measuring the hemodynamic effects of massage on skeletal muscle: a novel hybrid near-infrared diffuse optical instrument," *J Bodyw Mov Ther* **16**(1), 22-28 (2012).

78. Y. Shang et al., "Cerebral monitoring during carotid endarterectomy using near-infrared diffuse optical spectroscopies and electroencephalogram," *Phys Med Biol* **56**(10), 3015-3032 (2011).

79. B. J. Berne, and R. Pecora, "Dynamic light scattering with application to chemistry, biology and physics," *Courier Dover, New York* (1976).

80. T. Gisler et al., "Mode-Selective Dynamic Light-Scattering - Theory Versus Experimental Realization," *Applied optics* **34**(18), 3546-3553 (1995).

81. M. Heckmeier et al., "Imaging of dynamic heterogeneities in multiple-scattering media," *JOSA A* **14**(1), 185-191 (1997).

82. G. Maret, and P. E. Wolf, "Multiple Light-Scattering from Disordered Media - the Effect of Brownian-Motion of Scatterers," *Z Phys B Con Mat* **65**(4), 409-413 (1987).

83. L. Dong et al., "Simultaneously extracting multiple parameters via fitting one single autocorrelation function curve in diffuse correlation spectroscopy," *IEEE transactions on bio-medical engineering* **60**(2), 361-368 (2013).

84. D. A. Boas et al., "Imaging the body with diffuse optical tomography," *Signal Processing Magazine, IEEE* **18**(6), 57-75 (2001).

85. M. Schweiger, S. R. Arridge, and D. T. Delpy, "Application of the finite-element method for the forward and inverse models in optical tomography," *Journal of Mathematical Imaging and Vision* **3**(3), 263-283 (1993).

86. A. H. Hielscher, and S. Bartel, "Use of penalty terms in gradient-based iterative reconstruction schemes for optical tomography," *Journal of biomedical optics* **6**(2), 183-192 (2001).

87. H. Dehghani et al., "Near infrared optical tomography using NIRFAST: Algorithm for numerical model and image reconstruction," *Commun. Numer. Meth. Engng* **25**(6), (2009).

88. M. Jermyn et al., "Fast segmentation and high-quality three-dimensional volume mesh creation from medical images for diffuse optical tomography," *Journal of biomedical optics* **18**(8), 86007 (2013).

89. T. Li et al., "Simultaneous measurement of deep tissue blood flow and oxygenation using noncontact diffuse correlation spectroscopy flow-oximeter," *Sci Rep-Uk* **3**((2013).

90. T. Durduran et al., "Diffuse optics for tissue monitoring and tomography," *Rep Prog Phys* **73**(7), (2010).

91. D. E. Koppel, "Statistical Accuracy in Fluorescence Correlation Spectroscopy," *Physical Review A* **10**(6), 1938-1945 (1974).

92. Y. Lin et al., "Noncontact diffuse correlation spectroscopy for noninvasive deep tissue blood flow measurement," *Journal of biomedical optics* **17**(1), 010502 (2012).

93. T. Durduran et al., "Bulk optical properties of healthy female breast tissue," *Phys Med Biol* **47**(16), 2847-2861 (2002).

94. H. Dehghani et al., "Three-dimensional optical tomography: resolution in small-object imaging," *Applied optics* **42**(16), 3117-3128 (2003).

95. M. Diop et al., "Calibration of diffuse correlation spectroscopy with a time-resolved near-infrared technique to yield absolute cerebral blood flow measurements," *Biomed Opt Express* **2**(7), 2068-2081 (2011).

96. S. J. Scott Prahl, "Optical properties spectra," http://omlc.ogi.edu/spectra/index.html.

97. H. J. Van Staveren et al., "Light scattering in lntralipid-10% in the wavelength range of 400–1100 nm," *Applied optics* **30**(31), 4507-4514 (1991).

98. B. W. Pogue, and M. S. Patterson, "Review of tissue simulating phantoms for optical spectroscopy, imaging and dosimetry," *Journal of biomedical optics* **11**(4), (2006).

99. F. Ayers et al., "Fabrication and characterization of silicone-based tissue phantoms with tunable optical properties in the visible and near infrared domain," *Biomedical Optics (BiOS) 2008* 687007-687007-687009 (2008).

100. S. D. Jiang et al., "Near-infrared breast tomography calibration with optoelastic tissue simulating phantoms," *J Electron Imaging* **12**(4), 613-620 (2003).

101. Q. Zhu et al., "Design of near-infrared imaging probe with the assistance of ultrasound localization," *Applied optics* **40**(19), 3288-3303 (2001).

102. B. Brooksby et al., "Combining near-infrared tomography and magnetic resonance imaging to study in vivo breast tissue: implementation of a Laplacian-type regularization to incorporate magnetic resonance structure," *Journal of biomedical optics* **10**(5), 051504 (2005).

103. P. K. Yalavarthy et al., "Structural information within regularization matrices improves near infrared diffuse optical tomography," *Opt Express* **15**(13), 8043-8058 (2007).

104. H. Dehghani et al., "Numerical modelling and image reconstruction in diffuse optical tomography," *Philosophical transactions. Series A, Mathematical, physical, and engineering sciences* **367**(1900), 3073-3093 (2009).

105. P. K. Yalavarthy et al., "Critical computational aspects of near infrared circular tomographic imaging: Analysis of measurement number, mesh resolution and reconstruction basis," *Opt Express* **14**(13), 6113-6127 (2006).

106. B. A. Brooksby et al., "Near-infrared (NIR) tomography breast image reconstruction with a priori structural information from MRI: Algorithm development for reconstructing heterogeneities," *Ieee J Sel Top Quant* **9**(2), 199-209 (2003).

107. M. Huang, and Q. Zhu, "Dual-mesh optical tomography reconstruction method with a depth correction that uses a priori ultrasound information," *Applied optics* **43**(8), 1654-1662 (2004).

108.H. Dehghani et al., "Depth sensitivity and image reconstruction analysis of dense imaging arrays for mapping brain function with diffuse optical tomography," *Applied optics* **48**(10), D137-143 (2009).

109.S. Arridge, and J. Schotland, "Optical tomography: forward and inverse problems," *arXiv preprint arXiv:0907.2586* (2009).

110.S. I. Kabanikhin, "Definitions and examples of inverse and ill-posed problems," *J Inverse Ill-Pose P* **16**(4), 317-357 (2008).

111.P. Vaupel, F. Kallinowski, and P. Okunieff, "Blood flow, oxygen and nutrient supply, and metabolic microenvironment of human tumors: a review," *Cancer research* **49**(23), 6449-6465 (1989).

112.V. R. Kondepati, H. M. Heise, and J. Backhaus, "Recent applications of near-infrared spectroscopy in cancer diagnosis and therapy," *Anal Bioanal Chem* **390**(1), 125-139 (2008).

113.C. B. Wilson et al., "Quantitative Measurement of Monoclonal-Antibody Distribution and Blood-Flow Using Positron Emission Tomography and I-124 in Patients with Breast-Cancer," *Int J Cancer* **47**(3), 344-347 (1991).

114.H. Madjar et al., "Color Doppler and duplex flow analysis for classification of breast lesions," *Gynecol Oncol* **64**(3), 392-403 (1997).

115.R. Choe et al., "Optically measured microvascular blood flow contrast of malignant breast tumors," *PloS one* **9**(6), e99683 (2014).

116.V. Ntziachristos et al., "MRI-guided diffuse optical spectroscopy of malignant and benign breast lesions," *Neoplasia* **4**(347-354 (2002).

117.Q. Zhu et al., "Benign versus Malignant Breast Masses: Optical differentiation with US-guided Optical Imaging Reconstruction (vol 237, pg 57, 2005)," *Radiology* **239**(2), (2006).

118."Breast Cancer Screen," Wikipedia, https://upload.wikimedia.org/wikipedia/commons/8/80/Breast_self-exam_NCI_visuals_online.jpg.

119.L. ANSftSUo, "American National Standard for the Safe Use of Lasers," *American National Standards Institute. ANSIZ136. New York, NY: American National Standards Institute* (2007).

120.S. Ueda et al., "Baseline tumor oxygen saturation correlates with a pathologic complete response in breast cancer patients undergoing neoadjuvant chemotherapy," *Cancer research* **72**(17), 4318-4328 (2012).

121.L. Enfield et al., "Monitoring the response to neoadjuvant hormone therapy for locally advanced breast cancer using three-dimensional time-resolved optical mammography," *Journal of biomedical optics* **18**(5), (2013).

122.N. G. Chen et al., "Portable near-infrared diffusive light imager for breast cancer detection," *Journal of biomedical optics* **9**(3), 504-510 (2004).

123.W. T. Yang et al., "Correlation between color power Doppler sonographic measurement of breast tumor vasculature and immunohistochemical analysis of microvessel density for the quantitation of angiogenesis," *Journal of ultrasound in medicine* **21**(11), 1227-1235 (2002).

124.Y. Shang et al., "Diffuse optical monitoring of repeated cerebral ischemia in mice," *Opt. Express* **19**(21), 20301-20315 (2011).

125.D. J. Pine et al., "Diffusing-wave spectroscopy," *Phys.Rev.Lett.* **60**(12), 1134-1137 (1988).

126.M. J. Stephen, "Temporal fluctuations in wave propagation in random media," *Phys.Rev.B* **37**(1), 5 (1988).

127.G. Yu et al., "Intraoperative evaluation of revascularization effect on ischemic muscle hemodynamics using near-infrared diffuse optical spectroscopies," *J. Biomed. Opt.* **16**(2), 027004 (2011).

128.Y. Shang et al., "Effects of muscle fiber motion on diffuse correlation spectroscopy blood flow measurements during exercise," *Biomed. opt. express* **1**(2), 500-511 (2010).

129.L. He et al., "Using optical fibers with different modes to improve the signal-to-noise ratio of diffuse correlation spectroscopy flow-oximeter measurements," *Journal of biomedical optics* **18**(3), (2013).

130.U. Sunar et al., "Noninvasive diffuse optical measurement of blood flow and blood oxygenation for monitoring radiation therapy in patients with head and neck tumors: a pilot study," *J. Biomed. Opt.* **11**(6), 064021 (2006).

131.T. Gisler et al., "Mode-selective dynamic light scattering: theory versus experimental realization," *Appl. Opt.* **34**(18), 3546-3553 (1995).

132.G. Dietsche et al., "Fiber-based multispeckle detection for time-resolved diffusing-wave spectroscopy: characterization and application to blood flow detection in deep tissue," *Applied optics* **46**(35), 8506-8514 (2007).

133.J. Li et al., "Transient functional blood flow change in the human brain measured noninvasively by diffusing-wave spectroscopy," *Opt. Lett.* **33**(19), 2233-2235 (2008).

134.J. Li et al., "Noninvasive detection of functional brain activity with near-infrared diffusing-wave spectroscopy," *Journal of biomedical optics* **10**(4), 44002 (2005).

135.E. G. Neumann, *Single-Mode Fibers: Fundamentals*, Springer-Verlag, Berlin (1988).

136.C. Zhou, "In-vivo optical imaging and spectroscopy of cerebral hemodynamics," in *Dept. Physics and Astronomy*, pp. xxiii, 325 p., University of Pennsylvania, Philadelphia (2007).

137.C. Yeh, and F. Shimabukuro, *The Essence of Dielectric Waveguides*, 1 ed., Springer, New York (2008).

138.S. Fantini et al., "Non-invasive optical monitoring of the newborn piglet brain using continuous-wave and frequency-domain spectroscopy," *Phys. Med. Biol* **44**((1999).

139.A. k. Chatak, *Optics*, 1 ed., Tata McGraw-Hill, New Delhi (2009).

140.R. G. Lyons, *Understanding Digital Signal Processing*, Prentice Hall, New Jersey (2010).

141.J. H. Zar, "Biostatistical Analysis," pp. 88-89, Prentice-Hall, NJ (1999).

142.J. H. Zar, "Biostatistical Analysis," p. 110, Prentice-Hall, NJ (1999).

143.D. Irwin, "Influence of tissue absorption and scattering on diffuse correlation spectroscopy blood flow measurements," in *Dept. Biomedical Eng.*, pp. x, 67 p., University of Kentucky, Lexington (2011).

144.L. He et al., "Noncontact Diffuse Correlation Tomography of Human Breast Tumor," *Journal of biomedical optics* **Accepted**((2015).

145.C. Huang et al., "Speckle contrast diffuse correlation tomography of complex turbid medium flow," *Medical physics* **42**(7), 4000-4006 (2015).

VITA

Lian He, Ph.D. candidate

EDUCATION

Nanjing University of Aeronautics and Astronautics, Nanjing, Jiangsu, P.R. China
B.E., Biomedical Engineering, June 2009

Rutgers University, New Brunswick, NJ, USA
Master student, Biomedical Engineering, August 2009 - August 2010

University of Kentucky, Lexington, KY, USA
Ph.D. candidate, Biomedical Engineering, August 2010 – present

PROFESSIONAL POSITIONS

Research Assistant, Department of Biomedical Engineering, University of Kentucky, Lexington, KY

AWARDS

Dissertation Year Fellowship, University of Kentucky	2014 - 2015
Conference Travel Support Awards, University of Kentucky	2012, 2014
NIRFAST Workshop Travel Support Award, OSA, Miami, FL	2012

PROFESSIONAL MEMBERSHIP

Optical Society of America (OSA)	2012, 2014

PUBLICATIONS

Peer Reviewed Journals (7)

1. **L. He**, Y. Lin, Y. Shang, B. Shelton, G. Yu, "Using optical fibers with different modes to improve the signal-to-noise ratio (SNR) of diffuse correlation spectroscopy (DCS) flow-oximeter measurements", *Journal of Biomedical Optics*18(3), 037001 (2013)
2. **L. He**, Y. Lin, C. Huang, D. Irwin, M. Szabunio, G. Yu, "Noncontact Diffuse Correlation Tomography of Human Breast Tumor", *Journal of Biomedical Optics*, (Accepted 2015)

3. C. Huang, D. Irwin, Y. Lin, Y. Shang, **L. He**, W. Kong, J. Luo, G. Yu, "Speckle contrast diffuse correlation tomography of complex turbid medium flow", *Medical Physics Letter*,42(7), 4000 (2015)
4. Y. Lin, C. Huang, D. Irwin, **L. He**, Y. Shang, G. Yu, "Three-dimensional flow contrast imaging of deep tissue using noncontact diffuse correlation tomography", *Applied Physics Letters*,104.12 (2014)
5. T. Li, Y. Lin, Y. Shang, **L. He**, C. Huang, M. Szabunio, G. Yu, "Simultaneous measurement of deep tissue blood flow and oxygenation using noncontact diffuse correlation spectroscopy flow-oximeter", *Scientific Reports*,3, 1358 (2013)
6. Y. Lin, **L. He**, Y. Shang, G. Yu, "Noncontact diffuse correlation spectroscopy for noninvasive deep tissue blood flow measurement", *Journal of Biomedical Optics Letters* 17(2), 010502 (2012)
7. L. Dong, **L. He**, Y. Lin, Y. Shang, G. Yu, "Simultaneously extracting multiple parameters via fitting one single autocorrelation function curve in diffuse correlation spectroscopy", *IEEE Transactions on Biomedical Engineering*, TBME-01162 (2012)

CONFERENCE PROCEEDINGS/ABSTRACTS (22)

1. **L. He**, Y. Lin, C. Huang, D. Irwin, M. Szabunio, G. Yu, "Noncontact Diffuse Correlation Tomography of Human Breast Tumor", UK CCTS Spring Conference, Lexington, KY, 2015
2. **L. He**, Y. Lin, C. Huang, D. Irwin, M. Szabunio, G. Yu, "Noncontact Diffuse Correlation Tomography of Human Breast Tumor", UK Markey Cancer Research Day, Lexington, KY, 2015
3. D. Irwin*, C. Huang*, Y. Lin, Y. Shang, **L. He**, W. Kong, J. Luo, G. Yu, "Speckle contrast diffuse correlation tomography for flow contrast imaging of complex turbid media", UK CCTS Spring Conference, Lexington, KY, 2015
4. D. Irwin*, C. Huang*, Y. Lin, Y. Shang, **L. He**, W. Kong, J. Luo, G. Yu, "Speckle contrast diffuse correlation tomography for flow contrast imaging of complex turbid media", UK Markey Cancer Research Day, Lexington, KY, 2015
5. D. Irwin, C. Huang, Y. Lin, Y. Shang, **L. He**, W. Kong, J. Luo, G. Yu, "Speckle Contrast Diffuse Correlation Tomography for Flow Contrast Imaging of Turbid Media", Biomedical Engineering Society (BMES), Tampa, FL, 2015
6. **L. He,** Y. Lin, C. Huang, G. Yu, "3-D Blood Flow Imaging of Breast Tumor Using Noncontact Diffuse Correlation Tomography: Computer Simulations", OSA Biomedical Optics, Miami, FL, 2014
7. C. Huang, Y. Lin, **L. He**, D. Irwin, G. Yu, " A novel CAD-based method to generate individualized finite element mesh and source-detector alignment for noncontact diffuse correlation tomography", OSA Biomedical Optics, Miami, FL, 2014
8. D. Irwin, Y. Lin, C. Huang, **L. He**, Y. Shang, G. Yu, "Noncontact near-Infrared 3-D blood flow contrast imaging on small animal mammary tumors: preliminary results", OSA Biomedical Optics (BIOMED), Miami, FL, 2014
9. Y. Lin, C. Huang, D. Irwin, **L. He**, Y. Shang, G. Yu, "Noncontact three-dimensional flow contrast imaging of deep tissue using diffuse correlation tomography", OSA Biomedical Optics, Miami, FL, 2014

10. Y. Lin, T. Li, Y. Shang, **L. He**, C. Huang, M. Szabunio, G. Yu, "Simultaneous measurement of deep tissue blood flow and oxygenation using noncontact diffuse correlation spectroscopy flow-oximeter", OSA Biomedical Optics, Miami, FL, 2014
11. L. Dong, **L. He**, Y. Lin, Y. Shang, G. Yu, "Exploring the extraction of multiple parameters simultaneously from fitting an autocorrelation function curve in diffuse correlation spectroscopy", OSA Biomedical Optics, Miami, FL, 2014
12. **L. He**, Y. Lin, C. Huang, D. Irwin, M. Szabunio, G. Yu, "Noncontact diffuse optical 3-D imaging of hemodynamic contrasts in breast tumor: computer simulation", UK CCTS Spring Conference, Lexington, KY, 2013
13. C. Huang, Y. Lin, **L. He**, Y. Shang, D. Irwin, M. Szabunio, G. Yu, "Noncontact diffuse optical 3-D imaging of hemodynamic contrasts in breast tumor: geometrical reconstruction and alignment of optical sources and detectors, UK CCTS Spring Conference, Lexington, KY, 2013
14. D. Irwin, Y. Lin, **L. He**, C. Huang, Y. Shang, M. Zhao, G. Yu, "Noncontact 3-D imaging of small animal tumors with combined diffuse optical, correlation, and fluorescence tomography: preliminary results in phantoms", UK CCTS Spring Conference, Lexington, KY, 2013
15. Y. Lin, T. Li, Y. Shang, **L. He**, C. Huang, M. Szabunio, G. Yu, "Simultaneous measurement of deep tissue blood flow and oxygenation using noncontact diffuse correlation spectroscopy flow-oximeter", UK CCTS Conference, Lexington, KY, 2013
16. **L. He**, Y. Lin, C. Huang, D. Irwin, M. Szabunio, G. Yu, "Noncontact diffuse optical 3-D imaging of hemodynamic contrasts in breast tumor: computer simulation", UK Markey Cancer Research Day, Lexington, KY, 2013
17. C. Huang, Y. Lin, **L. He**, Y. Shang, D. Irwin, M. Szabunio, G. Yu, "Noncontact diffuse optical 3-D imaging of hemodynamic contrasts in breast tumor: geometrical reconstruction and alignment of optical sources and detectors", UK Markey Cancer Research Day, Lexington, KY, 2013
18. Y. Lin, T. Li, Y. Shang, **L. He**, C. Huang, M. Szabunio, G. Yu, "Simultaneous measurement of deep tissue blood flow and oxygenation using noncontact diffuse correlation spectroscopy flow-oximeter", UK Markey Cancer Research Day, Lexington, KY, 2013
19. D. Irwin, Y. Lin, **L. He**, C. Huang, Y. Shang, M. Zhao, G. Yu, "Noncontact 3-D imaging of small animal tumors with combined diffuse optical, correlation, and fluorescence tomography: preliminary results in phantoms", UK Markey Cancer Research Day, Lexington, KY, 2013
20. **L. He**, Y. Lin, Y. Shang, and G. Yu, "Noncontact 3-D optical imaging of breast tumor", UK Markey Cancer Research Day, Lexington, KY, 2012
21. **L. He**, Y. Lin, Y. Shang, and G. Yu, "Using few-mode fiber to improve the signal-to-noise ratio of DCS flow-oximeter measurements", OSA Biomedical Optics, Miami, FL, 2012
22. Y. Lin, **L. He**, Y. Shang, G. Yu, "Noncontact diffuse correlation spectroscopy probe for deep tissue blood flow measurement", OSA Biomedical Optics, Miami, FL, 2012